

Interplay Between Neutrino Kicks and Hydrodynamic Kicks of Neutron Stars and Black Holes

Hans-Thomas Janka^{1*} and Daniel Kresse^{1,2†}

^{1*}Max Planck Institute for Astrophysics, Karl-Schwarzschild-Straße 1, Garching, 85748, Germany.

²Technical University of Munich, TUM School of Natural Sciences, Physics Department, James-Franck-Straße 1, Garching, 85748, Germany.

*Corresponding author(s). E-mail(s): thj@mpa-garching.mpg.de;

Contributing authors: danielkr@mpa-garching.mpg.de;

†These authors contributed equally to this work.

Abstract

Neutron stars (NSs) are observed with high space velocities and elliptical orbits in binaries. The magnitude of these effects points to natal kicks that originate from asymmetries during the supernova (SN) explosions. Using a growing set of long-time 3D SN simulations with the PROMETHEUS-VERTEX code, we explore the interplay of NS kicks that are induced by asymmetric neutrino emission and by asymmetric mass ejection. Anisotropic neutrino emission can arise from a large-amplitude dipolar convection asymmetry inside the proto-NS (PNS) termed LESA (Lepton-number Emission Self-sustained Asymmetry), which determines the kicks of NSs born from stars near the low-mass end of SN progenitors. In more massive progenitors aspherical accretion downflows around the PNS can also lead to anisotropic neutrino emission (absorption) with a neutrino-induced NS kick roughly opposite to (aligned with) the kick by asymmetric mass ejection. We estimate upper bounds for the final neutrino kicks of $150\text{--}260\text{ km s}^{-1}$, whereas the hydrodynamic kicks can reach up to more than 1300 km s^{-1} . Therefore the hydrodynamic kicks dominate for NSs from explosions of higher-mass progenitors, whereas the neutrino kicks dominate in the case of NSs from the lowest-mass progenitors. Our models suggest that the Crab pulsar as a representative of the latter category could have received its velocity of $\sim 160\text{ km s}^{-1}$ by a neutrino kick due to the LESA asymmetry. Such neutrino kicks of $100\text{--}200\text{ km s}^{-1}$ define a nearly ubiquitous floor value, which may shed new light on the origin of pulsars in globular clusters. Black holes, if formed by the collapse of short-lived PNSs and solely kicked by anisotropic neutrino emission, obtain velocities of only some km s^{-1} .

Keywords: Stars: neutron, Stars: black holes, Supernovae: general, Stars: massive, Neutrinos, Hydrodynamics

1 Introduction

Various observational findings provide evidence that neutron stars (NSs) obtain natal kicks during their birth in the supernova (SN) explosions of massive stars. Radio pulsars are found to

possess space velocities of up to $\sim 1500\text{ km s}^{-1}$ (e.g., [Arzoumanian et al, 2002](#); [Hobbs et al, 2005](#); [Chatterjee et al, 2005](#)), NSs associated with core-collapse supernova (CCSN) remnants exhibit displacements from the geometric center of the

explosion (e.g., Puppis A, Mayer et al 2020; Cas A, Holland-Ashford et al 2023), and orbital parameters of NSs in binary systems require kicks of the compact objects (for a summary of relevant observational aspects, see Lai et al, 2001). These observations cannot be explained by the electromagnetic recoil due to the Harrison-Tademaru effect (Lai et al, 2001) or the Blaauw mechanism (Blaauw, 1961), which predicts binary systems to become affected and even unbound by the mass loss connected to the SN explosion of one component. Instead, intrinsic asymmetries during the SN explosions must be the dominant effect for kicking the NSs. Different studies have pointed to the NS kick distribution being unimodal (Hobbs et al, 2005) or bimodal (Arzoumanian et al, 2002) with an average velocity of 200–500 km s⁻¹. In particular, a fraction of the NS population must have received relatively lower kick velocities in order to account for the pulsars found gravitationally bound in globular clusters (e.g., Abbate et al, 2023; Heywood, 2023; Wu et al, 2023). Also NSs born in low-mass X-ray binaries (Bahramian and Degenaar, 2023; O’Doherty et al, 2023) and high-mass X-ray binaries (Kim et al, 2023) as well as those in the binary NSs observed in our Galaxy (Gaspari et al, 2024) and measured by gravitational waves in their latest pre-merger evolution (Abbott et al, 2017a,b) were not kicked out of their orbits but stayed bound to their companions.

Anisotropic mass-energy loss through asymmetrically ejected gas and neutrinos must be considered as the primary mediators of the recoil momentum transferred to NSs during their birth, causing hydrodynamic NS kicks and neutrino-induced NS kicks (e.g., Janka and Müller, 1994; Burrows and Hayes, 1996; Fryer and Kusenko, 2006), since the energy radiated in gravitational waves by collapsing stars is minuscule (typically less than $10^{-7} M_{\odot} c^2$; Radice et al 2019; Powell and Müller 2019; Andresen et al 2021; Mezzacappa et al 2023; Vartanyan et al 2023) compared to the gravitational binding energy of the newborn NS radiated in neutrinos (several 10^{53} erg or $\gtrsim 0.1 M_{\odot} c^2$; Sukhbold et al, 2016; Kresse et al, 2021; Vartanyan and Burrows, 2023) and compared to the kinetic energy of the SN ejecta (exceeding $\sim 10^{50}$ erg; Kasen and Woosley, 2009; Pejcha and Prieto, 2015; Martinez et al, 2022). Abundant theoretical work has been devoted to

understanding of these NS kicks (e.g., Janka and Müller, 1994; Scheck et al, 2004; Burrows and Hayes, 1996; Scheck et al, 2006; Nordhaus et al, 2010, 2012; Wongwathanarat et al, 2010, 2013; Janka, 2017; Müller et al, 2017; Gessner and Janka, 2018; Müller et al, 2019; Nagakura et al, 2019; Powell and Müller, 2020; Bollig et al, 2021; Rahman et al, 2022; Powell et al, 2023; Coleman and Burrows, 2022; Burrows et al, 2023b), based mainly on axi-symmetric (2D) CCSN simulations until about 2010 and later on three-dimensional (3D) simulations.

Interestingly, in their neutrino-driven 3D SN simulations, Wongwathanarat et al (2013) found that iron-group nuclei and intermediate-mass elements (IMEs, mainly those heavier than ²⁴Mg) are ejected preferentially, i.e. with higher abundances, in the hemisphere opposite to the direction of a large hydrodynamic NS kick, because the SN explosion and mass ejection are stronger on this side. Such a geometry is dictated by linear momentum conservation, which implies that the net momentum of the ejected gas is balanced by the opposite momentum received by the kicked NS. Since the SN shock and the gas outflow that is driven by the neutrino energy deposition are stronger where the SN explosion is more powerful, also the explosive nucleosynthesis is more efficient on this side, which enhances the production of IMEs by nuclear burning in shock-heated matter and of iron-group nuclei, trans-iron species, and radioactive isotopes such as ⁴⁴Ti in the freeze-out from NSE in neutrino-heated material.

Wongwathanarat et al (2017) showed that this explosion-nucleosynthesis-kick asymmetry shapes the entire large-scale morphology of Cassiopeia A (Cas A), which is the remnant of a type-IIb SN of a progenitor star that had stripped almost all of its hydrogen envelope, allowing the evolving ejecta to retain the explosion geometry very clearly even at the stage of the aging SN remnant (Orlando et al, 2021). The NuSTAR (Nuclear Spectroscopic Telescope Array) mapping of the radioactive ⁴⁴Ti distribution in Cas A by Grefenstette et al (2014) and Grefenstette et al (2017) provides general support of the picture drawn by the 3D simulations and thus for Cas A being the relic of a neutrino-driven SN explosion with the NS having received its natal kick mainly by the hydrodynamic recoil

of asymmetrically ejected gas. A closer analysis of the gas geometry (Holland-Ashford et al, 2017) and of the distribution of IMEs (Katsuda et al, 2018) in larger samples of SN remnants also reveals overall consistency with this scenario.

Although neutrino-induced NS kicks had also been evaluated in some of the mentioned simulation-based studies (e.g. Scheck et al, 2006; Nordhaus et al, 2010; Wongwathanarat et al, 2013; Nagakura et al, 2019; Rahman et al, 2022), the models considered there were still handicapped by their 2D nature or their simplified treatment of the neutrino physics and transport, or both. A reliable determination of the neutrino kicks requires a sophisticated treatment of the neutrino transport in full 3D simulations conducted over sufficiently long evolution times of, at best, several seconds. Such simulations have become available only recently (Stockinger et al, 2020; Bollig et al, 2021; Coleman and Burrows, 2022; Burrows et al, 2023b). We supplement this recent work by a detailed and comprehensive analysis of a growing set of 3D stellar core-collapse simulations performed with the PROMETHEUS-VERTEX SN code of the Garching group including cases that lead to black-hole (BH) formation.

The situation is observationally less consolidated for natal BH kicks than for NS kicks (e.g., Andrews and Kalogera, 2022). Many stellar population synthesis studies assume BH kicks with a momentum distribution similar to that of NS kicks, i.e., with a BH velocity distribution that is reduced by the BH-to-NS mass ratio or the fraction of the stellar envelope that falls back (e.g., Fryer et al, 2012; Mandel and Müller, 2020; Mandel et al, 2021; Oh et al, 2023; Stevance et al, 2023). However, referring to the observation of some low-mass X-ray binaries containing BHs at large distances above the plane of the Milky Way, Repetto et al (2012), Repetto and Nelemans (2015), and Repetto et al (2017) concluded that the velocity distribution instead of the momentum of natal kicks of at least this population of BHs might be more similar to that of NSs (but see Mandel, 2016, for counter-arguments). Detailed observations of individual low-mass X-ray binaries and BH X-ray binaries indeed confirm that natal kicks of considerable magnitude (up to several 100 km s^{-1} at least) can be imparted to the BHs in such systems (e.g., Atri et al, 2019; Kimball

et al, 2023; Dashwood Brown et al, 2024). Janka (2013) explained this possibility by low-mass BHs that form due to asymmetric mass accretion onto the transiently existing NS when initially ejected material falls back, because the SN explosion is not strong enough to unbind the inner layers of the collapsing star. The thus born BH may receive a large hydrodynamic kick provided the SN explosion is still sufficiently powerful to expel a considerable fraction of the asymmetrically distributed innermost ejecta. Recent 3D simulations of such fallback SNe within the framework of the neutrino-driven mechanism lend support to the viability of this predicted scenario (Chan et al, 2020) and even show quantitative agreement (Burrows et al, 2023a) with the analytic estimates by Janka (2013).

Based on theoretical considerations one also expects a population of BHs that are born in stellar core-collapse events without a SN explosion or where the SN blast is too weak to produce asymmetric ejecta. Under these circumstances either little mass ejection by the wimpy SN occurs or mass loss is absent or effectively spherical if (a part of) the hydrogen envelope of the progenitor is stripped due to the so-called mass-decrement effect (Nadezhin, 1980; Lovegrove and Woosley, 2013) when the gravitational potential of the NS prior to BH formation is reduced by the energy loss through neutrino emission. In such cases the BH receives a natal kick that is solely caused by anisotropic neutrino emission and should remain very low, namely of the order of a few km s^{-1} , if the BH forms within fractions of a second (Rahman et al, 2022), or at most some 10 km s^{-1} , if the NS lives for a few seconds before it collapses to a BH (Burrows et al, 2023b). Very recently, the BH binary VFTS 243 was identified by its well determined system properties as the first case where the BH has received a very low kick velocity predominantly by asymmetric neutrino emission (Vigna-Gómez et al, 2023).

The present paper aims at a consistent and comprehensive evaluation of the hydrodynamic kicks together with the corresponding neutrino-induced kicks of new-born NSs and BHs for a set of long-term 3D stellar collapse simulations performed by the Garching group for progenitor stars with zero-age-main-sequence (ZAMS) masses between $9 M_{\odot}$ and $75 M_{\odot}$. We thus intend to shed light on the physical origin of these kicks

by tracking down in detail the processes that play a role for the acceleration of the compact remnants. Our special focus will be on the complex interplay of neutrino and hydrodynamic momentum transfer that is a consequence of their mutual coupling due to neutrino interactions in the stellar matter. In the course of this effort we also intend to relate our results to those of similar analyses reported in recent literature and thus to clarify some misconceptions discussed there. In particular, we will furnish further evidence that the effect that acts longest in accelerating NSs (and some BHs) is the gravitational attraction between the compact remnant and the asymmetric ejecta gas. Since the momentum transfer to the compact remnant by the force of gravity accounts for the dominant contribution to the hydrodynamic kicks, we will argue that the term “gravitational tugboat mechanism” for the hydrodynamic recoil of the compact objects (Wongwathanarat et al, 2013) is well justified. Our work is further motivated by the goal to understand the relevance of neutrino-induced kicks for the total NS kicks, because this might have consequences for the interpretation of the mentioned observations of SN remnants where the NS kick vector points opposite to the direction of a dipole deformation of the ejecta or enhanced concentrations of IMEs and iron-group elements.

Our paper is structured as follows. In Section 2 we briefly describe the simulation code and its inputs, the investigated progenitors, and the results of their long-term 3D core-collapse simulations, and we provide the details of our numerical methods to evaluate these 3D simulations for the hydrodynamic and neutrino-induced NS and BH kicks. In Section 3 we report our results for the hydrodynamic and neutrino kicks of NSs in models with successful SN explosions as well as our results for neutrino-induced BH kicks in models that fail to explode. Section 4 contains a summary, discussion, and conclusions. In Appendices A–C we present, for all of our 3D simulations with sophisticated neutrino transport, supplementary plots which show in detail the time evolution of quantities that are especially relevant for understanding the physical effects that contribute to the neutrino-induced NS and BH kicks.

2 Numerical modeling

2.1 Simulation code and inputs

The 3D CCSN models discussed in this work were computed with the PROMETHEUS-VERTEX neutrino-hydrodynamics code (Rampp and Janka, 2002; Buras et al, 2006). The PROMETHEUS hydrodynamics module (Fryxell et al, 1989; Keil, 1997; Kifonidis et al, 2003) is based on a higher-order Godunov scheme for the Newtonian hydrodynamics equations, which are integrated with directional splitting and an exact Riemann solver for ideal gases. The VERTEX transport module solves the energy and velocity ($\mathcal{O}(v/c)$) dependent three-flavor neutrino transport by a two-moment scheme with Boltzmann closure (Rampp and Janka, 2002). The three-dimensionality of the transport problem is handled by a ray-by-ray-plus (RbR+) approach, which computes only radial neutrino flux components because it applies the assumption that the neutrino phase space distribution is axially symmetric around the radial direction. The good overall agreement of neutrino properties and hydrodynamic evolution in 3D CCSN simulations with the RbR+ approximation and full multi-dimensional transport was demonstrated by Glas et al (2019a). The neutrino energy bins are fully coupled for the propagator and interaction terms and the reported simulations employed an energy grid with 12–15 bins up to a maximum energy of 380 MeV. The code includes general relativistic effects in the monopole term of the gravitational potential (Case A of Marek et al, 2006) as well as corrections for general relativistic redshift and time dilation in the neutrino transport. Some of the 3D simulations were presented in previous papers (see Table 1), where details of the specific numerical setups can be found. A recent summary of the most relevant features of the code, its input physics for the equation of state (EoS) of the stellar plasma and the nuclear composition, and the neutrino reactions taken into account in the transport solver is provided by Fiorillo et al (2023).

Most of the 3D simulations leading to SN explosions and NS formation were computed with the nuclear EoS of Lattimer and Swesty (1991) (LS220, using an incompressibility modulus of 220 MeV), but in some of the reported models, in particular for BH formation, we also employed the

Table 1 Overview of investigated models: progenitor properties and setups of 3D CCSN simulations

Model	M_{ZAMS} [M_{\odot}]	M_{prec} [M_{\odot}]	M_{He} [M_{\odot}]	Z [Z_{\odot}]	$\xi_{2.5}$	Progenitor Dim./Rot.	EoS	Grid early/late	N_r	Refs.
s9.0	9.00	8.75	1.57	1	0.00004	1D, non-rot.	LS220	YY-SMR/ 2°	400–626	[1],[9,17]
z9.6	9.60	9.60	1.70	0	0.00008	1D, non-rot.	LS220	YY- 2°	400–700	[2],[10,17]
s12.28	12.28	11.13	3.29	1	0.03167	3D, non-rot.	SFHo	YY- 3.5°	550–729	[3,4],[11,18]
m15	15.00	11.23	4.77	1	0.10602	1D, rot.*	LS220	YY- 2°	400–800	[5],[12,18]
m15e	"	"	"	"	"	"	LS220	YY- 2°	400–800	[5],[12,18]
s18.88	18.88	14.34	5.79	1	0.28335	3D, non-rot.	LS220	YY- 2°	550–730	[6],[13,18]
s20	20.00	15.93	6.33	1	0.28462	1D, non-rot.	LS220	SP/YY- 2°	400–750	[7],[14,18]
s20e	"	"	"	"	"	"	LS220	SP/YY- 2°	400–740	[7],[14,18]
s40	40.00	15.34	15.34	1	0.54399	1D, non-rot.	LS220	YY- 5°	400–667	[7],[15,16,18]
u75_DD2	75.00	74.05	54.84	10^{-4}	0.88157	1D, non-rot.	DD2	YY- 5°	400–646	[8],[15,18]
u75_LS220_1	"	"	"	"	"	"	LS220	YY- 5°	400–562	[8],[15,18]
u75_LS220_2	"	"	"	"	"	"	LS220	YY- 5°	400–562	[8],[15,18]
u75_LS220_hr	"	"	"	"	"	"	LS220	YY-SMR	400–573	[8],[15,16,18]
u75_SFHo	"	"	"	"	"	"	SFHo	YY- 5°	400–706	[8],[15,18]

Note: M_{ZAMS} , M_{prec} , and M_{He} are the progenitor’s ZAMS mass, pre-collapse mass, and helium-core mass (defined by 50% hydrogen mass fraction); Z and $\xi_{2.5}$ are the progenitor’s metallicity and (pre-collapse) compactness parameter (O’Connor and Ott, 2011a); 3D/1D and rot./non-rot. indicates whether the pre-collapse evolution has been simulated in 3D/1D and with/without rotation [^(*)model m15 at 10 ms after the bounce: iron-core mass $M_{Fe} = 1.42 M_{\odot}$, radius $R_{Fe} = 8.2 \times 10^7$ cm, moment of inertia $I_{Fe} = 8.9 \times 10^{47}$ g cm², angular momentum $J_{Fe} = 9.7 \times 10^{47}$ g cm²s⁻¹, average rotation period $\bar{P}_{Fe} = 2\pi I_{Fe}/J_{Fe} = 5.8$ s]; nuclear EoS: LS220, SFHo, or DD2; computational grid: Yin-Yang (YY) or spherical polar (SP), with uniform angular resolution $\Delta\theta \in \{2^{\circ}, 3.5^{\circ}, 5^{\circ}\}$ or with static mesh refinement (SMR) for angular grid ($0.5^{\circ} \leq \Delta\theta \leq 2^{\circ}$); number of radial zones (N_r ; min.–max.). **References (progenitor models):** [1] Woosley and Heger (2015), [2] Heger (2012), [3] Sukhbold et al (2018), [4] N. Yadav (2023, priv. com.), [5] Heger et al (2005), [6] Yadav et al (2020), [7] Woosley and Heger (2007), [8] Woosley et al (2002). **References (SN/BH models):** [9] Melson et al (2020), [10] Melson et al (2015b), [11] R. Bollig (2023, priv. com.), [12] Summa et al (2018), [13] Bollig et al (2021), [14] Melson et al (2015a), [15] A. Summa (2018, priv. com.), [16] Walk et al (2020), [17] Stockinger et al (2020), [18] Kresse et al (2024, in prep.).

DD2 and SFHo EoSs of Hempel and Schaffner-Bielich (2010); Steiner et al (2013) (see Table 1).

The refined treatment of the neutrino transport with the VERTEX module was applied for several seconds only in two of our most recent 3D simulations, whereas in all of the other models the VERTEX transport was used for at most about 600 ms after core bounce (time t'_f listed in Tables 2 and 3). At that time either the NS began to collapse to a BH and the simulation was stopped or the calculation was continued with a more approximate description of the neutrino heating and cooling inside and around the proto-neutron star (PNS), applying neutrino transport results from detailed 1D PNS cooling simulations that took into account PNS convection by a mixing-length treatment. The numerical method for this transport approximation, which we call NEMESIS (Neutrino-Extrapolation Method for Efficient SIMulations of Supernova explosions), was first introduced in Appendix E of Stockinger et al (2020) and further improved by Kresse (2023) (D. Kresse et al, 2024, in preparation).

2.2 Investigated models

Table 1 lists the basic properties of the progenitor stars considered in our study and some elementary information of the computed core-collapse and SN models: the ZAMS mass, pre-collapse mass, helium core mass, stellar metallicity, compactness parameter

$$\xi_M \equiv \frac{M/M_{\odot}}{r(M)/1000 \text{ km}} \quad (1)$$

(O’Connor and Ott, 2011b) for a chosen value of $M = 2.5 M_{\odot}$ of the enclosed mass ($r(M)$ is the corresponding radius inside the star), the dimension of the pre-collapse model and the total angular momentum as well as the average rotation period of the iron core shortly after core bounce for the rotating $15 M_{\odot}$ model, the nuclear EoS used, the computational grids employed in the CCSN simulation (with/without VERTEX neutrino transport), and the corresponding angular resolution as well as the (time-dependent) number of radial grid

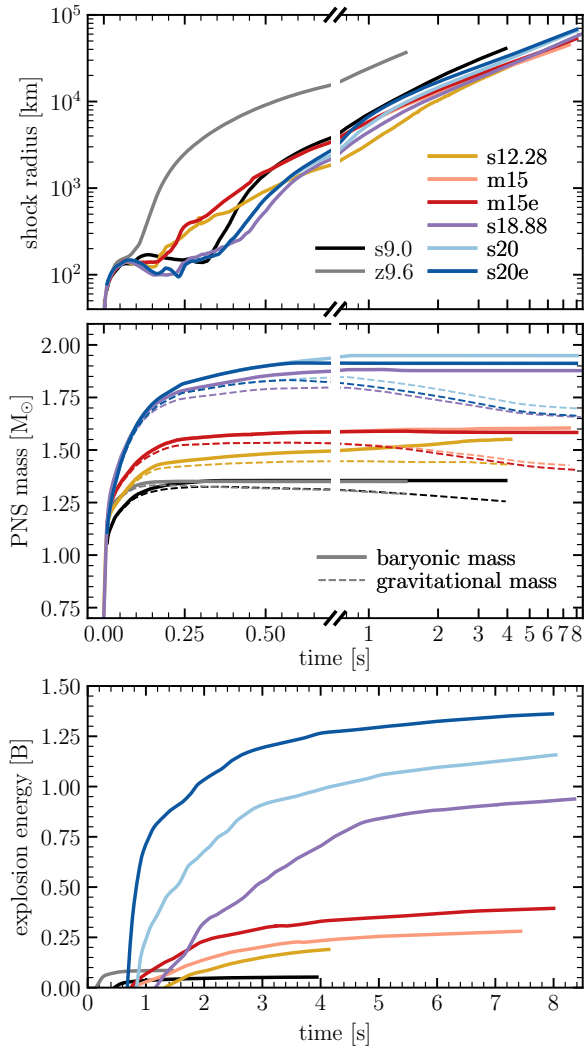


Fig. 1 Angle-averaged shock radii (*top*), baryonic PNS masses (solid lines) and gravitational PNS masses (dashed lines; *middle*), and explosion energies (with overburden energy taken into account; *bottom*; $1\text{B} = 1\text{bethe} = 10^{51}\text{ erg}$) for all successfully exploding models. Note that the time axes in the top and middle panels are different from that of the bottom panel for better visibility

zones. We also provide references for the sources of the progenitor models and for publications in which results from the core-collapse simulations were reported before.

Our compilation includes 3D explosion models with ZAMS masses of 9.0, 9.6, 12.28, 15 (rotating), 18.88, and 20 M_{\odot} as well as non-exploding, BH-forming 40 M_{\odot} and 75 M_{\odot} models. The VERTEX neutrino transport was applied for different

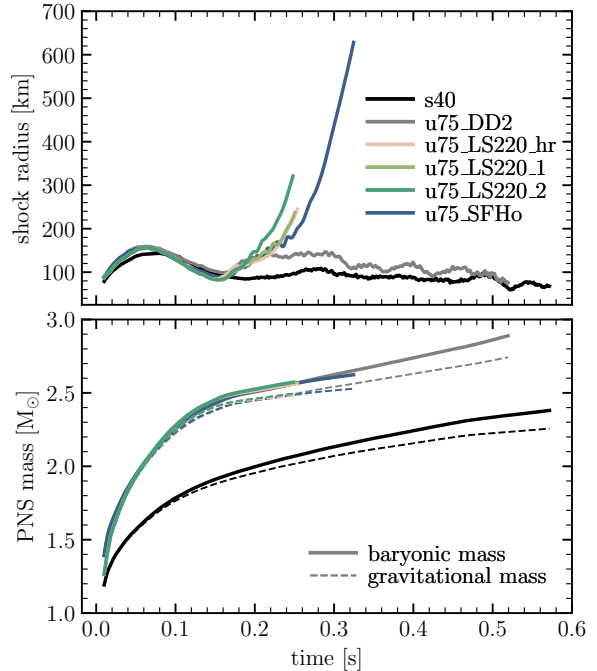


Fig. 2 Angle-averaged shock radii (*top*) and PNS masses (*bottom*) for all BH-forming models. The solid lines show the baryonic PNS masses, the dashed lines the gravitating PNS masses. The lines end when the PNS begins to collapse to a BH

periods of time t_f' and the hydrodynamic modeling was subsequently continued with the NEMESIS scheme until time t_f (Table 2). The shock radii and explosion energies $E_{\text{exp}}^{\text{OB-}}$ are displayed as functions of time in Figure 1. These energies take into account the overburden of stellar material ahead of the SN shock, i.e., the binding energies of the stellar layers exterior to the SN shock are subtracted. At the end of all of the simulations the explosion energies have nearly reached their final values, because their growth rates have become rather small. Correspondingly, the differences between $E_{\text{exp}}^{\text{OB-}}$ and the diagnostic energies $E_{\text{exp}}^{\text{diag}}$ (defined as the total internal plus kinetic plus gravitational energy of all postshock matter with a positive value of this sum) are minor when the computational runs were stopped (Table 2).

For the 12.28 M_{\odot} and 18.88 M_{\odot} stars a final evolution period prior to core collapse (seven minutes for the latter and one hour for the former) were simulated in 3D in order to self-consistently generate asymmetric initial conditions of the density, velocity field, and chemical

composition for the subsequent SN simulations (see [Yadav et al, 2020](#)). Such pre-collapse asymmetries turned out to be crucial for obtaining explosions in these two cases (see [Bollig et al, 2021](#), for the $18.88 M_{\odot}$ model). The $9.0 M_{\odot}$ ([Melson et al, 2020](#); [Stockinger et al, 2020](#)) and $9.6 M_{\odot}$ ([Melson et al, 2015b](#); [Stockinger et al, 2020](#)) models explode rather quickly after core bounce because of their steep temporal decline of the mass infall rate to the stalled shock, whereas the explosion of the $15 M_{\odot}$ progenitor was supported by fairly rapid rotation ([Summa et al, 2018](#)) and that of the $20 M_{\odot}$ progenitor by a minor change in the neutral-current neutrino-nucleon scattering cross sections ([Melson et al, 2015a](#)).

Table 1 lists two variants of both the $15 M_{\odot}$ and the $20 M_{\odot}$ simulations. Each pair is based on the same 3D neutrino-hydrodynamics simulations with the VERTEX transport code applied until t_{f}^{ν} . The main difference between the two cases is a slightly different treatment of the postshock heating and the interior cooling of the PNS with the NEMESIS scheme during the long-time simulations from t_{f}^{ν} until t_{f} . This variation was supposed to test, within plausible limits, the sensitivity of the final SN and NS properties on possible uncertainties of the physics of neutrino heating and cooling during this long-term evolution ([Kresse, 2023](#)).

Several 3D core-collapse simulations of the two very massive 40 and $75 M_{\odot}$ progenitors were performed by A. Summa with different nuclear EoSs and varied angular resolution. The evolution was followed up to the moment when the PNS became gravitationally unstable and started to form a BH (times t_{f}^{ν} in Table 3). Neutrino emission characteristics of two of these simulations were analysed by [Walk et al \(2020\)](#). In the calculation of the $40 M_{\odot}$ progenitor, which employed the LS220 EoS, the shock recedes after it has reached a maximum radius of about 150 km between 50 ms and 100 ms post bounce (Figure 2). A similar behavior is obtained for the $75 M_{\odot}$ progenitor when the DD2 EoS is used. In contrast, with the LS220 and SFHo EoSs the average shock evolves through a minimum radius at ~ 150 ms after bounce but afterwards it exhibits a phase of rapid neutrino-driven expansion until the moment when the PNS begins to collapse to a BH and the simulations were stopped. Since the shock radius hardly exceeds 600 km even in the most extreme

case (Figure 2), all the matter heated by neutrinos is likely to fall back to the BH and successful explosions with SN-like mass ejection cannot be expected to happen in these $75 M_{\odot}$ models (for core-collapse simulations with BH formation and concomitant shock expansion in different kinds of progenitor stars, see, e.g., [Kuroda et al, 2018](#); [Chan et al, 2018](#); [Ott et al, 2018](#); [Chan et al, 2020](#); [Pan et al, 2021](#); [Powell et al, 2021](#); [Rahman et al, 2022](#); [Burrows et al, 2023a](#)). In their 3D calculations of the $40 M_{\odot}$ progenitor, [Burrows et al \(2023a\)](#) obtained an explosion despite BH formation and significant fallback (fallback SN), in contrast to our failed SN for the same progenitor. They attribute this difference to insufficient angular resolution in our CCSN run. This argument, however, is not likely to be the correct explanation, because our 3D simulations of the $75 M_{\odot}$ models with the LS220 EoS do not reveal any significant resolution dependence when runs with 5° and much higher angular resolution using a static mesh refinement (SMR; model `u75_LS220_hr`) are compared (Table 1). Our set of BH forming models also includes two realizations of the $75 M_{\odot}$ simulations with LS220 and 5° resolution that show slightly different shock expansion due to minor differences in the postshock neutrino heating.

2.3 Evaluation for PNS kicks

NSs receive natal kicks connected to their formation in stellar core-collapse events by mass ejection connected to a SN explosion as well as anisotropic neutrino emission. Anisotropic loss of energy in gravitational waves plays a negligible role for kicking the NSs, because the energy carried away by these waves is several orders of magnitude less than the energy lost in neutrinos, which in turn amounts to up to 10% of the rest-mass energy of the compact remnant.

2.3.1 Kick evaluation including the PNS mass evolution

In order to account for the changes of the PNSs mass associated with the neutrino emission, we evaluate the recoil acceleration of the PNS directly from the forces leading to a change of the PNS momentum:

$$\dot{\mathbf{p}}_{\text{NS}} = \underbrace{-\left(\dot{\mathbf{p}}_{\text{gas}} + \dot{\mathbf{p}}_{\nu}^{\text{tot}}\right)}_{\text{accelerating forces (hydro and neutrino)}} - \underbrace{c^{-2}L_{\nu}^{\text{tot}}\mathbf{v}_{\text{NS}}}_{\text{momentum change by neutrino emission in PNS rest frame}}. \quad (2)$$

In this equation L_{ν}^{tot} is the total neutrino luminosity (see Equation 7), \mathbf{v}_{NS} the PNS velocity, and c the speed of light. $\dot{\mathbf{p}}_{\text{gas}}$ is the time derivative of the volume-integrated linear momentum,¹

$$\mathbf{p}_{\text{gas}}(t) = \int_{r>R_{\text{NS}}} dV \rho \mathbf{v}, \quad (3)$$

of the stellar gas exterior to the PNS surface radius at R_{NS} (typically defined at a density of $10^{11} \text{ g cm}^{-3}$), with ρ and \mathbf{v} being the gas density and velocity, respectively. The time derivative of the total linear momentum of the escaping neutrinos, $\dot{\mathbf{p}}_{\nu}^{\text{tot}}$, is evaluated in the rest frame of the PNS, where the neutrino transport of the CCSN models was computed. It can be written as a function of the energy-flux densities \mathbf{F}_{ν_i} of all neutrino species ν_i ($= \nu_e, \bar{\nu}_e, \nu_{\mu}, \bar{\nu}_{\mu}, \nu_{\tau}, \bar{\nu}_{\tau}$) as

$$\dot{\mathbf{p}}_{\nu}^{\text{tot}}(R, t) = \sum_{\nu_i} \dot{\mathbf{p}}_{\nu_i}(R, t) \quad (4)$$

¹In practice, we numerically differentiate the linear gas momentum of the ejecta for Equation (2) with a time-sampling interval of ~ 1 ms.

$$\begin{aligned} &= \frac{R^2}{c} \oint_{r=R} d\Omega \sum_{\nu_i} (\mathbf{F}_{\nu_i} \otimes \hat{\mathbf{r}}) \cdot \hat{\mathbf{r}} \\ &= \frac{R^2}{c} \oint_{r=R} d\Omega \sum_{\nu_i} \mathbf{F}_{\nu_i}(\mathbf{r}, t) \\ &\cong \frac{R^2}{c} \oint_{r=R} d\Omega \sum_{\nu_i} F_{\nu_i}^r(\mathbf{r}, t) \hat{\mathbf{r}}, \quad (5) \end{aligned}$$

where $d\Omega$ is a solid angle element on the sphere of radius R , $\hat{\mathbf{r}}$ the unit vector locally perpendicular to the sphere, and the last line holds as an equality in our analysis, because our RbR+ transport treatment provides only radial components $F_{\nu_i}^r$ of the neutrino energy fluxes. Since the surface integral of Equation (5) has to be evaluated in the free-streaming limit, typically at $R = 400$ km, i.e., far outside the neutrinospheres (Stockinger et al, 2020), any nonradial flux components are negligibly small anyway.² Accordingly, the energy loss rate of the PNS by its neutrino emission (i.e., the direction-averaged total neutrino luminosity) is given by

$$L_{\nu}^{\text{tot}}(R, t) = \sum_{\nu_i} L_{\nu_i}(R, t) \quad (6)$$

$$= R^2 \oint_{r=R} d\Omega \sum_{\nu_i} F_{\nu_i}^r(\mathbf{r}, t). \quad (7)$$

We stress that our evaluation of the NS kick is based on a consideration of the total linear momentum carried away by the escaping neutrinos and by gas exterior to the PNS. Due to momentum conservation, the sum of these two momentum terms must be compensated by the negative momentum received by the NS. For this evaluation it is crucial to compute the neutrino-induced kick *in the free-streaming limit* in order to include the effects of neutrino emission, absorption, and scattering in material outside the neutrinosphere (Stockinger et al, 2020). If, for example, the neutrino kick is evaluated at the neutrinosphere, one misses the contributions from anisotropic neutrino emission, absorption, and scattering that occur in

²Here the neutrino fluxes are those measured in the laboratory frame of a distant observer, not those in the comoving frame of the stellar fluid. Note that the PNS is fixed at the coordinate center of the computational grid for numerical reasons and therefore the rest frame of the PNS is identical with the observer frame.

massive accretion flows around the PNS. Therefore, placing the evaluation radius at different locations can, on the one hand, significantly alter the results for the neutrino-induced PNS kick (as visible by comparing numbers in Coleman and Burrows 2022 and Burrows et al 2023b). On the other hand, the momentum deposited by neutrino interactions in the gas exterior to the neutrinosphere (which for all neutrino species is close to our PNS radius R_{NS}) changes the gas momentum integrated by Equation (3) in the volume $r > R_{\text{NS}}$. This implies a corresponding change of the NS momentum that is inferred from the total gas momentum (according to Equation 2). However, the momentum transferred to the gas in the vicinity of the PNS is subtracted from the momentum carried by the neutrinos, or in other words, the corresponding change of the NS's hydrodynamic kick is compensated by a negative change of the neutrino-induced kick of the PNS, as correctly concluded when the total neutrino momentum is measured at a very large distance from the NS. In contrast, shifting the evaluation radius for the neutrino emission asymmetry to the neutrinosphere instead of placing it in the free streaming regime can imply a double counting of momentum contributions in the neutrino and hydro sectors and can thus lead to an overestimation of the total (neutrino plus hydro) NS kick. We will come back to this point in our later discussion.

The last term on the rhs of Equation (2) accounts for the change of the PNS's momentum due to fact that neutrinos leaving the moving PNS carry away linear momentum in the observer frame, because the term $-c^{-2}L_{\nu}^{\text{tot}}\mathbf{v}_{\text{NS}}$ denotes the rate of momentum loss connected to the mass equivalent of the rate of neutrino energy loss by the PNS. As we will see in the following, this term will ensure that the PNS's velocity does not change in the case external forces on the PNS are absent, the baryonic mass of the PNS, $M_{\text{NS,b}}$ is constant, but the PNS radiates neutrinos isotropically in its rest frame and accordingly its gravitational mass, $M_{\text{NS,g}}$ changes with time.

Generally, the temporal variation of the PNS's momentum can be caused by changes of the PNS's velocity and gravitational mass:

$$\begin{aligned}\dot{\mathbf{p}}_{\text{NS}} &= M_{\text{NS,g}}\dot{\mathbf{v}}_{\text{NS}} + \dot{M}_{\text{NS,g}}\mathbf{v}_{\text{NS}} \\ &= M_{\text{NS,g}}\dot{\mathbf{v}}_{\text{NS}} + \left(\dot{M}_{\text{NS,b}} - c^{-2}L_{\nu}^{\text{tot}}\right)\mathbf{v}_{\text{NS}},\end{aligned}\quad (8)$$

where in the second line we have introduced the reduction of the gravitational mass by neutrino emission and the time derivative of the baryonic mass indicates possible mass gain or loss by the PNS through accretion or neutrino-driven outflows, respectively. The baryonic mass of the PNS, $M_{\text{NS,b}}(t)$, is obtained by integrating the baryon number density, multiplied with the average nucleon rest mass, over the PNS volume interior to the PNS radius $R_{\text{NS}}(t)$ at a density of $10^{11} \text{ g cm}^{-3}$. The time-dependent gravitational PNS mass, $M_{\text{NS,g}}(t)$, is related to this mass by subtracting the mass equivalent corresponding to the energy loss via neutrino emission:

$$M_{\text{NS,g}}(t) = M_{\text{NS,b}}(t) - \frac{1}{c^2} \int_{t_i}^t dt' L_{\nu}^{\text{tot}}(t'), \quad (9)$$

taking as starting point t_i of the time integration the beginning of the PROMETHEUS-VERTEX simulations to include the (small) neutrino energy loss during the collapse of the degenerate stellar core before core bounce (i.e., $t = 0$). Now combining Equations (2) and (8), we get for the PNS acceleration:

$$\dot{\mathbf{v}}_{\text{NS}}(t) = -\frac{\dot{\mathbf{p}}_{\text{gas}}(t) + \dot{\mathbf{p}}_{\nu}^{\text{tot}}(t)}{M_{\text{NS,g}}(t)} - \frac{\dot{M}_{\text{NS,b}}(t)\mathbf{v}_{\text{NS}}(t)}{M_{\text{NS,g}}(t)}. \quad (10)$$

From this equation we can verify what we mentioned above: If no hydrodynamic forces act on the PNS, i.e., $\dot{\mathbf{p}}_{\text{gas}} = 0$, and the PNS radiates neutrinos isotropically in its rest frame, i.e., $\dot{\mathbf{p}}_{\nu}^{\text{tot}} = 0$, and the baryonic PNS mass is constant, i.e., $\dot{M}_{\text{NS,b}} = 0$, the PNS is not accelerated, $\dot{\mathbf{v}}_{\text{NS}} = 0$, and the PNS's velocity \mathbf{v}_{NS} is therefore constant in time, too.

In practise, we separate this equation into expressions for the accelerations connected to the hydrodynamic kick and the neutrino-induced kick. The recoil acceleration due to the hydrodynamic PNS kick is given by

$$\begin{aligned}\dot{\mathbf{v}}_{\text{NS}}^{\text{hyd}}(t) &= -\frac{\dot{\mathbf{p}}_{\text{gas}}(t)}{M_{\text{NS,g}}(t)} - \frac{\dot{M}_{\text{NS,b}}(t)\mathbf{v}_{\text{NS}}^{\text{hyd}}(t)}{M_{\text{NS,g}}(t)} \\ &\simeq -\frac{\dot{\mathbf{p}}_{\text{gas}}(t)}{M_{\text{NS,g}}(t)},\end{aligned}\quad (11)$$

and, in analogy, the recoil acceleration leading to the neutrino-induced PNS kick velocity is given by

$$\begin{aligned}\dot{\mathbf{v}}_{\text{NS}}^{\nu}(t) &= -\frac{\dot{\mathbf{p}}_{\nu}^{\text{tot}}(t)}{M_{\text{NS,g}}(t)} - \frac{\dot{M}_{\text{NS,b}}(t)\mathbf{v}_{\text{NS}}^{\nu}(t)}{M_{\text{NS,g}}(t)} \\ &\simeq -\frac{\dot{\mathbf{p}}_{\nu}^{\text{tot}}(t)}{M_{\text{NS,g}}(t)}.\end{aligned}\quad (12)$$

The approximate expressions in the second lines of Equations (11) and (12) neglect the term $\propto \dot{M}_{\text{NS,b}}\mathbf{v}_{\text{NS}}$. This is well justified most of the time, because during the early postbounce evolution, during which the baryonic mass of the PNS grows rapidly by accretion, \mathbf{v}_{NS} is still small, and at late postbounce times, i.e., later than ~ 1 s after bounce, the baryonic PNS mass is effectively constant. In our standard procedure for the numerical post-processing of the core-collapse simulations, the hydrodynamic kicks and neutrino-induced kicks of the PNSs are determined by time integration of the accelerations in Equations (11) and (12), neglecting the terms $\propto \dot{M}_{\text{NS,b}}\mathbf{v}_{\text{NS}}$:

$$\mathbf{v}_{\text{NS}}^{\text{hyd}}(t) = \int_0^t dt' \dot{\mathbf{v}}_{\text{NS}}^{\text{hyd}}(t'), \quad (13)$$

$$\mathbf{v}_{\text{NS}}^{\nu}(t) = \int_0^t dt' \dot{\mathbf{v}}_{\text{NS}}^{\nu}(t'), \quad (14)$$

with time zero being typically at core bounce. Correspondingly, we obtain the total PNS kick velocity as function of time, $\mathbf{v}_{\text{NS}}^{\text{tot}}(t)$ as the vector sum of $\mathbf{v}_{\text{NS}}^{\text{hyd}}(t)$ and $\mathbf{v}_{\text{NS}}^{\nu}(t)$:

$$\mathbf{v}_{\text{NS}}^{\text{tot}}(t) = \mathbf{v}_{\text{NS}}^{\text{hyd}}(t) + \mathbf{v}_{\text{NS}}^{\nu}(t). \quad (15)$$

Solving Equations (11) and (12) including the terms $\propto \dot{M}_{\text{NS,b}}\mathbf{v}_{\text{NS}}$ for the hydrodynamic and neutrino-induced PNS kick velocities $\mathbf{v}_{\text{NS}}^{\text{hyd}}(t)$ and $\mathbf{v}_{\text{NS}}^{\nu}(t)$, e.g., with a Runge-Kutta integrator, yields results that differ from the ones obtained with our standard, slightly more approximate evaluation by less than $\sim(2-3)\%$ in all models and at any time during their evolution. Such small deviations are on the same level as the numerical inaccuracies connected to the discretized computations of the time derivatives and integrals of the strongly fluctuating force vectors $\dot{\mathbf{p}}_{\text{gas}}(t)$ and $\dot{\mathbf{p}}_{\nu}^{\text{tot}}(t)$. In the figures and tables of this paper we will therefore present results where the terms $\propto \dot{M}_{\text{NS,b}}\mathbf{v}_{\text{NS}}$ are

neglected in Equations (11) and (12). In the following we will hint at this minor limitation of accuracy by denoting the total NS kick velocities with $\mathbf{v}_{\text{NS}}^{\text{tot}}$ instead of \mathbf{v}_{NS} .

2.3.2 Approximate estimates

As said before, the time integrals of Equations (13) and (14) permit us to include the temporal variation of the inertial/gravitational PNS mass in the kick calculations. Alternatively, hydrodynamic and neutrino kick velocities can be estimated by considering global momentum conservation in the observer frame of reference, balancing the NS momentum, \mathbf{p}_{NS} , and the gas plus neutrino momentum, $\mathbf{p}_{\text{gas}} + \mathbf{p}_{\nu}^{\text{tot}}$, as done by [Scheck et al \(2006\)](#); [Wongwathanarat et al \(2013\)](#); [Gessner and Janka \(2018\)](#); [Stockinger et al \(2020\)](#), and [Bollig et al \(2021\)](#). This approach is suitable to obtain estimates of the kick velocities in very good agreement with those from the analysis of Section 2.3.1 at early postbounce times when the baryonic and the gravitational PNS mass are still very similar. Minor differences between the results from Equation (15) and Equation (17) below during this phase are mostly connected to inaccuracies of the numerical integration, because the direction and absolute value of the PNS acceleration still fluctuate wildly due to the violently turbulent gas flows in the postshock layer. At later times, when the PNS acceleration has developed a preferred direction, both calculations disagree up to about 10%, corresponding to the typical relative difference of gravitational and baryonic NS mass.

In Figures A1–C15 in Appendix A, which provide detailed information for most of our core-collapse simulations with explosions or BH formation, we also show for comparison the evolution of the hydrodynamic kick and total (i.e., hydrodynamic plus neutrino) kick computed approximately from the total gas momentum according to momentum conservation:

$$\mathbf{v}_{\text{NS}}^{\text{hyd,mc}}(t) = -\frac{\mathbf{p}_{\text{gas}}(t)}{M_{\text{NS,b}}(t)}, \quad (16)$$

$$\mathbf{v}_{\text{NS}}^{\text{tot,mc}}(t) = -\frac{\mathbf{p}_{\text{gas}}(t) + \mathbf{p}_{\nu}^{\text{tot}}(t)}{M_{\text{NS,b}}(t)}. \quad (17)$$

Dividing by the baryonic PNS mass in Equations (16) and (17) ensures that the velocity of the PNS does not change in the absence of

accelerating forces when its gravitational mass decreases due to isotropic neutrino emission in the PNS's rest frame. However, these estimates usually lead to lower bounds on the actual kicks and they work best in the extreme case that the accelerating forces act very fast and early when the mass decrement of the PNS by neutrino emission is still small. In contrast, dividing the total momentum by the gravitational mass, $\mathbf{v}_{\text{NS}}^{\text{upper}}(t) = -(\mathbf{p}_{\text{gas}}(t) + \mathbf{p}_{\nu}^{\text{tot}}(t))/M_{\text{NS,g}}(t)$, tends to yield an upper bound of the NS kick; this approximation would work well if the NS acceleration happened mainly after the PNS has radiated most of its gravitational binding energy in neutrinos and therefore the inertial (gravitational) mass of the NS has converged to its final value. The true kick velocities evaluated via time integration of Equations (10), (11), and (12) lie between these lower and upper limits.

2.3.3 Forces of the hydro kicks

According to [Scheck et al \(2006\)](#) the hydrodynamic force kicking the PNS can be separated into different contributions corresponding to the momentum transfer to the PNS by (a) the pressure of surrounding gas, (b) momentum carried by the accretion flows or outflows, and (c) the action of gravitational forces between the PNS and the matter of the collapsing and exploding star. Integrating the Euler equation over the relevant volume exterior to a radius R_0 around the PNS, one obtains:

$$\begin{aligned} \dot{\mathbf{p}}_{\text{hyd}} &= -\dot{\mathbf{p}}_{\text{gas}} = \dot{\mathbf{p}}_{\text{pres}} + \dot{\mathbf{p}}_{\text{mom}} + \dot{\mathbf{p}}_{\text{grav}} \\ &= -\oint_{r=R_0} dS P \hat{\mathbf{r}} - \oint_{r=R_0} dS \rho (\mathbf{v} \otimes \mathbf{v}) \cdot \hat{\mathbf{r}} \\ &\quad + \int_{r>R_0} dm GM_{\text{NS}} \frac{\hat{\mathbf{r}}}{r^2}, \end{aligned} \quad (18)$$

where $dS = R_0^2 d\Omega$ is the surface element with solid angle $d\Omega$ on the sphere of radius R_0 , $P = P(|\mathbf{r}| = R_0, t)$ is the gas pressure on the sphere, and the term $\rho(\mathbf{v} \otimes \mathbf{v}) \cdot \hat{\mathbf{r}} = \rho \mathbf{v} v_r$ denotes the momentum flux of gas flowing radially inward or outward through this sphere. By default we use $R_0 = 2 R_{\text{NS}}$, where R_{NS} is the PNS radius corresponding to an angle-averaged density of $10^{11} \text{ g cm}^{-3}$. This choice is justified by the fact that in all cases this radius of evaluation yields excellent agreement of the time-integrated vector sum of the three force

contributions, $\int_0^t \dot{\mathbf{p}}_{\text{hyd}} dt'$, and the negative of the total gas momentum $-\mathbf{p}_{\text{gas}}$ of the ejecta according to Equation (3). Minor discrepancies occur only in phases when the absolute value of the NS kick velocity is very small and thus sensitive to low-amplitude variations and minor numerical discretization errors. The agreement becomes considerably worse in some cases when R_0 is moved to other locations between $\sim R_{\text{NS}}$ and $\sim 3 R_{\text{NS}}$. Moreover, inappropriate choices of R_0 also cause quantitative changes of the three terms added up in Equation (18). This may lead to incorrect conclusions drawn from the entire analysis. In particular the magnitudes of the pressure and momentum flux terms are quite sensitive to the radius where they are evaluated. We will come back to the critical role of the force-evaluation radius in the context of neutrino-induced kicks in Section 3.2.2.

Any significant acceleration of the PNS by pressure forces and momentum transfer through gas flows requires sufficiently dense gas in the close vicinity of the PNS. Therefore, these forces are relevant only during the early postbounce phase and shortly after the onset of the SN explosion. During this period the hydrodynamic PNS kick just starts to develop and all of the three forces contributing in Equation (18) have similar magnitudes and partly cancel each other due to opposite signs ([Scheck et al, 2006](#)). Gravitational forces, in contrast, are important during all of the evolution. In particular, because of its long-range and non-saturating nature, gravity can play a role still at late time after the beginning of the explosion (see the long-time CCSN simulations discussed by [Janka et al, 2022](#)). Most of the hydrodynamic PNS kick is therefore transferred to the PNS once the explosion has attained its final asymmetry and a preferred kick direction has developed, and a major fraction of the asymptotic value of the PNS velocity due to the hydrodynamic kick can be attributed to the action of gravitational forces between the PNS and the matter ejected by the SN. We will again verify this fact in the simulations discussed in the next section. For this reason the hydrodynamic PNS kick has been termed

“gravitational tugboat” effect (Wongwathanarat et al, 2013).³

2.3.4 Asymmetry parameters

The hydrodynamic and neutrino kicks of the PNSs can be related to the asymmetry of the SN ejecta and neutrino emission by dimensionless asymmetry parameters.

For the hydrodynamic kicks one sets the total linear momentum of the gas exterior to the PNS, $\mathbf{p}_{\text{gas}}(t)$ (Equation 3), in relation to the scalar quantity

$$p_{\text{ej}}(t) = \int_{R_{\text{NS}}}^{R_s} dV \rho |\mathbf{v}|, \quad (19)$$

which represents the total momentum of the gas between the PNS surface and the direction-dependent shock radius R_s . With both of these quantities one can define the momentum-asymmetry parameter of the ejecta by

$$\bar{\alpha}_{\text{ej}}(t) = \frac{|\mathbf{p}_{\text{gas}}(t)|}{p_{\text{ej}}(t)} \quad (20)$$

(Janka and Müller 1994; Scheck et al 2006; Janka 2017; Gessner and Janka 2018; Janka et al 2022). The values of $\bar{\alpha}_{\text{ej}}(t)$ for our 3D CCSN simulations at the end of the computational runs at times $t = t_f$ are listed in Table 2.

Using this parameter and Equation (16), the kick velocity deduced from momentum conservation can be recovered: $v_{\text{NS}}^{\text{hyd,mc}}(t) = |\mathbf{v}_{\text{NS}}^{\text{hyd,mc}}(t)| = \bar{\alpha}_{\text{ej}}(t) p_{\text{ej}}(t) M_{\text{NS,b}}^{-1}(t)$. One should note that the numerical value of $\bar{\alpha}_{\text{ej}}(t)$ exhibits considerable variation in time with the general tendency to decrease during the long-time evolution of the SN explosions, because $|\mathbf{p}_{\text{gas}}|$ converges to a constant value when the ejecta decouple from the PNS hydrodynamically and gravitationally, whereas $p_{\text{ej}}(t)$ continues to grow until the SN shock breaks out from the stellar surface and the ejecta reach homologous expansion. Janka (2017) derived a simple scaling relation $v_{\text{NS}}^{\text{hyd,mc}} \propto \bar{\alpha}_{\text{ej}} E_{\text{exp}} M_{\text{NS}}^{-1}$, which connects the hydrodynamic kick with the explosion energy E_{exp} and the ejecta asymmetry $\bar{\alpha}_{\text{ej}}$. The scaling factor in this relation together with the normalization of $\bar{\alpha}_{\text{ej}}$ depend on the phase

³This naming has been criticized as inappropriate in some recent papers (Coleman and Burrows, 2022; Burrows et al, 2023b).

of the SN evolution, which has to be specified in order to compare explosion asymmetries of different SN models.

Also for the neutrino-induced NS kicks time-dependent parameters $\alpha_{\nu}(t)$ and $\bar{\alpha}_{\nu}(r)$ can be introduced, following Janka and Müller (1994), Gessner and Janka (2018), and Stockinger et al (2020). These parameters characterize the neutrino emission asymmetry that leads to a net linear momentum associated with the energy carried away by the neutrinos escaping the NS. For the instantaneous value of a quantity defined in this way we can write

$$\alpha_{\nu_i}(R, t) = c \frac{|\dot{\mathbf{p}}_{\nu_i}(R, t)|}{L_{\nu_i}(R, t)}, \quad (21)$$

$$\alpha_{\nu}^{\text{tot}}(R, t) = c \frac{|\dot{\mathbf{p}}_{\nu}^{\text{tot}}(R, t)|}{L_{\nu}^{\text{tot}}(R, t)}, \quad (22)$$

using the linear momenta associated with the neutrino emission as defined in Equations (4) and (5) and the neutrino luminosities as given by Equations (6) and (7). Time averages of these anisotropy parameters of the neutrino emission can be obtained by integrating the terms in the numerators and denominators over the time intervals of interest, for example $[0, t]$ for the evolution between core bounce and moment t :

$$\bar{\alpha}_{\nu_i}(R, t) = c \frac{|\int_0^t dt' \dot{\mathbf{p}}_{\nu_i}(R, t')|}{\int_0^t dt' L_{\nu_i}(R, t')}, \quad (23)$$

$$\bar{\alpha}_{\nu}^{\text{tot}}(R, t) = c \frac{|\int_0^t dt' \dot{\mathbf{p}}_{\nu}^{\text{tot}}(R, t')|}{\int_0^t dt' L_{\nu}^{\text{tot}}(R, t')}. \quad (24)$$

The values of these parameters at the end of the 3D neutrino transport simulations with the VERTEX code at times $t = t_f'$ are listed in Table 3.

With the time-averaged neutrino asymmetry parameter $\bar{\alpha}_{\nu}^{\text{tot}}$ defined above, we can estimate an upper bound of the neutrino-induced kick by assuming that $\bar{\alpha}_{\nu}^{\text{tot}}$ remains constant during the evolution that follows after the VERTEX neutrino transport calculation has ended. Thus extrapolating, we get

$$\begin{aligned} \tilde{v}_{\text{NS}}^{\nu, \infty} &= v_{\text{NS}}^{\nu}(t_f') + \frac{\bar{\alpha}_{\nu}^{\text{tot}}(t_f')}{c} \int_{t_f'}^{\infty} dt' \frac{L_{\nu}^{\text{tot}}(t')}{M_{\text{NS,g}}(t')} \\ &\cong \frac{\bar{\alpha}_{\nu}^{\text{tot}}}{c} \int_0^{\infty} dt' \frac{L_{\nu}^{\text{tot}}(t')}{M_{\text{NS,g}}(t')}. \end{aligned} \quad (25)$$

for an approximate estimate of the final value, provided the neutrino emission asymmetry $\bar{\alpha}_\nu^{\text{tot}} \equiv \bar{\alpha}_\nu^{\text{tot}}(t_f^\nu)$ averaged from core bounce until time t_f^ν also holds later on. In our analysis we make use of the expression in the first line of Equation (25). The second line applies to a high degree of accuracy when the variation of gravitational mass of the PNS mass is small during the time interval $[0, t_f^\nu]$.⁴ In Equation (25), the time integration is performed until the PNS has effectively radiated its entire gravitational binding energy in neutrinos, which in all of our simulations is beyond the time t_f when the 3D CCSN simulation was stopped. However, data from 1D PNS cooling simulations with PROMETHEUS-VERTEX including a mixing-length treatment of PNS convection were available for much longer periods (see Fiorillo et al, 2023) and allowed us to carry out the time integration of Equation (25) until the hot PNS has become a cold, neutrino-transparent NS.

The neutrino anisotropy parameters can be directly used to express the momentum transfer to the PNS by its asymmetric neutrino emission in terms of the corresponding energy loss in neutrinos:

$$|\dot{\mathbf{p}}_\nu^{\text{tot}}(t)| = \alpha_\nu^{\text{tot}}(t) \frac{L_\nu^{\text{tot}}(t)}{c}, \quad (26)$$

$$|\mathbf{p}_\nu^{\text{tot}}(t)| = \bar{\alpha}_\nu^{\text{tot}}(t) \frac{E_\nu^{\text{tot}}(t)}{c}, \quad (27)$$

with $E_\nu^{\text{tot}}(t) = \int_0^t dt' L_\nu^{\text{tot}}(t')$.⁵ Moreover, ignoring the (relatively small) variation of the gravitational PNS mass in the integrand of Equation (14) (with Equation 12) relative to the baryonic PNS mass, we can approximately write for the NS's neutrino kick velocity

$$v_{\text{NS}}^\nu(t) = |\mathbf{v}_{\text{NS}}^\nu(t)| \approx \frac{\bar{\alpha}_\nu^{\text{tot}}(t)}{c} \frac{E_\nu^{\text{tot}}(t)}{M_{\text{NS,b}}(t)}. \quad (28)$$

⁴In general, the effect of the variation of the gravitational mass of the PNS compared to its baryonic mass is a subdominant effect, which affects the neutrino kicks only on the level of about 10 percent.

⁵The small difference of the total neutrino energy loss when starting the time integration at core bounce ($t = 0$) or at the beginning of the CCSN simulation (i.e., at time t_i) does not matter in this context, because the neutrino emission prior to core bounce is essentially isotropic in all cases.

Using this, one obtains a simple estimate of the neutrino kick (e.g. Gessner and Janka, 2018):

$$v_{\text{NS}}^\nu \approx 167 \frac{\text{km}}{\text{s}} \frac{\bar{\alpha}_\nu^{\text{tot}}}{0.005} \frac{E_\nu^{\text{tot}}}{3 \times 10^{53} \text{ erg}} \left(\frac{M_{\text{NS,b}}}{1.5 M_\odot} \right)^{-1}, \quad (29)$$

which implies that an 0.5% long-time (net) asymmetry of the neutrino emission, e.g., due to PNS convection and LESA or asymmetric accretion, can lead to a NS kick of typically around 150 km s^{-1} .

If the total neutrino luminosity has a dipole asymmetry, i.e.,

$$\frac{dL_\nu^{\text{tot}}}{d\Omega} = \frac{L_\nu^{\text{tot}}}{4\pi} (1 + a_d \cos \theta), \quad (30)$$

where a_d is the normalized amplitude of the dipole component, then the surface integral of Equation (5) yields

$$\dot{\mathbf{p}}_\nu^{\text{tot}} = |\dot{\mathbf{p}}_\nu^{\text{tot}}| = \alpha_\nu^{\text{tot}} \frac{L_\nu^{\text{tot}}}{c} = \frac{a_d}{3} \frac{L_\nu^{\text{tot}}}{c}, \quad (31)$$

which means that $\alpha_\nu^{\text{tot}} = a_d/3$. A value of 0.5% for $\bar{\alpha}_\nu^{\text{tot}}$ as considered in Equation (29) therefore implies an emission dipole of 1.5% of the monopole.

Table 2 Hydrodynamic PNS kicks and explosion energies of 3D SN models

Model	t_f^ν [s]	t_f [s]	$M_{\text{NS,b}}^f$ [M_\odot]	$M_{\text{NS,g}}^f$ [M_\odot]	$M_{\text{NS,g}}^\infty$ [M_\odot]	$v_{\text{NS}}^{\text{hyd}}$ [km/s]	v_{NS}^ν [km/s]	$v_{\text{NS}}^{\text{tot}}$ [km/s]	$\bar{\alpha}_{\text{ej}}$	$\theta_{\text{hyd}}^{\nu,f}$ [$^\circ$]	$\theta_{\text{spin}}^{\text{kick}}$ [$^\circ$]	P_{NS} [ms]	$E_{\text{exp}}^{\text{diag}}$ [B]	$E_{\text{exp}}^{\text{OB-}}$ [B]
s9.0	0.488	3.936	1.355	1.255	1.240	30.4	44.4	57.0	0.095	82.4	135.4	1,518	0.054	0.052
z9.6	0.450	1.450	1.350	1.290	1.237	10.4	49.4	59.6	0.039	12.1	140.7	1,715	0.086	0.086
s12.28	4.139	4.139	1.551	1.429	1.402	243.1	138.6	301.5	0.173	79.3	70.8	7.5	0.228	0.190
m15	0.457	7.433	1.605	1.427	1.416	627.0	54.4	621.1	0.196	98.8	80.4	2.1	0.332	0.281
m15e	0.457	8.002	1.583	1.405	1.396	561.6	54.4	549.0	0.147	106.1	60.9	2.1	0.436	0.394
s18.88	1.675	8.360	1.878	1.657	1.652	462.3	95.7	506.5	0.074	67.7	145.1	7.8	1.000	0.938
s20	0.506	8.038	1.949	1.698	1.690	1291.5	55.0	1305.5	0.167	76.4	89.9	36.3	1.229	1.157
s20e	0.506	7.980	1.912	1.663	1.655	878.5	55.0	918.8	0.100	44.2	48.7	316.1	1.431	1.361

Note: t_f^ν and t_f are the postbounce times at the end of the full-transport simulation with PROMETHEUS-VERTEX and at the end of the NEMESIS extension run, respectively; $M_{\text{NS,b}}^f$ and $M_{\text{NS,g}}^f$ are the final baryonic mass and gravitational mass (Equation 9) of the NS at time t_f ; $M_{\text{NS,g}}^\infty$ is the corresponding final gravitational NS mass for $t \rightarrow \infty$ (assuming $M_{\text{NS,b}}(t) = \text{const}$ for $t > t_f$); $v_{\text{NS}}^{\text{hyd}}$ is the magnitude of the hydrodynamic NS kick velocity at $t = t_f$ (Equation 13), v_{NS}^ν that of the neutrino-induced NS kick velocity at $t = t_f^\nu$ (Equation 14; see Table 3 for estimated upper bounds of the neutrino-induced kick velocity for $t \rightarrow \infty$), and $v_{\text{NS}}^{\text{tot}}$ is the total computed NS kick velocity as the absolute value of the vector sum of $\mathbf{v}_{\text{NS}}^{\text{hyd}}(t_f)$ and $\mathbf{v}_{\text{NS}}^\nu(t_f^\nu)$; $\bar{\alpha}_{\text{ej}}$ is the anisotropy parameter of the SN ejecta (Equation 20) at time t_f ; $\theta_{\text{hyd}}^{\nu,f} = \theta(\mathbf{v}_{\text{NS}}^{\text{hyd}}(t_f), \mathbf{v}_{\text{NS}}^\nu(t_f^\nu))$ is the angle between the hydrodynamic NS kick vector (at $t = t_f$) and the neutrino-induced NS kick vector (at $t = t_f^\nu$); $\theta_{\text{spin}}^{\text{kick}} = \theta(\mathbf{J}, \mathbf{v})$ is the angle between the NS spin vector and its kick vector at $t = t_f$; P_{NS} is the NS spin period at $t = t_f$ (evaluated as described in Appendix D of Stockinger et al 2020 with an assumed final radius of the cold NS of 12 km; see also Kresse 2023); $E_{\text{exp}}^{\text{diag}}$ and $E_{\text{exp}}^{\text{OB-}}$ are the final diagnostic explosion energy (i.e., the integrated gravitational plus kinetic plus internal energy of all gas between PNS radius and shock radius with a positive value of this total energy) and the final explosion energy with the overburden energy (i.e., the binding energy of stellar matter outside of the SN shock) subtracted, both computed at $t = t_f$. 1 B = 1 bethe = 10^{51} erg.

3 Results

In the following we will first discuss our results for hydrodynamic NS kicks due to asymmetric mass ejection and will compare them to the neutrino-induced NS kicks caused by asymmetric neutrino emission. Subsequently, we will elaborate on the neutrino kicks of NSs and BHs in somewhat more detail, based on a time-dependent analysis of all of the discussed models.

3.1 Hydrodynamic kicks

Table 2 provides an overview of parameters that characterize the explosions and NS properties (masses, kicks, and spins) of our set of 3D SN models. The explosion energies have nearly reached saturation at the end of our long-term simulations. The values of $E_{\text{exp}}^{\text{OB-}}$ include the remaining (negative) binding energy of stellar shells exterior to the shock. In all of the listed cases this overburden energy makes less than $\sim 15\%$ of the “diagnostic” explosion energy $E_{\text{exp}}^{\text{diag}}$ (for a definition, see the notes of Table 2) of the postshock gas. The values of $E_{\text{exp}}^{\text{OB-}}$ span a wide range from about 5×10^{49} erg for the lowest-mass progenitor to close to 1.4×10^{51} erg for the $20 M_{\odot}$ models (see also Figure 1). The explosion energy grows monotonically with the progenitor’s ZAMS mass and compactness $\xi_{2.5}$ (Equation 1 and Table 1) in our limited set of models.

The final gravitational NS masses are between $\sim 1.24 M_{\odot}$ and $\sim 1.70 M_{\odot}$, depending on the progenitor and, as a secondary effect, on the explosion energy. The middle panel of Figure 1 shows the time evolution of both the NS baryonic masses and the corresponding gravitational masses. In our set of models lower-mass progenitors give birth to lower-mass NSs, but this dependence can also be non-monotonic because of a non-monotonic relation between the core structure of pre-collapse stars and the ZAMS mass (Sukhbold and Woosley, 2014; Sukhbold et al, 2018). More energetic neutrino-driven explosions typically correlate with higher NS masses because of the higher neutrino luminosities and more matter being heated by neutrinos (Nakamura et al, 2015; Burrows and Vartanyan, 2021), but more energetic explosions for the same progenitor lead to slightly lower NS masses (Table 2).

The hydrodynamic NS kicks are expected to scale with the explosion energy and the explosion asymmetry:

$$v_{\text{NS}}^{\text{hyd}} \propto \bar{\alpha}_{\text{ej}} E_{\text{exp}} \quad (32)$$

(Equation 11 in Janka, 2017). This expectation is compatible with our results of Table 2 and those of Burrows et al (2023b). The low-mass progenitors, which explode with the lowest energies, also develop small ejecta asymmetries (measured by $\bar{\alpha}_{\text{ej}}$ of Equation 20) because of their explosion early after core bounce and their rapid ejecta expansion (see the discussion in, e.g., Gessner and Janka, 2018; Müller et al, 2019; Stockinger et al, 2020; Burrows et al, 2023b). Therefore their hydrodynamic kicks asymptote to their final values within only 1–2 s (Figure 3) and at only a few 10 km s^{-1} . Our explosion models for the 12.28, 15, and $18.88 M_{\odot}$ progenitors reach hydro kicks of $240\text{--}630 \text{ km s}^{-1}$ until the simulations were stopped, but there is a trend of monotonic increase continuing beyond this time (Figure 3). The two explosion models of the $20 M_{\odot}$ progenitor develop the highest explosion energies and therefore also the biggest hydro kicks of nearly 900 km s^{-1} and 1300 km s^{-1} with considerable growth rates even after 8 s, in particular in the model with the most extreme NS kick. This model is likely to reach a NS kick of around 1500 km s^{-1} in the end.

It is interesting that in the two rotating models, m15 and m15e, the explosion is strongest close to the equatorial plane due to a powerful spiral mode of the standing accretion shock instability (spiral SASI; Blondin and Mezzacappa, 2007) driving the onset of shock expansion in this simulation (see Summa et al, 2018). For this reason an explosion with a pronounced hemispheric asymmetry *perpendicular* to the rotation axis develops, i.e., the ejecta expand most strongly around the equator and possess a sizable dipolar deformation. Therefore, in contrast to naive expectations based on 2D simulations of rotation-supported explosions, the hydrodynamic NS kicks in these 3D simulations have big inclination angles relative to the rotation axis of the $15 M_{\odot}$ progenitor. The relative angles between the progenitor’s spin vector and the vector direction of the NS’s final hydro kicks are 81.1° for model m15 and 61.5° for model m15e. These angles are close to those between the NS spin and kick vectors of models m15 and m15e (see Table 2), because the NS spin directions are

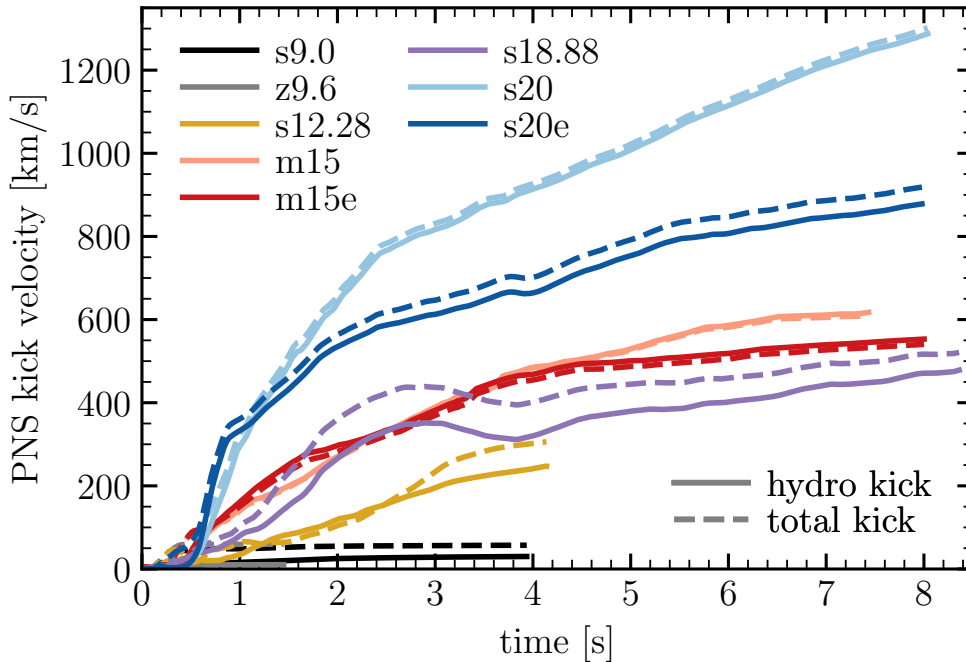


Fig. 3 Evolution of the PNS kick velocities in all successfully exploding 3D models. The solid lines show the hydrodynamic PNS kick velocities, the dashed lines display the total PNS kick velocities as the vector sums of hydrodynamic plus neutrino-induced kick velocities. Note that the neutrino kick velocity vector is fixed here to the results obtained at the end of the VERTEX neutrino transport calculations (at t_f^ν ; Tables 2 and 3)

basically identical with the spin axis of the progenitor, and the total (hydro plus neutrino) kicks of the NSs are far dominated by the hydrodynamic kicks. In model m15 (and m15e) also the neutrino-induced kick is near the equatorial plane at time t_f^ν when the VERTEX neutrino transport was switched off; the angle between the progenitor’s spin vector and the neutrino-kick vector is 92.3° .

Table 2 also provides the values of the neutrino-induced NS kicks at times t_f^ν . These values and the corresponding kick directions are fixed when plotting the subsequent evolution of the total kicks in Figure 3. The neutrino kicks at times t_f^ν are typically lower estimates of the final values. We also list our estimates of the possible final neutrino-kick velocities, $\tilde{v}_{\text{NS}}^{\nu, \infty}$, in Table 3 and plot them in Figure 4. They are obtained by using Equation (25), i.e., by making the assumption that the neutrino emission asymmetry averaged from core bounce until time t_f^ν also holds for the entire later PNS neutrino cooling phase. The values thus obtained can be considered as crude extrapolation

for the long-time evolution of the neutrino kicks.⁶ In Figure 4 we also estimate the final total NS kicks by adding the hydro kicks at the end points of our simulations, t_f , and our extrapolated values of the neutrino kicks, assuming that the vector directions of the neutrino kicks at times t_f^ν remain unchanged during the later neutrino emission.

Figure 4 visualizes our progenitor dependent results for hydrodynamic, neutrino, and total kicks graphically; successfully exploding models are shown in the left panel. In the cases of the low-mass models s9.0 and z9.6 the total kicks ($|\boldsymbol{v}_{\text{NS}}^{\text{tot}}|$ and $|\tilde{\boldsymbol{v}}_{\text{NS}}^{\text{tot}}|$) are clearly dominated by the neutrino-induced kicks, in the intermediate-mass

⁶Most extreme upper limits may be obtained by replacing $\bar{\alpha}_\nu^{\text{tot}}(t_f^\nu)$ in Equation (25) by $\alpha_\nu^{\text{tot}}(t_f^\nu)$ (averaged over a time interval of several 10 ms near t_f^ν , using Equation 24). The thus computed values for the neutrino kicks extrapolated to very late times can be up to about a factor of two greater than those listed for $\tilde{v}_{\text{NS}}^{\nu, \infty}$ in Table 3 in models where dense, neutrino absorbing, asymmetric gas flows around the NS exist until late after bounce (i.e., m15, s18.88, s20). However, we consider these values as unrealistically high upper bounds, because the directions of such flow asymmetries are usually strongly time dependent. Therefore the neutrino emission asymmetry in the free-streaming limit exhibits considerable directional fluctuations in time, and the time-averaged neutrino emission asymmetry $\bar{\alpha}_\nu^{\text{tot}}(t)$ is usually much lower than the instantaneous values $\alpha_\nu^{\text{tot}}(t)$ (see Section 3.2.1 and Appendix A).

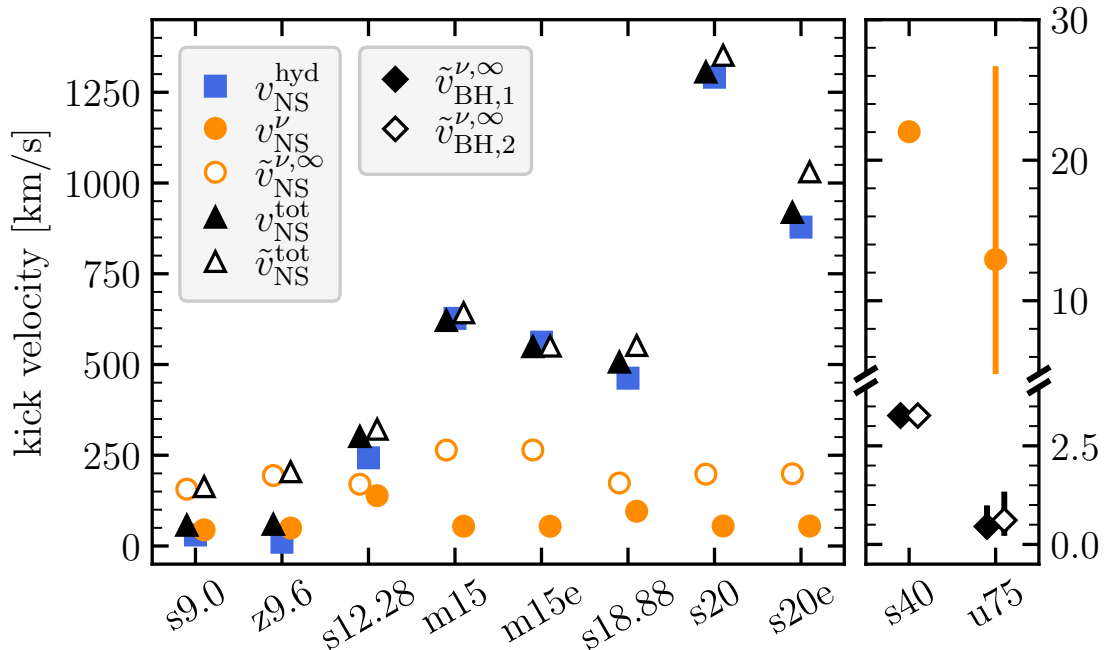


Fig. 4 Overview of the main results for NS kicks (*left panel*) and BH kicks (*right panel*). The filled orange circles mark the neutrino-induced kick velocities of the PNSs at times t_f^ν (see Tables 2 and 3), i.e., when the 3D simulations with VERTEX neutrino transport ended or when the PNS collapsed to a BH. *Left panel*: The blue squares denote the hydrodynamic NS kicks at later times $t_f \geq t_f^\nu$ (Table 2) when the 3D PROMETHEUS-VERTEX/NEMESIS simulations were stopped. The filled black triangles represent the total kick velocities, i.e., $|\mathbf{v}_{\text{NS}}^{\text{tot}}| = |\mathbf{v}_{\text{NS}}^{\text{hyd}}(t_f) + \mathbf{v}_{\text{NS}}^\nu(t_f^\nu)|$, at time t_f when the 3D SN simulations were stopped. Note that in some models the velocities still grow with significant rates at the end of our simulations (see Figure 3). The open orange circles are extrapolated values of the neutrino-induced kick velocities, assuming that the anisotropy of the neutrino emission until t_f^ν is representative for entire energy loss of the PNS in neutrinos (Equation 25). The open black triangles show extrapolated values of the total (neutrino plus hydrodynamic) kicks, $|\tilde{\mathbf{v}}_{\text{NS}}^{\text{tot}}| = |\mathbf{v}_{\text{NS}}^{\text{hyd}}(t_f) + \tilde{\mathbf{v}}_{\text{NS}}^{\nu,\infty}|$, i.e., assuming that the neutrino kick can be projected from t_f^ν into the future using its direction as given at t_f^ν and the neutrino-emission anisotropy given as averaged from bounce to t_f^ν . *Right panel*: The filled black diamonds in the right panel are the final BH kicks when the whole pre-collapse mass of the progenitor is swallowed by the BH, whereas the open back diamonds assume that only the He-core mass falls into the BH and the hydrogen envelope of the pre-collapse progenitor gets stripped. Note the different vertical scale of the right panel with a scale break at 4 km s^{-1} . The vertical bars in the case of model u75 indicate the stochastic variations of our different 3D collapse simulations of the $75 M_\odot$ progenitor (see Table 3). The plot shows that for SN explosions of low low-mass progenitors (here the 9.0 and $9.6 M_\odot$ models) neutrino-induced NS kicks are expected to dominate the hydrodynamic kicks, for intermediate-mass progenitors (here the $12.28 M_\odot$ model) both contributions to the NS kick are of similar magnitude, whereas for SN explosions of massive progenitors (here the 15 , 18.88 , and $20 M_\odot$ models) the hydrodynamic NS kicks are dominant. Note that in the $15 M_\odot$ simulations rapid rotation has an effect on the results (see text). In the case of BH formation without concomitant explosion and asymmetric mass ejection, the neutrino-induced BH kicks are only on the order of some km s^{-1} .

model s12.28 both neutrino and hydro kicks yield similarly important contributions to the total kick, and in the high-mass models m15, m15e, s18.88, s20, and s20e the hydrodynamic kicks account for the far dominant contributions to the total kicks. These results are in line with the findings reported by Stockinger et al (2020), Bollig et al (2021), and Burrows et al (2023b).

It is important to note that the hydrodynamic kicks in most models start growing initially more slowly than the neutrino kicks (see plots in Appendix A), and they rise rapidly only after

the SN shock has expanded to several thousand kilometers and the final ejecta asymmetry has developed. Before this time the rapid directional variability of the gas flows around the PNS does not permit the formation of a clear direction for the hydrodynamic kicks. The absolute values of the hydro kicks remain small during this early phase because they are reduced by the averaging of acceleration forces in different directions. The faster emergence of neutrino kicks of significant amplitudes and their complex interplay

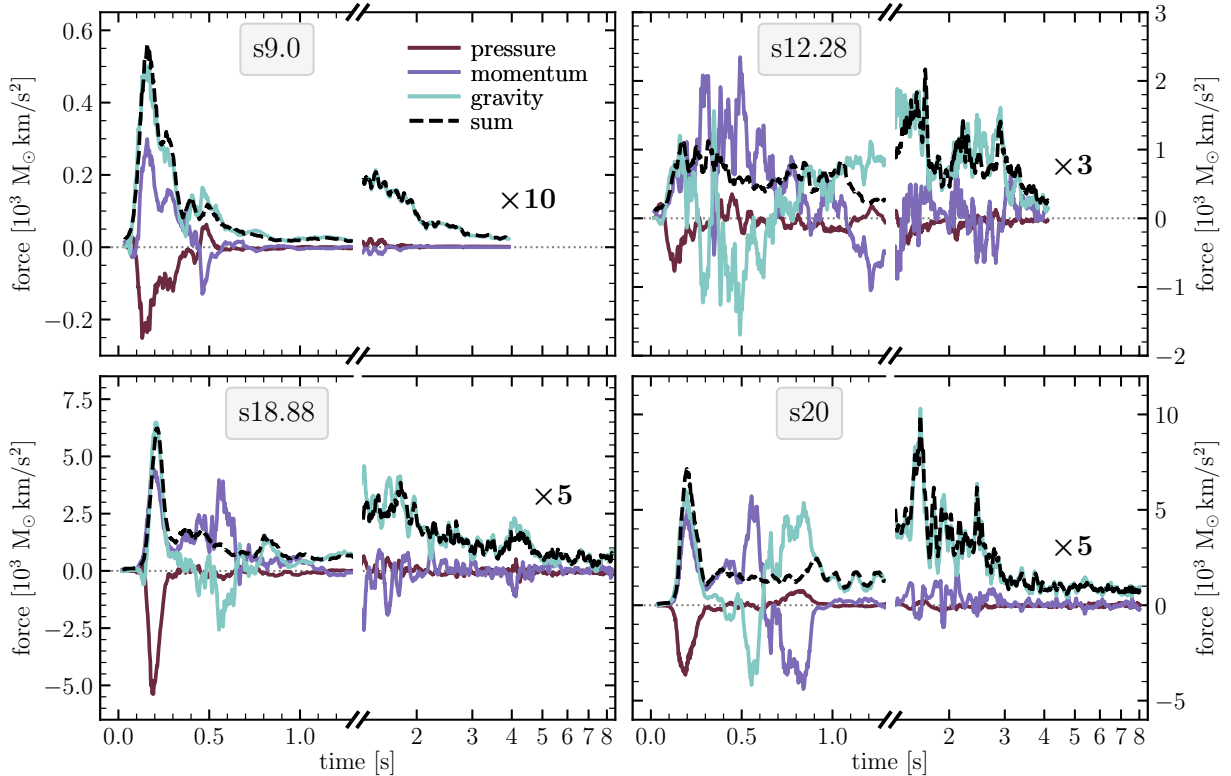


Fig. 5 Hydrodynamic forces on the PNS as functions of postbounce time for our 3D CCSN models s9.0 (*top left*), s12.28 (*top right*), s18.88 (*bottom left*), and s20 (*bottom right*). Colored solid lines as labelled in the upper left panel show the contributions to the total momentum transfer by gas pressure, momentum carried by mass gained or lost in accretion streams and outflows, and by the gravitational attraction between PNS and ejecta gas, as given in Equation (18) and evaluated with $R_0 = 2 R_{\text{NS}}$. The black dashed lines display the sum of these three components. In order to visualize the values that effectively create the PNS acceleration, we display the projections of the different forces onto the total accelerating force: $\hat{\mathbf{p}}_i \cdot \hat{\mathbf{p}}_{\text{hyd}} / |\hat{\mathbf{p}}_{\text{hyd}}|$ with $i \in \{\text{pres, mom, grav}\}$. Note the change of the time axis from linear to logarithmic for the evolution after 1.3 s. For better visibility the force values during this long-time evolution are scaled by the factors indicated in each panel. It is obvious that the gravitational force accounts for the dominant effect during most phases and is the far dominant contribution during the long-time evolution. Model s12.28 shows the largest fluctuations in all three force contributions until late times ($\gtrsim 1$ s) because of the ongoing, considerable mass accretion onto the PNS even during this late evolution (see middle panel of Figure 1)

with the hydro kicks will be discussed in detail in Section 3.2.

Despite the fact that the neutrino kicks, in particular the estimated final ones, can reach sizable magnitudes of up to $200\text{--}260 \text{ km s}^{-1}$ (Table 3), their relative shares in the absolute values of the total NS kicks of our high-mass models turn out to be more moderate (Figure 4). This finding is explained by the large angles θ_{hyd}^k between the directions of the hydro and neutrino kicks (see Table 3 for the values at time t_f' and Table 2 for those at t_f), especially in our rapidly rotating models m15 and m15e, where the relative angles are

around 100° at t_f . In all other models the directions of hydrodynamic and neutrino kick fall into the same hemisphere. In contrast, the spiral-SASI assisted explosion of the $15 M_\odot$ star does not only force both the hydro kick and the neutrino kick to directions nearly perpendicular to the spin axis of progenitor and NS, but it also leads to a very large angle between the two kick directions.

Finally, in Table 2 we also list the NS spin periods P_{NS} at t_f (evaluated as described in Appendix D of Stockinger et al, 2020, using $r_0 = R_{\text{NS}}$) and the angles $\theta_{\text{spin}}^{\text{kick}}$ between the NS spin and kick directions at this time. The PNSs are spun

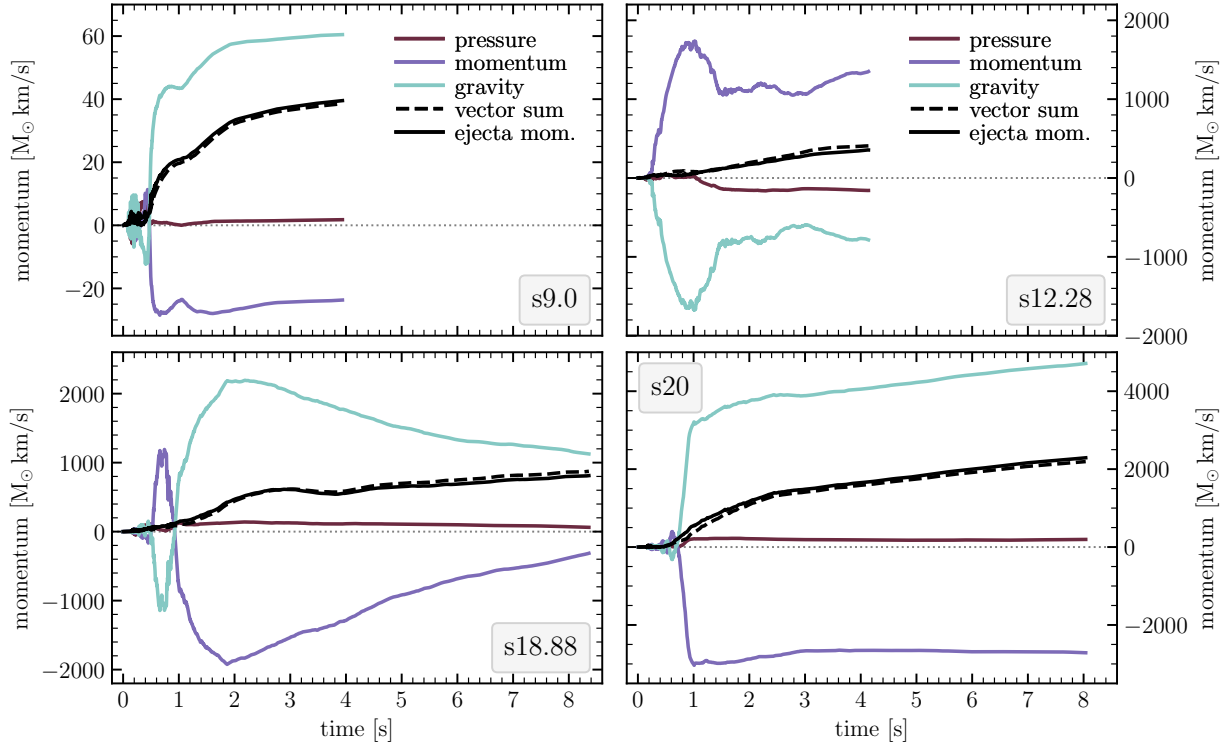


Fig. 6 Contributions to the total PNS momentum caused by hydrodynamic forces as functions of postbounce time for our 3D CCSN models s9.0 (*top left*), s12.28 (*top right*), s18.88 (*bottom left*), and s20 (*bottom right*). Colored solid lines as labelled in the upper panels show the projections $\mathbf{p}_i \cdot \mathbf{p}_{\text{hyd}} / |\mathbf{p}_{\text{hyd}}|$ for $i \in \{\text{pres, mom, grav}\}$, with $\mathbf{p}_i(t) = \int_0^t \dot{\mathbf{p}}_i dt'$ and $\mathbf{p}_{\text{hyd}}(t) = \mathbf{p}_{\text{pres}} + \mathbf{p}_{\text{mom}} + \mathbf{p}_{\text{grav}}$. This means that the force terms corresponding to gas pressure, momentum carried by mass flows, and gravity as given in Equation (18), evaluated with $R_0 = 2 R_{\text{NS}}$, are time-integrated until time t and projected onto the total momentum transfer to the PNS caused by all hydrodynamic forces until this time. The magnitude of this total hydrodynamic momentum transfer as the vector sum of the three components, $|\mathbf{p}_{\text{hyd}}|$, is plotted by black dashed lines. For comparison, the black solid lines give the total momentum of the gas exterior to the PNS, $|\mathbf{p}_{\text{gas}}|$, according to Equation (3). The agreement is very good in all displayed cases. The gravitational effect dominates also on the absolute momentum scale and not only with its component projected onto the total accelerating force acting on the PNS as shown in Figure 5. The concordance of the signs of total momentum and gravitational momentum transfer signals that the latter accounts for the decisive effect. Here, as in Figure 5, model s12.28 makes an exception due to ongoing, significant mass accretion even at late times $t > 1$ s; in this case momentum transfer to the PNS is still important and can govern the ongoing acceleration, which is visible by the momentum term dominating and pushing in the direction of the total PNS momentum. But we expect that the gravitational term will eventually take over once accretion onto the PNS has decreased to very low values as in the other models

up by the angular momentum carried to the compact remnant by anisotropic accretion flows (e.g., Blondin and Mezzacappa, 2007; Wongwathanarat et al, 2010; Rantsiou et al, 2011; Wongwathanarat et al, 2013; Kazeroni et al, 2016, 2017; Müller et al, 2017, 2018, 2019; Powell and Müller, 2020; Stockinger et al, 2020; Coleman and Burrows, 2022; Burrows et al, 2023b), but their values and directions are only transient and can be massively influenced by later fallback accretion (see the detailed discussions in Janka et al, 2022; Müller, 2023). In the $15 M_{\odot}$ models the NS spin period is

determined by the rapid rotation of the collapsing stellar core.

We witness no tendency of spin-kick alignment at t_f , in agreement with results discussed in Müller et al (2019) and the long-term 3D CCSN simulations reported by Janka et al (2022), but our sample of models is small. Spin-kick alignment is, in particular, also absent in the two rapidly spinning m15 models, because the directions of the NS kicks (hydro and neutrino contributions) are close to the equatorial plane due to the geometry of explosion, which is shaped by the spiral-SASI that

initiated the shock expansion. The situation might be different, however, in 3D explosions of rapidly rotating stars that explode either with a more axially symmetric, oblate deformation of the ejecta (Janka, 2017) or a prolate deformation along the rotation axis with a large hemispheric asymmetry (Burrows et al, 2023b).

A detailed discussion of the development of the NS spins in connection to the explosion behavior and 3D flow dynamics in our SN simulations will be provided in a separate paper (Kresse et al, in preparation).

In Figures 5 and 6 we show the forces that contribute to the acceleration of the PNS by asymmetric matter ejection and the corresponding integrated momentum transfer caused by hydrodynamic pressure, gas inflows and outflows, and the gravitational attraction of the gas surrounding the PNS. This analysis is based on the description in Section 2.3.3.

Of course, the NS’s hydrodynamic kick is a consequence of momentum conservation, since the NS receives a momentum of the same magnitude as the linear momentum of the asymmetric SN ejecta, but in the opposite direction. This fact is obvious from Equation (2), which we routinely use to compute the total hydrodynamic NS kick. Our analysis of Figures 5 and 6 is an alternative way to calculate the kick by adding up the forces acting at a certain radius R_0 (doing so, we follow previous analyses by, e.g., Scheck et al 2006; Nordhaus et al 2010; Wongwathanarat et al 2013; Müller et al 2017; Coleman and Burrows 2022; Burrows et al 2023b). In our study, this radius is chosen such that the agreement of the NS momentum vectors obtained by both methods is optimal, i.e., the negative of the ejecta momentum and the sum of the time integrals of the three contributing forces show best agreement (Figure 6). Thus we ensure that the evaluation radius R_0 for the force calculation (Equation 18) is properly chosen. We empirically determined the optimal radius to be $R_0 \approx 2R_{\text{NS}}$. This location is sufficiently far outside the PNS that the momentum transfer to the surrounding gas by neutrino interactions exterior to the neutrinospheres is accounted for already.

From Figures 5 and 6 it is clear that a major part of the NS acceleration takes place in most models after the gas accretion by the PNS has become unimportant, i.e., later than about 1s after bounce, but before fallback of initial ejecta

sets in many seconds later when the neutrino heating abates. The term for the gravitational force plays the dominant role on the long time scales, because gravity continuously acts as a long-range force, even after PNS accretion has diminished. This is obvious from the forces plotted in Figure 5. And Figure 6 also shows that during the late, post-accretion phase the final NS momentum is aligned with the direction of the integrated contribution by the gravitational effect (see the signs of the different components and that of the summed effect). Therefore Wongwathanarat et al (2013) introduced the name “gravitational tugboat mechanism” for the acceleration process, thus expressing the great importance of the gravitational term for the final NS kick. In contrast, as long as PNS accretion delivers significant amounts of matter onto the PNS (in model s12.28 this is the case during all of the displayed evolution), the momentum transfer by gas flows is the leading effect. But once the accretion subsides to an irrelevant level, any long-lasting NS acceleration will be governed by the gravitational interaction between the NS and the asymmetric ejecta, independent of the question whether some fraction of this gravitationally pulling matter ultimately falls back and is accreted by the NS or not.⁷ We expect that ultimately also in model s12.28 the gravitational tug adopts the leading role once ejecta downdrafts do no longer entail gas accretion by the PNS.

⁷In some recent papers (Coleman and Burrows, 2022; Burrows et al, 2023b) it was argued that the name “gravitational tugboat effect/mechanism” is inappropriately chosen and misleading, because the importance of gravity was misjudged when the simulations were halted before the final kicks were reached, and because the gravitational tug is in the wrong direction, and because some of the pulling matter may get accreted onto the NS in the end. Our analysis shows that the first two arguments are not valid. We further stress that even if some of the gravitationally pulling matter falls back onto the NS, this leads to a relative amplification of the ejecta momentum in the opposite hemisphere. Thus the NS momentum balancing this ejecta momentum also increases, i.e., there is a growth of the NS’s momentum component pointing to the side where the gravitationally attracting matter fell inward to the NS. The force mediating the NS acceleration is therefore gravity, even if some involved matter ultimately merges with the NS (due to gravitational interaction). These facts are the reason why the accelerating process was called gravitational tugboat mechanism/effect, although in the end the NS’s motion is, of course, just a consequence of global momentum conservation.

Table 3 Neutrino-induced PNS kicks and characteristic parameters at time t_f^ν for exploding and BH forming 3D models

Model	t_f^ν [s]	$M_{\text{NS,b}}$ [M_\odot]	$M_{\text{NS,g}}$ [M_\odot]	E_ν^{tot} [10^{53} erg]	$\bar{\alpha}_{\nu_e}$ [%]	$\bar{\alpha}_{\bar{\nu}_e}$ [%]	$\bar{\alpha}_{\nu_x}$ [%]	$\bar{\alpha}_\nu^{\text{tot}}$ [%]	v_{NS}^ν [km/s]	θ_{hyd}^ν [$^\circ$]	$\tilde{v}_{\text{NS}}^{\nu,\infty}$ [km/s]	$\tilde{v}_{\text{BH},1}^{\nu,\infty}$ [km/s]	$\tilde{v}_{\text{BH},2}^{\nu,\infty}$ [km/s]
s9.0	0.488	1.355	1.320	0.617	1.73	3.12	0.66	0.60	44.4	76.7	156.6	—	—
z9.6	0.450	1.350	1.319	0.556	2.06	3.81	0.84	0.76	49.4	9.8	194.2	—	—
s12.28	4.139	1.551	1.429	2.184	2.09	0.22	0.43	0.55	138.6	79.3	170.0	—	—
m15	0.457	1.575	1.533	0.744	0.11	0.25	1.10	0.70	54.4	48.9	264.3	—	—
s18.88	1.675	1.878	1.751	2.271	0.56	0.57	0.47	0.45	95.7	10.1	173.6	—	—
s20	0.506	1.901	1.828	1.310	0.82	1.53	0.57	0.46	55.0	60.3	197.8	—	—
s40	0.572	2.381	2.257	2.210	0.14	0.30	0.16	0.13	22.0	150.0	—	3.27	3.27
u75_DD2	0.519	2.889	2.743	2.616	0.21	0.39	0.18	0.15	26.7	118.6	—	0.99	1.34
u75_LS220_1	0.250	2.572	2.493	1.418	0.15	0.14	0.07	0.05	4.8	115.3	—	0.16	0.22
u75_LS220_2	0.248	2.573	2.494	1.397	0.13	0.23	0.12	0.13	11.6	102.1	—	0.39	0.53
u75_LS220_hr	0.254	2.563	2.484	1.425	0.14	0.31	0.12	0.12	11.4	87.2	—	0.38	0.52
u75_SFHo	0.325	2.623	2.529	1.696	0.36	0.25	0.20	0.09	10.2	113.7	—	0.35	0.47

Note: t_f^ν is the postbounce time at the end of the evolution simulated in 3D with full neutrino transport, which is identical with the moment when the PNS begins to collapse to a BH in the non-exploding models; $M_{\text{NS,b}}$, $M_{\text{NS,g}}$, and E_ν^{tot} are the baryonic PNS mass, the gravitational PNS mass, and the total radiated neutrino energy, respectively, at time t_f^ν ; $\bar{\alpha}_{\nu_e}$, $\bar{\alpha}_{\bar{\nu}_e}$, $\bar{\alpha}_{\nu_x}$, and $\bar{\alpha}_\nu^{\text{tot}}$ are the time-averaged anisotropy parameters of the energy emission in ν_e , $\bar{\nu}_e$, ν_x , and of the total (according to Equations 23 and 24) at t_f^ν ; $v_{\text{NS}}^\nu = |\mathbf{v}_{\text{NS}}^\nu|$ is the magnitude of the neutrino-induced PNS kick velocity at t_f^ν ; $\theta_{\text{hyd}}^\nu = \theta(\mathbf{v}_{\text{NS}}^{\text{hyd}}(t_f^\nu), \mathbf{v}_{\text{NS}}^\nu(t_f^\nu))$ is the angle between the hydro and the neutrino kick vectors at $t = t_f^\nu$; $\tilde{v}_{\text{NS}}^{\nu,\infty}$ is the estimated upper bound of the final, neutrino-induced kick velocity (for $t \rightarrow \infty$) according to Equation (25); $\tilde{v}_{\text{BH}}^{\nu,\infty} = v_{\text{NS}}^\nu \cdot M_{\text{NS,g}}/M_{\text{BH}}$ is the final BH kick velocity, assuming a final BH mass of $M_{\text{BH}} = M_{\text{prec}} - E_\nu^{\text{tot}}/c^2$ (i.e., the whole pre-collapse progenitor collapses into the BH) in the case of $\tilde{v}_{\text{BH},1}^{\nu,\infty}$ and $M_{\text{BH}} = M_{\text{He}} - E_\nu^{\text{tot}}/c^2$ (i.e., ejection of the entire hydrogen envelope instead of its accretion by the BH) in the case of $\tilde{v}_{\text{BH},2}^{\nu,\infty}$; the values of M_{prec} and M_{He} are given in Table 1.

3.2 Neutrino kicks

Anisotropic neutrino loss and the corresponding neutrino-induced NS kicks have two major sources. Either they originate from neutrino transport asymmetries inside the PNS (Figure 7), or they are a consequence of asymmetric neutrino emission and absorption/scattering asymmetries in regions outside the PNS but still close to its surface (Figure 8).

Convection in the hot mantle layer of the PNS below the neutrinospheres accelerates the transport of electron lepton number by carrying electrons and ν_e out of the dense PNS core (Figure 7). The corresponding convective cells with rising flows of lepton-rich gas and downdrafts of de-leptonized plasma create a patchy pattern with areas of enhanced neutrino emission distributed over the neutrinospheres. This pattern of hot-spot emission can lead to NS kicks. Since there is a large number of convective cells that change rapidly on time scales of only $\mathcal{O}(10\text{ ms})$, the hot-spot emission varies stochastically in random directions and with fluctuating amplitudes. Therefore the associated neutrino-induced kicks remain small because of statistical averaging effects. However, in addition to these small-scale and rapidly variable asymmetries, also a large hemispheric difference in the strength of PNS convection shows up in 3D simulations (Tamborra et al, 2014; O’Connor and Couch, 2018; Glas et al, 2019a; Powell and Müller, 2019; Vartanyan et al, 2019), which establishes a hemispheric contrast of the electron fraction in the near-surface layers of the PNS between its convection shell and the neutrinospheres. As a consequence, a dipolar asymmetry of the electron-neutrino lepton-number (ν_e minus $\bar{\nu}_e$) flux develops, which was termed Lepton-number Emission Self-sustained Asymmetry (LESA; Tamborra et al, 2014). This dipole can be the dominant multipole component defining the global asymmetry of the neutrino-lepton number emission of the PNS for longer-lasting (hundreds of milliseconds to seconds) periods of postbounce evolution, and its vector direction was found to be quite stable or to drift only slowly with time. The LESA phenomenon is also associated with dipolar anisotropies of the number and energy fluxes of all individual neutrino species (ν_e , $\bar{\nu}_e$, and heavy-lepton neutrinos ν_x) and therefore of the total neutrino luminosity, too. The vector direction of

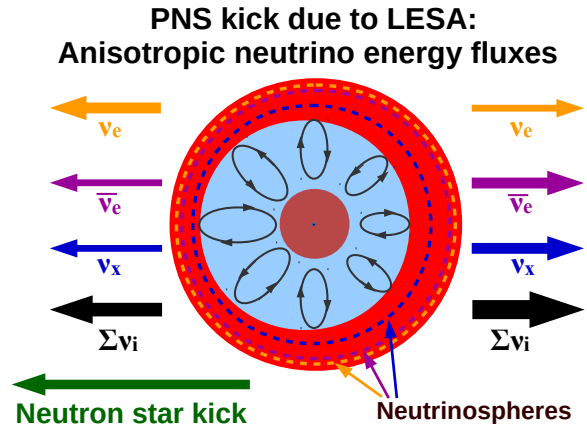
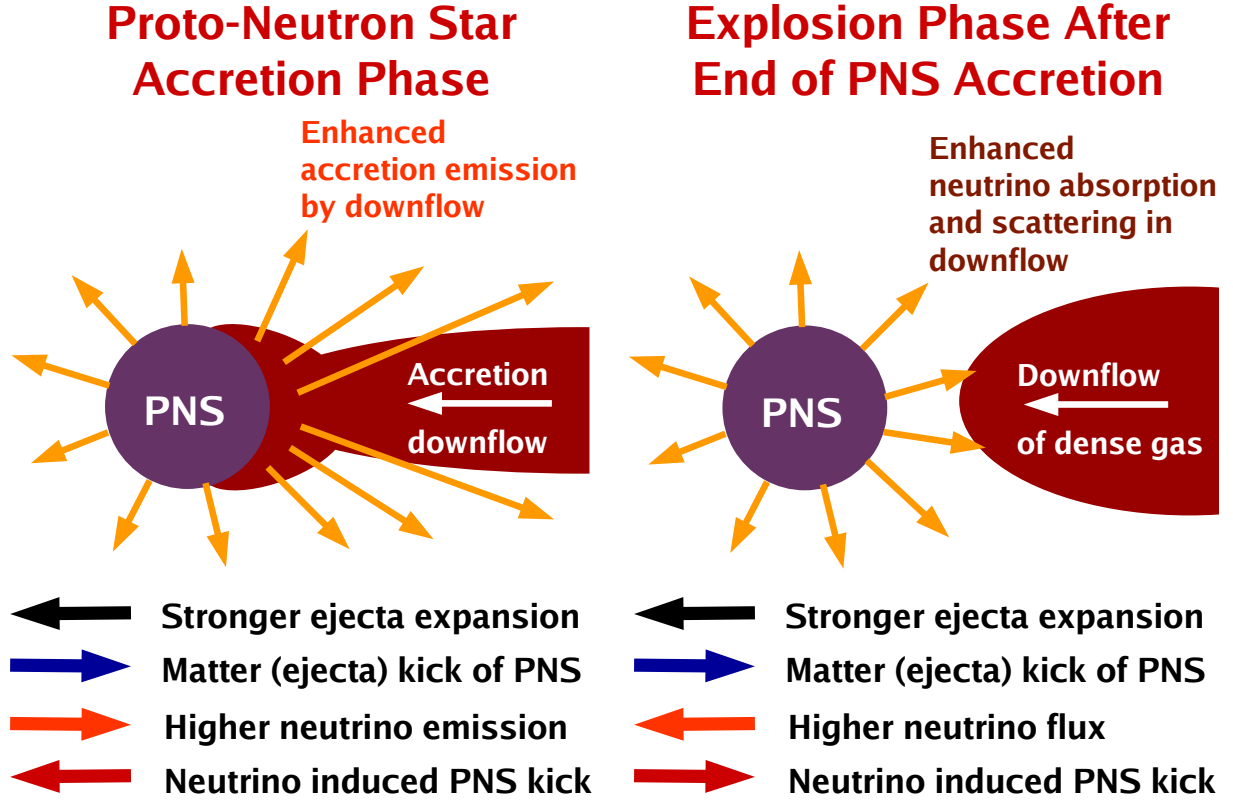


Fig. 7 PNS kick by anisotropic neutrino emission due to LESA. Stronger convective transport of electron-lepton number out of the PNS core in one hemisphere (in the image on the left side) increases the electron-neutrino (ν_e) emission, whereas the electron antineutrino ($\bar{\nu}_e$) and heavy-lepton neutrino (ν_x) fluxes are relatively stronger in the opposite hemisphere, where also the total neutrino flux as sum over all neutrino species is highest. Correspondingly, the PNS receives a total neutrino-induced kick (roughly) aligned with the orientation of the LESA dipole, which is defined by the direction of the strongest electron-neutrino lepton-number (ν_e minus $\bar{\nu}_e$) flux. The neutrino-induced kick by ν_e individually is directed opposite to the LESA vector and opposite to the kicks by $\bar{\nu}_e$ and ν_x individually

the dipole of the total neutrino luminosity is opposite to the dipole vector of the lepton-number flux. A schematic visualization can be seen in Figure 7, where the PNS receives a kick to the left, aligned with the LESA dipole vector and compensating the momentum carried away by the stronger total neutrino emission in the hemisphere on the right side.

The second region that contributes in sculpting anisotropic neutrino loss extends between the PNS and the SN shock (Figure 8). In this region dense downdrafts of cool gas and buoyant plumes of neutrino-heated, high-entropy matter cause asymmetric accretion onto the PNS and concomitant neutrino production as well as anisotropic absorption and scattering of neutrinos leaving the neutrinospheres. These non-spherical gas flows around the PNS are a consequence of convective overturn in the neutrino-heating layer behind the shock on the one hand, and of SASI mass motions as a global, nonradial instability of the stalled accretion shock on the other hand (e.g. Blondin et al, 2003; Ohnishi et al, 2006; Fogliizzo et al, 2007; Blondin and Mezzacappa, 2007; Scheck et al, 2008;



Neutrino flux asymmetry must be measured in free-streaming limit

Fig. 8 Interplay of neutrino-induced recoil acceleration and ejecta (matter) induced hydrodynamic recoil acceleration connected to asymmetric PNS accretion and ejecta distribution in exploding models. Typically, PNS accretion flows (*left*) and dense, slow ejecta in the vicinity of the PNS (*right*) preferentially occur in the hemisphere where the explosion and mass ejection are weaker, i.e., on the side the matter-induced PNS kick points to. *Left*: Gas accreted by the PNS can produce anisotropic neutrino emission before it settles down onto the PNS surface. The associated neutrino kick of the PNS, which is opposite to the direction of the enhanced neutrino emission, is thus towards the side of the stronger explosion and therefore opposite to the matter kick. *Right*: In the case of enhanced neutrino absorption and scattering by asymmetrically distributed dense ejecta near the PNS the neutrino kick and the matter kick are aligned. However, the momentum transfer by neutrino absorption and scattering in the dense ejecta reduces the net momentum of the anisotropically ejected gas in our considered situation, thus reducing the matter kick. This reduction of the hydrodynamic NS kick compensates the apparent neutrino kick that is associated with the neutrino flux anisotropy caused by the neutrino absorption and scattering in matter exterior to the neutrinosphere. Such a compensation is, for example, consistent with the fact that a PNS, whose neutrino fluxes leave the neutrinosphere isotropically in all directions in the PNS's rest frame, should not receive any net acceleration if a fraction of the neutrinos is absorbed or scattered at some distance away from the PNS in matter that is detached from the compact remnant. Note that alignment or anti-alignment of neutrino kicks and hydrodynamic kicks is meant here as a hemispheric coincidence rather than an exactly parallel orientation of the vectors

Iwakami et al, 2009; Fernández, 2010). The accretion downdrafts and rising outflows can be highly time dependent with variability of the mass accretion rate on time scales of milliseconds to tens of milliseconds, and their spatial pattern changes accordingly rapidly. However, a strong LESA dipole can have an impact on the gas motions around the PNS such that accretion downdrafts

occur, in a time-averaged sense, more frequently in the hemisphere the LESA dipole vector points to, because neutrino heating and thus the explosion is stronger in the opposite hemisphere (see Tamborra et al, 2014). This can lead to a near-alignment of the neutrino-induced NS kick produced by the LESA dipole and the hydrodynamic NS kick caused by the asymmetric explosion as

witnessed in the low-mass $9.6 M_{\odot}$ explosion model of [Stockinger et al \(2020\)](#), because in this model the LESA dipole determines the neutrino emission asymmetry as well as the ejecta asymmetry.

The general situation, however, is more complex when accretion flows develop randomly without any strong feedback with the LESA anisotropy that is created inside the PNS as visualized in [Figure 7](#). Downflows from random directions, as expected for conditions with a weak LESA dipole or massive accretion flows with strong penetration power in high-mass progenitors, can kick the PNS hydrodynamically to arbitrary directions and uncorrelated with the LESA asymmetry, but in a complex interplay with the neutrino emission and absorption occurring in the dense down-drafts. [Figure 8](#) provides a schematic and simplified graphical representation of how emission and absorption/scattering effects in the down-drafts in the close vicinity of the neutrino radiating PNS can correlate or anti-correlate with the hydrodynamic (matter-induced) kick. The directions of both kicks should not be considered here as perfectly aligned or anti-aligned, but as preferentially coincident in their hemispheres, because the neutrino emission by accretion downstreams can be spread over a wide angle and downflows can also be channelled around the PNS due to their associated angular momentum.

When strong and frequent downflows cause accretion emission of neutrinos dominantly on one side of the PNS, neutrinos will kick the PNS against the main direction of the hydrodynamic kick. This may sound counter-intuitive, but it can be understood by the fact that the ejecta-induced kick usually points towards the hemisphere with the higher downflow activity, because the explosion is stronger and thus the momentum of the outward ejecta expansion is higher in the opposite hemisphere. In contrast, when downflows do not reach as close to the PNS surface and are not accreted by the PNS, they mostly absorb and scatter neutrinos from the PNS instead of producing accretion emission. The absorbed neutrinos will transfer momentum to the downflows, thus increasing the gas momentum on this side of the PNS. Consequently, the hydrodynamic kick of the PNS associated with asymmetric gas ejection will be reduced, because this kick is directed towards the downflows and therefore it is collinear with the

extra gas momentum caused by neutrino absorption and scattering. The reduction of the effective hydrodynamic kick, however, is compensated by a neutrino kick aligned with the hydrodynamic kick, since the neutrino absorption and scattering in the downflows lead to a relative enhancement of the neutrino radiation in the opposite hemisphere. A proper balancing of these counter-working effects of hydrodynamic and neutrino kicks requires the measurement of the momentum asymmetry of the escaping neutrinos in the free-streaming regime at large distances on the one hand and the integration of the entire ejecta momentum on the other hand, as already discussed in [Sect. 2.3](#).

One can verify these elementary facts on the basis of our detailed analysis of the neutrino kicks for NSs and BHs in our set of 3D simulations.

3.2.1 Neutrino kicks of neutron stars

[Table 3](#) provides an overview of our results for the neutrino-induced PNS kicks in all of our 3D simulations at time t_f'' until which the VERTEX neutrino transport was applied, and [Figure 9](#) displays the time evolution of characteristic quantities. The neutrino kicks start rising within ~ 100 ms after bounce and typically reach higher values more quickly than the hydrodynamic kicks (see [Figures A1–A6](#)). The former grow as soon as neutrino emission asymmetries develop inside the PNS or in its near-surface accretion layer, whereas the hydrodynamic kicks find a stable direction only after the explosion has set in and then reach higher values in a long-time trend of continuous growth in explosions with pronounced ejecta asymmetries ([Figure 3](#)).

The magnitudes of the neutrino kicks reached within about 0.5 s after bounce are on the order of 50 km s^{-1} . While the instantaneous neutrino emission asymmetry parameters $\alpha_{\nu}^{\text{tot}}$ fluctuate around a few percent (typically between roughly $\sim 1\%$ and $\sim 3\%$), their time-averaged values are considerably lower (around $\sim 0.5\text{--}0.8\%$; [Table 3](#)) because of the rapid, short-time changes of the directions of the emission asymmetries ([Figure 9](#)). It is remarkable that in our lower-mass models s9.0 and z9.6, the time-averaged asymmetry parameters of ν_e and $\bar{\nu}_e$ and in model s12.28 that of ν_e stick out by significantly higher values of 2–4%. This fact is connected to the main origin of the neutrino emission anisotropy from

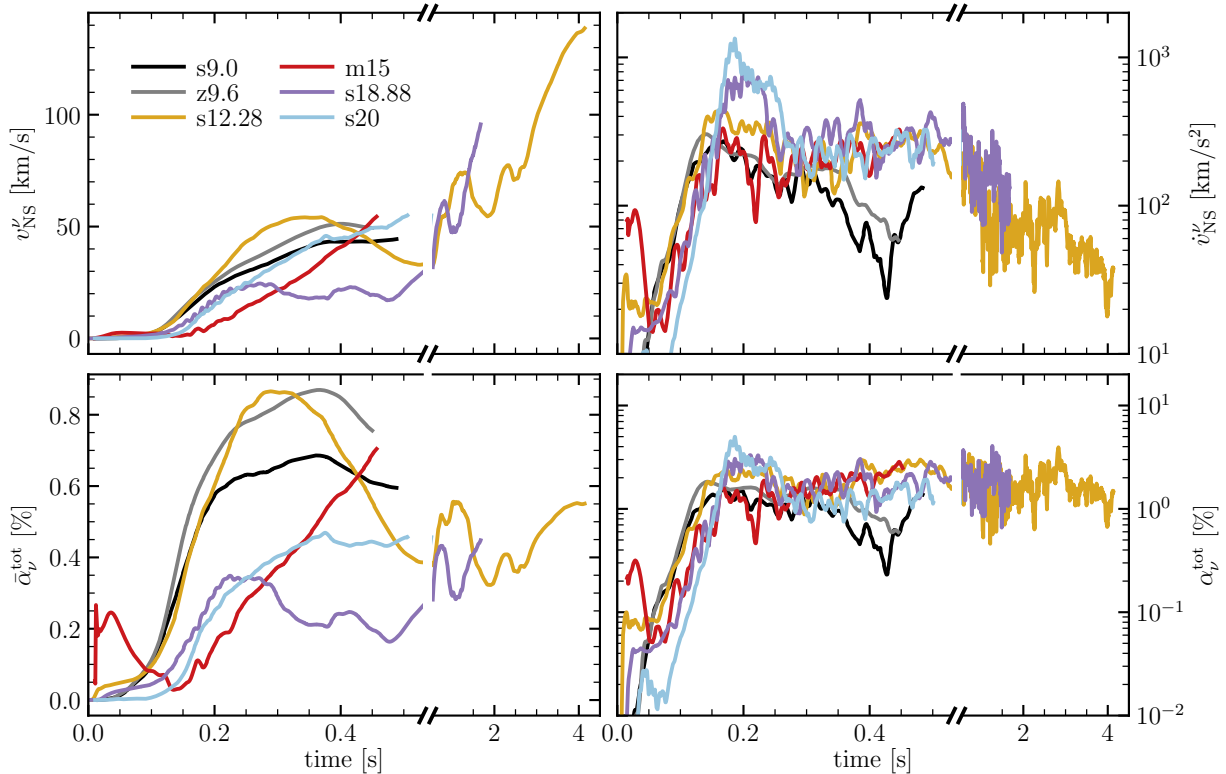


Fig. 9 Neutrino-induced PNS kick velocity (*top left*), the corresponding PNS acceleration by anisotropic neutrino emission (*top right*), the time-integrated anisotropy parameter of the total neutrino emission (Equation 24; *bottom left*), and the corresponding instantaneous neutrino anisotropy parameter (Equation 22; *bottom right*) for all successfully exploding models

a LESA dipole in these models. We will come back to this issue below. From Figure 9 we can also conclude that the time-averaged neutrino emission asymmetry asymptotes to fairly stable values between about 0.3% and 0.5% after several seconds, despite continuous large-amplitude variations of the instantaneous values (see our models s12.28 and s18.88 with long-term neutrino transport). This persistent low-level emission asymmetry leads to a long-lasting neutrino-induced acceleration of the PNS (Figure 9, upper right panel), which decreases with time as the neutrino luminosities of the cooling PNS gradually decline. These findings justify the assumptions that we made in our extrapolation formula for the neutrino kicks in Equation (25).

Inspecting Figures 10, 11, and 12, as well as the supplementary plots given in Appendix A and B, we can verify the different kinds of neutrino-induced kicks discussed before and visualized graphically in Figures 7 and 8.

Model z9.6:

Model z9.6 is the explosion of a low-mass progenitor with a particularly steep density gradient outside of its iron core, for which reason its bounce shock expands continuously and very rapidly. Therefore the explosion is nearly spherical (see the value of $\bar{\alpha}_{\text{ej}}$ in Table 2), and long-lasting accretion downflows towards the PNS do not occur (Melson et al, 2015b; Stockinger et al, 2020). Accordingly, the hydrodynamic NS kick remains very small (Figures 3 and 4) and the neutrino kick is dominated by the LESA asymmetry of the neutrino emission.

The lower left panel of Figure 10 shows the trend of aligned hydro and neutrino kicks that is expected when the LESA dipole asymmetry of the neutrino emission determines also the explosion asymmetry. The mass ejection will then be most powerful in the direction of the highest summed luminosity of ν_e and $\bar{\nu}_e$, because these

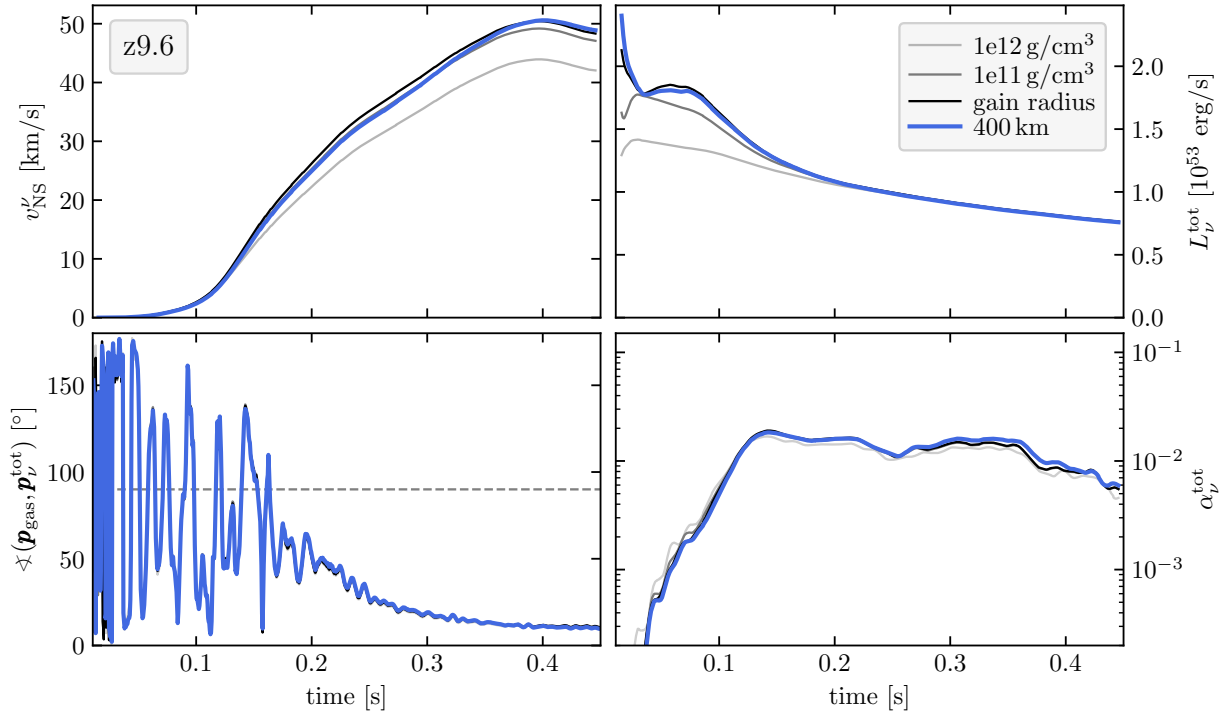


Fig. 10 Neutrino-induced NS kick velocity (*top left*), total neutrino luminosity (*top right*), angle between vector directions of the linear gas momentum and the linear momentum of the neutrino emission (*bottom left*), and instantaneous neutrino anisotropy parameter (Equation 22; *bottom right*) as functions of time for model z9.6. The thick blue lines show the results for our standard evaluation at a fixed radius of 400 km (i.e., in the free-streaming regime of the neutrinos). The light grey, dark grey, and black thin lines indicate the corresponding results for evaluation at the (angle-averaged) densities of $10^{12} \text{ g cm}^{-3}$ and $10^{11} \text{ g cm}^{-3}$, and at the (angle-averaged) gain radius, respectively. Model z9.6 exhibits the typical properties of a LESA-dominated neutrino kick, for example aligned neutrino and hydrodynamic kicks, because the low-mass progenitor explodes quickly and long-existent, massive accretion downflows around the PNS are absent. The analysis of the NS kick at all chosen locations yields similar results

two neutrino species dominate the postshock heating by their absorption on free nucleons. The neutrino-driven explosion is therefore strongest in the direction opposite to the LESA vector (i.e., opposite to the dipole vector of the ν_e minus $\bar{\nu}_e$ number flux) and therefore opposite to both hydro and neutrino kicks (see also Stockinger et al, 2020).

In the bottom right panel of Figure A2 we witness the expected, LESA-typical alignment of the PNS kicks caused by $\bar{\nu}_e$ and ν_x emission asymmetries, which are anti-aligned with the ν_e -induced NS kick, because the direction of the ν_e -luminosity dipole vector is opposite to those of the $\bar{\nu}_e$ and ν_x luminosity dipoles (Figure 7). The panel also shows that the hydrodynamic acceleration of the NS (represented by $\dot{\mathbf{p}}_{\text{gas}}$) fluctuates mostly in directions perpendicular to the acceleration vector of the total neutrino kick (represented by $\dot{\mathbf{p}}_{\nu}^{\text{tot}}$),

because of considerable stochastic variations of the directions of the accelerating hydrodynamic forces (weakened in Figure A2 because the curves are smoothed by applying a running average). For random relative directions of hydro and neutrino accelerations, the angles between both would be symmetrically distributed around a maximum at 90° . However, because of the LESA influence on the explosion asymmetry there is a statistical preference to angles of less than 90° , in particular between ~ 150 ms and ~ 400 ms, so that the net effect leads to aligned directions of the (time-integrated) hydro and neutrino kicks (Figure 10 and third panel from top in the right column of Figure A2).

Model s9.0:

Some of the phenomena found in model z9.6 can similarly be noticed in model s9.0 (Figure A1),

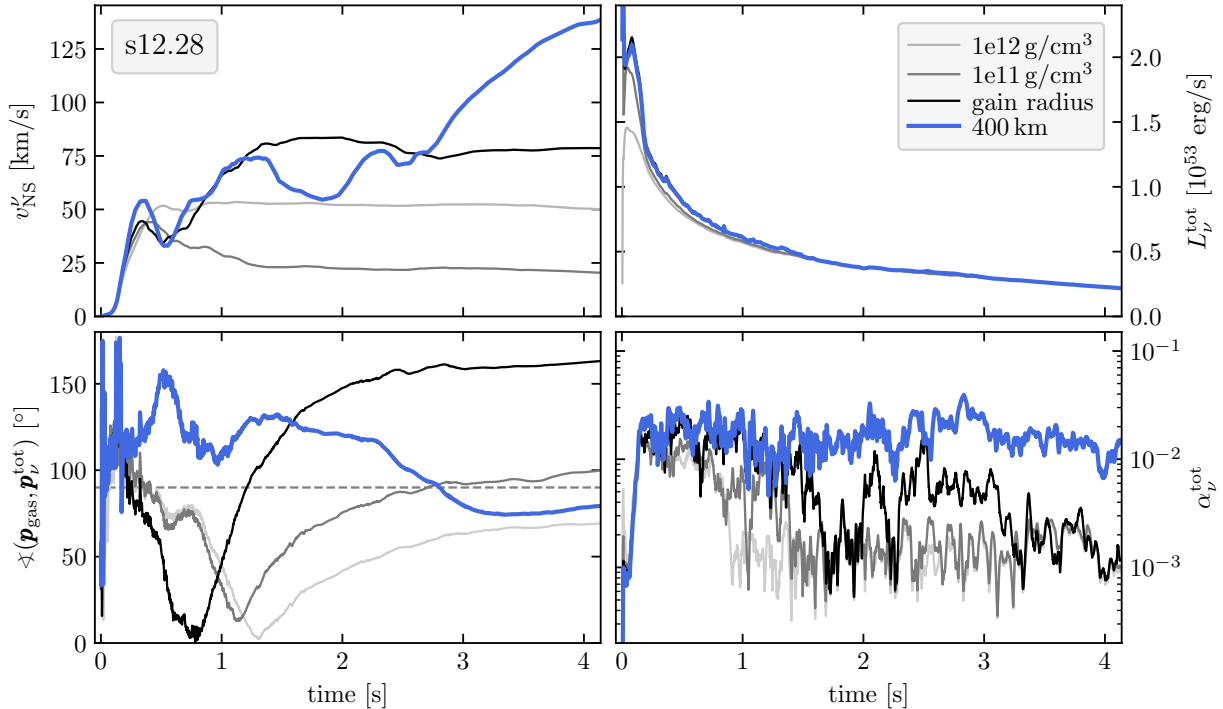


Fig. 11 Same as Figure 10, but for model s12.28. The model is an intermediate case that shows characteristic features of neutrino-induced NS kicks due to the LESA asymmetry in the first ~ 0.5 s after bounce, due to asymmetric accretion emission between ~ 0.5 s and ~ 1.5 s, and due to neutrino absorption and scattering in anisotropic downflows at later times. The results at $t \gtrsim 0.5$ s after bounce depend strongly on the chosen location of the kick analysis

which also has a small hydrodynamic NS kick, mainly because of its low explosion energy and despite a bigger ejecta asymmetry $\bar{\alpha}_{\text{ej}}$ than in model z9.6 (see Table 2 and Equation 32 for the scaling relations). Although model s9.0 exhibits the described characteristic features of a LESA-dominated neutrino kick most of the time, e.g., aligned acceleration directions by $\bar{\nu}_e$ and ν_x emission dipoles, anti-aligned to the ν_e -induced kick, there are times when the clear LESA situation in this model is perturbed by accretion downflows. This happens, for example, between ~ 350 ms and ~ 450 ms after bounce, when massive downflows mainly in the hemisphere opposite to the LESA vector absorb and scatter neutrinos (accretion emission of ν_e and $\bar{\nu}_e$ is only a secondary effect). This has several consequences, all of which are visible in Figure A1. First, the NS’s hydro kick, which in model s9.0 is not determined by LESA and has a large angle relative to the LESA direction (Stockinger et al, 2020), begins to grow during this phase shortly after the onset of the explosion (top and second panels in right column);

second, the angle between neutrino-induced and hydrodynamic kick velocities finds a stable, slowly evolving direction (third panel from top in right column); and third, the angle between ν_e -induced PNS acceleration (in the anti-LESA direction) and $\bar{\nu}_e$ and ν_x -induced accelerations shrinks due to the neutrino interactions in the downflows (bottom right panel). However, the direction of the neutrino kick is quite stable and largely unaffected by the downflows. Overall, in model s9.0, in contrast to the situation in model z9.6, the final kick geometry is not affected by the LESA emission dipole. This means that the hydrodynamic kick and the LESA-dominated neutrino kick are basically uncorrelated, implying that the relative angle between hydro kick and neutrino kick at time t_f^{ν} is large, nearly 80° (Table 3).

Interestingly, in model s9.0 as well as in model z9.6 the time-averaged and instantaneous asymmetry parameters of each neutrino species, $\bar{\alpha}_{\nu_i}$ and α_{ν_i} , approach each other towards the end of our VERTEX transport calculations. The underlying reason is that in these two simulations the

postbounce phases of high mass accretion rates by the PNS last only for ~ 140 ms (in s9.6) and for ~ 320 ms (in s9.0) (upper left panels of Figures A1 and A2), although in model s9.0 occasional downflows at later times can still cause perturbations of the general trends. The values of $\bar{\alpha}_{\nu_e}$ and $\bar{\alpha}_{\bar{\nu}_e}$ are particularly large in these simulations where the LESA dipole dominates the neutrino emission anisotropy, namely several percent instead of typically less than about 1% (see Table 3).

Model s12.28:

In model s12.28 neutrino and hydrodynamic NS kicks are of comparable magnitudes (Figure 4) with a big angle of around 80° between the two vector directions at late times (similar to model s9.0; Tables 2 and 3). This model is an intermediate case where LESA as well as long-lasting downflows and accretion around the PNS play similarly important roles for the neutrino kicks. Accretion occurs at a considerable strength for roughly the first 1.5 s after bounce and on a lower level even later. The corresponding neutrino emission is visible by enhanced ν_e and $\bar{\nu}_e$ luminosities that show variations over time (Figure A3). It can also be concluded from Figure 11, which demonstrates the important influence of emission and absorption/scattering of neutrinos exterior to the neutrinospheres by the fact that the evaluation of the neutrino-induced kick yields drastically different results for magnitude and direction, depending on whether the analysis is performed around and interior to the neutrinospheres (i.e., at densities of $10^{11} \text{ g cm}^{-3}$ and $10^{12} \text{ g cm}^{-3}$), or at the gain radius, or in the free-streaming regime at 400 km. Moreover, since the final angle between hydro and neutrino kicks is large, the ejecta geometry does not seem to be strongly influenced by the LESA asymmetry of the neutrino emission of the PNS in this model.

These aspects manifest themselves in a variety of specific properties of the total neutrino kick in Figures 11 and A3. During the first ~ 0.5 s after bounce, the LESA asymmetry of the PNS's neutrino emission mainly determines the neutrino kick, because the analysis for v_{NS}^ν , α_ν^{tot} , and the angle between hydro kick and neutrino kick yields very similar results at all of the different locations chosen in Figure 11. In the following period from 0.5 s until ~ 1.5 s after bounce, the total neutrino kick is accretion-emission dominated and

thus anti-aligned to the hydro kick, signalled by a large angle relative to the latter, as expected from the left panel of Figure 8. This is consistent with the fact that the neutrino kick evaluated at the gain radius differs from the kicks obtained at $10^{11} \text{ g cm}^{-3}$ and $10^{12} \text{ g cm}^{-3}$ but shows good agreement with the result obtained in the free-streaming limit during this period (Figure 11). At later times, the angle between hydro and neutrino kicks shrinks, suggesting that the neutrino kick is now strongly influenced by neutrino scattering and absorption in downflows that do not reach the PNS surface (as sketched in Figure 8, right panel). This picture is confirmed by the fact that the neutrino kick evaluated at 400 km significantly differs from the result obtained at the gain radius (Figure 11).

Further support of this picture is provided by an evaluation of the neutrino kicks of the different neutrino species individually in Figures B7, B8, and B9. In the first ~ 0.5 s after bounce one can witness location-independent kick results as well as the LESA-characteristic opposing directions of the ν_e kick on the one hand and the $\bar{\nu}_e$ and ν_x kicks on the other hand, which thus compensate each other partially. This is visible from the angles between \mathbf{p}_{ν_i} and \mathbf{p}_{gas} and from the direction angles (ϑ, φ) of the different neutrino kicks in a global polar coordinate system of the 3D simulation. During the earliest phase, $t \lesssim 0.2$ s after bounce, one can also notice a LESA-atypical tendency that the (still small) linear gas momentum is aligned with the ν_e momentum vector and anti-aligned with the $\bar{\nu}_e$ and ν_x momentum vectors, which confirms the previous statement that the LESA neutrino emission asymmetry of the PNS has no strong influence on the gas flows between PNS and SN shock. At $t \gtrsim 0.2$ s the gas momentum direction moves to the hemisphere opposite to the ν_e momentum vector (relative angle around 100°), before at $t \gtrsim 0.4$ s massive accretion downflows develop in the $-z$ hemisphere. This leads to a migration of the vector direction of the gas momentum, \mathbf{p}_{gas} , towards the $+z$ axis ($\vartheta \rightarrow 0$) of the global coordinate system and thus, incidentally more LESA-compatible, it is now directed nearly against the ν_e dipole (see Tamborra et al, 2014). Since the corresponding ν_e momentum vector of the LESA emission points towards the south ($\vartheta \approx 150^\circ$), the additional ν_e emission by accretion in the same hemisphere strengthens the

ν_e -induced NS kick until about 1.5 s (visible by the large difference between the kicks evaluated at $10^{11} \text{ g cm}^{-3}$ and $10^{12} \text{ g cm}^{-3}$ on the one hand and at the gain radius and in the free streaming regime on the other hand (Figure B7).

Since the momentum direction of the ν_e emission remains nearly stable during all of this evolution and at any of the chosen locations for evaluation in Figure B7, the time-averaged asymmetry parameter $\bar{\alpha}_{\nu_e}$ is close to the magnitude of the fluctuating values of α_{ν_e} , similar to our findings for $\bar{\alpha}_{\nu_e}$ and $\bar{\alpha}_{\bar{\nu}_e}$ in the LESA dominated models z9.6 and s9.0. At times $t \gtrsim 1.5 \text{ s}$, accretion emission becomes negligibly small and the ν_e -induced NS kick remains nearly constant. Since the gas momentum direction drifts, there is a continuous, slow change of the angle between \mathbf{p}_{ν_e} and \mathbf{p}_{gas} .

The massive accretion downflows that develop in the $-z$ hemisphere between $\sim 0.4 \text{ s}$ and $\sim 1.5 \text{ s}$ after bounce reduce the $\bar{\nu}_e$ -induced NS kick, in contrast to their effect on the ν_e -induced kick. Since the LESA dipole direction of the $\bar{\nu}_e$ emission is opposite to the one of ν_e , the additional accretion emission of $\bar{\nu}_e$ points against the $\bar{\nu}_e$ LESA dipole and thus leads to a decrease of the NS kick due to the anisotropically radiated $\bar{\nu}_e$ not only as a function of time, but also when the kick magnitudes are evaluated at locations outside the PNS rather than in the neutrinospheric region (see Figure B8). Moreover, the accretion emission of $\bar{\nu}_e$ in the hemisphere opposite to the $\bar{\nu}_e$ LESA vector causes a considerable migration of the $\mathbf{p}_{\bar{\nu}_e}$ vector when computed at locations exterior to the PNS.

For the NS kick by the ν_x emission similar effects as for $\bar{\nu}_e$ can be observed (Figure B9). But here the accretion in the southern hemisphere between $\sim 0.4 \text{ s}$ and $\sim 1.5 \text{ s}$ tends to suppress the ν_x diffusion out of the PNS on this side. It therefore enhances the ν_x LESA dipole pointing northward and thus the ν_x -induced kick evaluated at the gain radius. This effect, however, is nearly compensated by asymmetric ν_x scattering in the gain layer at larger distances, for which reason the NS kick at 400 km increases only little until $\sim 1.5 \text{ s}$. Only at later times new downdrafts (at new directions, as indicated by the shift of \mathbf{p}_{gas}) cause considerable ν_x scattering between the gain radius and 400 km (but hardly affect the ν_e and $\bar{\nu}_e$ emission). After $\sim 2.4 \text{ s}$ this increases the ν_x -induced NS kick

by nearly a factor of two, connected with a considerable change of the ν_x momentum direction (Figure B9, bottom left panel). An effect of the same kind can be witnessed for $\bar{\nu}_e$ at $t \gtrsim 3 \text{ s}$ and at a radius of 400 km (Figure B8). The drifting momentum directions of the radiated $\bar{\nu}_e$ and ν_x in the free streaming limit lead to time-averaged values of their $\bar{\alpha}_{\nu_i}$ that are considerably lower than the (fluctuating) magnitudes of the α_{ν_i} because of the compensating effects of acceleration phases in different directions (Figure A3). Only the analysis of $\bar{\alpha}_{\bar{\nu}_e}$ and $\bar{\alpha}_{\nu_x}$ at densities of $10^{11} \text{ g cm}^{-3}$ and $10^{12} \text{ g cm}^{-3}$ reveals directional stability, because at these radii the LESA dipole determines the $\bar{\nu}_e$ and ν_x emission asymmetries (Figures B8 and B9).

Model m15:

Model m15 explodes by the neutrino-powered mechanism, because the rapid rotation of the $15 M_{\odot}$ star favors the development of a strong spiral-SASI mode that supports the shock expansion preferentially around the equatorial plane. The shock front possesses a pronounced oblate shape with a sizable dipolar deformation along the equator and accretion downstreams at the poles (Summa et al, 2018). Due to the rapid rotation of the progenitor, the NS spin vector basically coincides with the progenitor's rotation axis and the final spin period of the NS is estimated to be about 2 ms at the end of our hydrodynamic simulations at t_f (Table 2). Here, angular momentum acquired by accretion flows and lost by mass outflow is taken into account according to the evaluation described in Appendix D of Stockinger et al (2020), but angular momentum carried away by neutrino emission is not included (such an angular momentum drain through neutrinos might increase the final NS spin period by several 10%; Janka, 2004).

The vector directions of the hydrodynamic kick and of the neutrino kick in model m15 are close to the equatorial plane (see Section 3.1), and both have a large angle relative to each other, namely about 50° at t_f^ν (Table 3 and Figure A4) and around 100° at t_f (Table 2). The neutrino kick in this model dominates clearly until the VERTEX neutrino transport calculation was stopped at t_f^ν , because the hydrodynamic kick velocity exhibits large-amplitude and quasi-periodic directional changes until it finds a stable direction

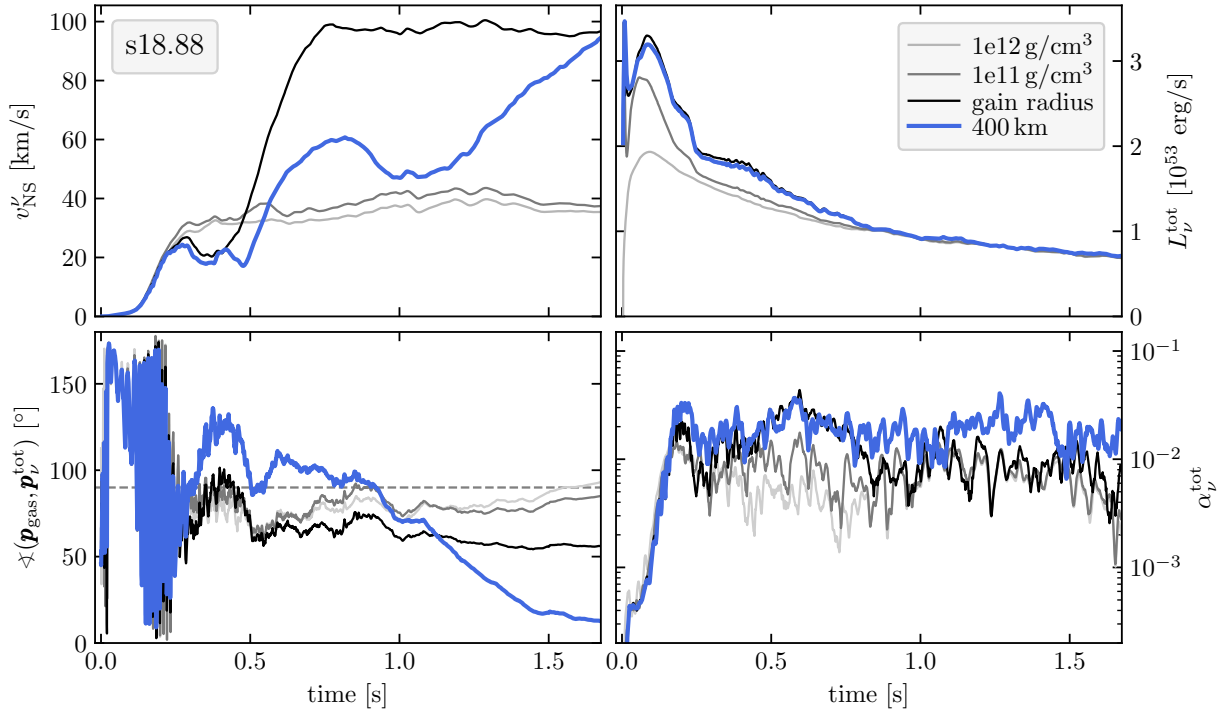


Fig. 12 Same as Figure 10, but for model s18.88. In this case the neutrino-induced NS kick is determined by the neutrino flux asymmetry caused by the LESA dipole before ~ 0.25 s after bounce, then it is mainly connected to ν_e and $\bar{\nu}_e$ emission and ν_x scattering in anisotropic accretion flows onto the PNS until ~ 0.75 s, and at later times by neutrino absorption and scattering in asymmetric downflows that do not reach the PNS but interact with neutrinos exterior to the gain radius. This can be concluded from the times when the kick velocities evaluated at different locations start to separate from each other or level off at nearly constant values

only about 150 ms after the onset of the explosion (Figure A4, third panel from top in the right column).

Since LESA is suppressed in the rapidly rotating PNS (see Walk et al, 2019), the NS acceleration (momentum derivative) vectors of ν_e and $\bar{\nu}_e$ are relatively close to each other (Figure A4, bottom right panel). This is expected for an accretion-dominated flux asymmetry, and the importance of accretion emission also explains why the neutrino kick vector stays close to the equatorial plane, because accretion flows from all directions carry large angular momentum, which forces them onto wound trajectories around the PNS’s equator. The momentum vector of the ν_x emission shows only a loose correlation with those of ν_e and $\bar{\nu}_e$, because ν_x mainly originate from the interior of the PNS. Scattering of ν_x in the accretion flows plays a secondary, but non-negligible role, driving the ν_x momentum vector also close to the equatorial plane, for which reason the total neutrino

kick of the NS is nearly perpendicular to the progenitor’s spin axis. Rapid directional variations of the accretion flows lead to a large reduction (by a factor of 10–20) of the time-averaged emission asymmetry parameters $\bar{\alpha}_{\nu_e}$ and $\bar{\alpha}_{\bar{\nu}_e}$ compared to the instantaneous values of α_{ν_e} and $\alpha_{\bar{\nu}_e}$, whereas the reduction is far less extreme (a factor of 2–3 near the end of the VERTEX transport calculation) for the more stable ν_x emission.

Models s18.88 and s20:

These two explosion simulations of massive progenitors resemble each other fairly closely in their overall behavior, but model s18.88 was computed with VERTEX neutrino transport more than three times longer. Both models are cases where accretion downflows to the PNS clearly determine the neutrino emission asymmetry and the final neutrino-induced kick. Again, the neutrino kick velocities grow initially faster than the hydrodynamic kick velocities, because the latter exhibit

rapid, large-amplitude variations of their directions relative to the neutrino kick, which are essentially symmetrically distributed around a relative angle of 90° as expected for randomly varying orientations. When ultimately the explosions take off and develop clear and more stable global asphericities, also the hydrodynamic kick velocities begin to rise (Figures A5 and A6). In the end the hydrodynamic kicks clearly dominate the total NS kicks in these two models (Tables 2 and 3; Figures 3 and 4).

When the LESA dipole in the PNS becomes sizable after ~ 0.1 s of postbounce evolution, the LESA emission asymmetry determines the neutrino kick of the PNS, which therefore starts to rise steeply at about this time. The LESA effect is crucial during the first ~ 0.25 s after bounce, signalled by the almost perfect agreement of the kick velocities evaluated at all of the different locations in Figure 12, indicating that the neutrino kick is defined by anisotropic neutrino transport inside the PNS. Moreover, a detailed inspection shows (the plots are not included in this paper) that the momentum vectors of the radiated ν_e and $\bar{\nu}_e$, \mathbf{p}_{ν_e} and $\mathbf{p}_{\bar{\nu}_e}$, are oriented in nearly opposite directions, and \mathbf{p}_{ν_e} and $\mathbf{p}_{\bar{\nu}_e}$ are nearly collinear during this phase, fully consistent with the LESA emission geometry. For more details on the LESA in model s18.88, the reader is referred to the analysis presented in Appendix C of Bollig et al (2021).

At ~ 0.25 s the kick velocities computed at the gain radius and in the free-streaming regime at 400 km begin to deviate considerably from those obtained at densities of $10^{11} \text{ g cm}^{-3}$ and $10^{12} \text{ g cm}^{-3}$. At that time emission of ν_e and $\bar{\nu}_e$ from accretion downflows becomes important, mostly taking place in the hemisphere the LESA lepton-number dipole vector points to (as expected if LESA would affect the accretion flows around the PNS; Tamborra et al, 2014). This accretion emission strengthens the ν_e flux in this hemisphere and thus increases the ν_e -induced NS kick compared to the LESA-determined kick, whereas it reduces the $\bar{\nu}_e$ -induced NS kick, because the $\bar{\nu}_e$ LESA dipole vector is in the opposite direction. Since enhanced scattering in the accretion layer damps the ν_x diffusion out of the PNS on the weaker side of the LESA lepton-number dipole, the ν_x emission asymmetry and corresponding NS kick are also amplified when measured at the gain radius.

This enhancement, however, is compensated to a large degree by ν_x scattering exterior to the gain radius so that, effectively, the net NS kick by the ν_x flux is not much altered (only slightly reduced or raised) in the free streaming regime compared to the results obtained in the neutrinospheric region. Until about (0.8–1) s after bounce, the accretion-affected contributions of all neutrino species therefore decrease or increase the total neutrino-induced NS kick at 400 km only moderately relative to the values computed at $10^{11} \text{ g cm}^{-3}$ and $10^{12} \text{ g cm}^{-3}$ (Figure 12).

While earlier than (0.8–1) s after bounce neutrino emission and scattering in mass flows accreted by the PNS have an influence, accretion becomes insignificant at later times, but absorption and scattering of high-energy $\bar{\nu}_e$ and ν_x in asymmetric downflows still play a role outside of the gain radius. This effect mostly concerns $\bar{\nu}_e$ and ν_x because of their higher-energy spectra. It is visible in Figure 12 by the evolution of the relative angle between hydrodynamic NS kick and neutrino-induced NS kick from values larger than 90° , which is expected for the accretion phase (Figure 8, left panel), to angles of less than 90° , which is a characteristic feature of neutrino interaction in non-accreted downflows (Figure 8, right panel). Moreover, the persistent importance of absorption and scattering of $\bar{\nu}_e$ and ν_x in asymmetrically distributed matter in the gain layer at $t \gtrsim 0.8$ s after bounce can also be concluded from the fact that their NS kicks deduced at the gain radius and at 400 km exhibit large differences.

All such effects had also been witnessed in model s12.28 (Figure 11), where the interplay of the LESA dipole fluxes with the ν_e , $\bar{\nu}_e$ accretion emission and ν_x scattering determined the final PNS kick velocity deduced from the neutrino flux asymmetries measured at large radii. However, in model s18.88 the late-time scattering effects in non-accreted downflows are so strong that the hydrodynamic and neutrino kicks at t_f^ν possess a small relative angle of $\sim 10^\circ$ only (Table 3). During the subsequent long-time evolution, however, the relative angle grows because of changes in the ejecta geometry, and it is large at the end of the simulations in all of the four models of s12.28, s18.88, s20, and s20e (Table 2). Remarkably, there is a sizable difference between our two long-term simulations of the $20 M_\odot$ model because of

their different explosion geometries (Kresse, 2023). Another significant difference between s12.28 on the one hand and s18.88 and s20 on the other hand is the aforementioned fact that in model s12.28 the time-integrated anisotropy parameter $\bar{\alpha}_{\nu_e}$ attains a value close to the (fluctuating) instantaneous values of α_{ν_e} (Figure A3), whereas in the s18.88 and s20 models the time-averaged emission asymmetry parameters of all neutrino species become much smaller than their instantaneous values (Figures A5 and A6).

3.2.2 A note on the evaluation radius

As we have seen in Figures 11 and 12 as well as Figures B7–B9, the results for the neutrino kicks can vary drastically depending on the radial position where the neutrino flux anisotropy is determined. Only our electron-capture SN-like model z9.6 is an exception and shows less sensitivity (Figure 10), because in this case asymmetric downflows to the PNS and long-time non-spherical accretion do not play a role. As already discussed in Section 2.3.1, the most consistent and unambiguous calculation of the final NS kick that has a clear interpretation of the underlying physics is based on a consideration of the linear momentum of the ejected gas for the hydrodynamic kick, i.e., of the gas exterior to the surface of the compact remnant at any time, and of the linear momentum of the neutrinos escaping to infinity for the neutrino kick, i.e., of the neutrino flux in the free-streaming limit, where further interactions of neutrinos with the stellar matter are no longer relevant, for which we chose a radius of 400 km (following Stockinger et al, 2020).

Alternatively, one could also evaluate the forces acting at a certain radius, hydrodynamic forces according to Section 2.3.3 as well as those connected to neutrinos, using the same radius for all of the forces. This approach was taken by Coleman and Burrows (2022). However, it has the disadvantage that the decomposition of the kick contributions due to hydrodynamic and neutrino forces in such an approach depends strongly on the choice of the evaluation radius and therefore its interpretation is not unambiguous. Coleman and Burrows (2022) picked a radius that corresponds to the mass coordinate of the final NS after mass accretion has ended, i.e., they considered a location analogue to the coordinate of the

“mass cut” often used in 1D models. Although this makes sense in principle, in exploding 3D models there is no Lagrangian mass coordinate of the progenitor that ultimately separates ejecta from NS material. Different from the 1D case, ejecta and NS matter in 3D simulations originate from different radii and thus different enclosed masses of the progenitor profile.⁸

Following the approach of Coleman and Burrows (2022) for models that form BHs without any explosive mass ejection, one would have to calculate the forces at the edge of the collapsing progenitor, which defines the ultimate mass cut. Evaluated at the surface of the star in the case of complete collapse, or in a spherical progenitor also at any other large radius, the hydrodynamic forces would not transfer any linear momentum to the compact remnant. This is the correct final outcome if no aspherical mass ejection takes place. Such an analysis performed in the free-streaming regime would also yield the correct neutrino recoil kick associated with the linear momentum carried away by the radiated neutrinos. However, this analysis would not permit to monitor the temporary recoil that the PNS receives by anisotropically moving, transiently expanding postshock gas in its surroundings. Evaluating all forces due to hydrodynamic and neutrino effects at a small radius near the neutrinospheres or at the surface of the PNS instead, would lead to incorrect results for the neutrino kick, because it ignores the neutrino interactions in dense, aspherical postshock gas that the neutrinos need to cross before they escape to infinity.

We therefore apply our standard procedure of computing hydrodynamic and neutrino-induced kicks also to cases where our 3D simulations lead to BH formation, which means that we determine the (transient) hydro kicks from the gas momentum of (temporary) ejecta and the neutrino kicks from the momentum of the neutrino flux in the free-streaming regime.

⁸In the more recent paper by Burrows et al (2023b) the choice of the “outer mass surface” of the final PNS seems to have been abandoned and replaced (for the calculation of the neutrino component) by the PNS radius located at a density-isosurface of $10^{11} \text{ g cm}^{-3}$. As we argued in Section 2.3.1 and demonstrated by results in Section 3.2.1, such a choice can be problematic, too, because it leads to an incorrect balancing of hydrodynamic kick and neutrino-induced kick, if the hydro and neutrino kicks are evaluated at different radii.

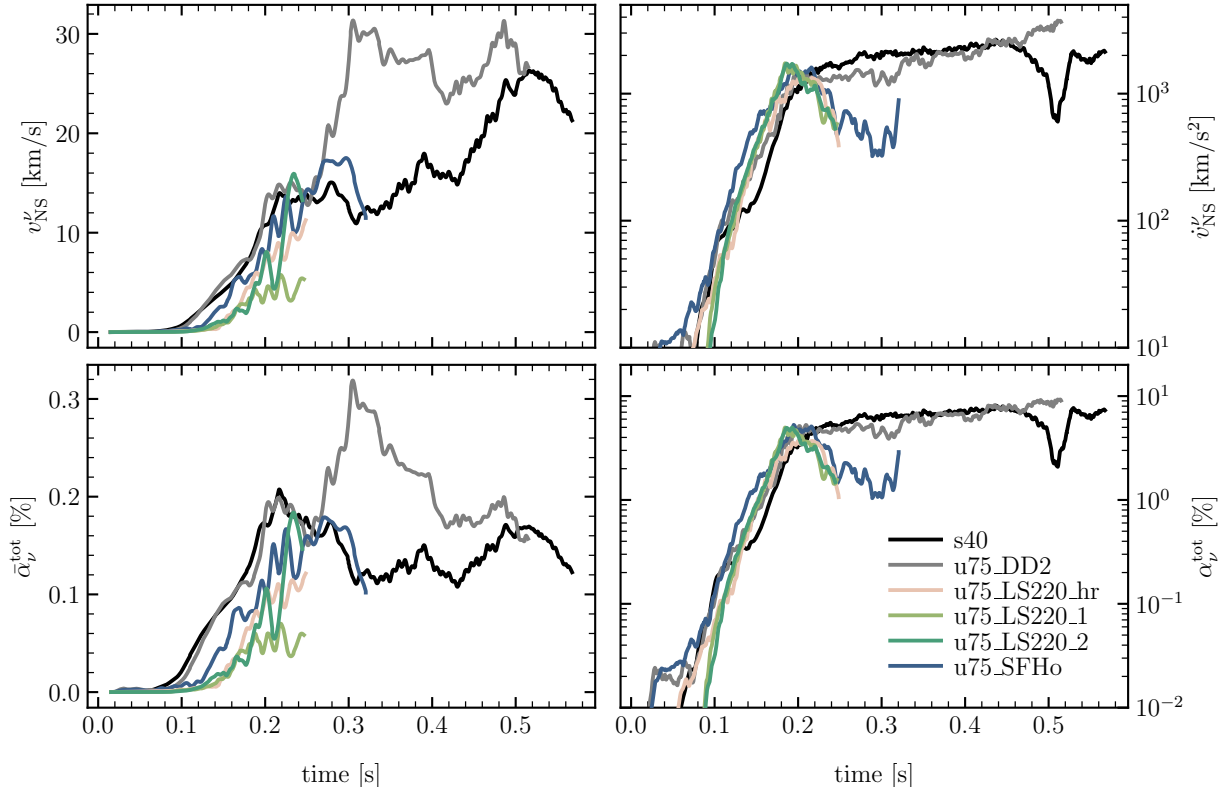


Fig. 13 Neutrino-induced kick velocity of the PNS (or proto-BH) (*top left*), corresponding acceleration by anisotropic neutrino emission (*top right*), time-integrated anisotropy parameter of the total neutrino emission (Equation 24; *bottom left*), and corresponding instantaneous neutrino anisotropy parameter (Equation 22; *bottom right*) for all BH-forming models

3.2.3 Neutrino kicks of black holes

Although some of our 3D simulations with BH formation exhibit a phase of transient shock expansion shortly before the PNS collapses, explosive and asymmetric mass ejection is not expected to happen in any of these models (see Section 2.2). Therefore the residual BHs receive a natal kick only by the anisotropic loss of neutrinos.

Figure 13 provides an overview of the evolution of the PNS kicks until the instant when the PNS becomes gravitationally unstable and our simulations were stopped. For the $75 M_{\odot}$ progenitor this moment is reached between ~ 250 ms and 325 ms after bounce, except with the stiff DD2 EoS, where it takes more than 500 ms and thus similarly long as in the case of the $40 M_{\odot}$ model, which was simulated with the much softer LS220 EoS. The maximum PNS kicks are only around 30 km s^{-1} . Despite the enormous values of the acceleration of up to several 1000 km s^{-2}

at the end of our computed evolution, one cannot count on any relevant further gain in velocity, because the anisotropically distributed postshock matter will be swallowed by the newly formed BH within a few milliseconds at most (see Rahman et al, 2022, for similar simulations showing the evolution beyond BH formation). After this short period, the matter of the non-rotating progenitor stars will fall into the BH basically spherically and the neutrino emission will become very low and effectively isotropic.

Table 3 contains a summary of relevant quantities for our BH forming models, too. In the last two columns we also provide estimates of the final BH kicks, which are smaller than the final PNS kicks by a factor $M_{\text{NS,g}}(t_{\text{f}}^{\nu})/M_{\text{BH}}(t \rightarrow \infty)$ because of momentum conservation: the final BH will be more massive but will possess the same momentum as the NS at the moment of its gravitational implosion. Here, we distinguish two cases, namely

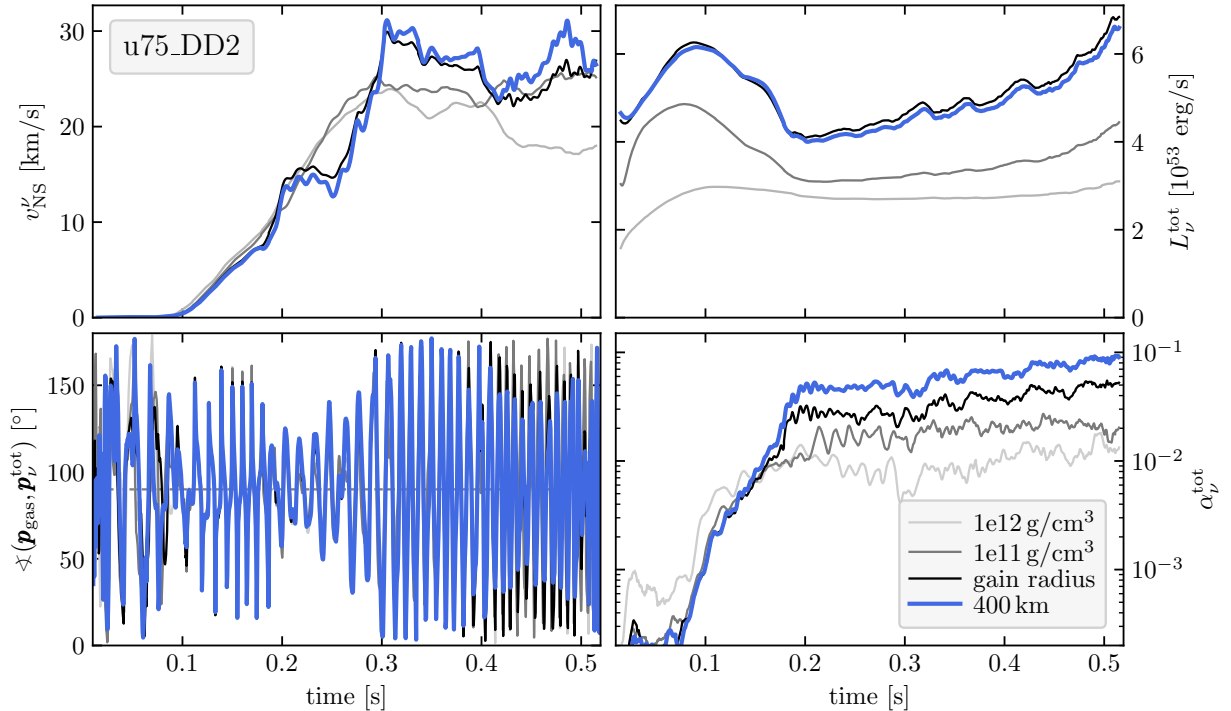


Fig. 14 Same as Figure 10, but for the BH forming model u75_DD2. Up to roughly one third of the total neutrino luminosity is produced by neutrino emission at densities below $10^{11} \text{ g cm}^{-3}$ in massive, non-spherical accretion flows onto the transiently existing PNS (or proto-BH). The values of the instantaneous anisotropy parameter of the neutrino emission (*bottom right*) are therefore very sensitive to the radial position where they are determined. Physics-wise meaningful results require an evaluation of the neutrino-induced kick in the free-streaming regime (400 km)

one where the entire pre-collapse mass of the progenitor ends up in the BH, and another case where just the progenitor’s helium core is accreted and the hydrogen envelope becomes gravitationally unbound because of the so-called mass-decrement effect, i.e., because of the reduced gravitational potential due to the energy loss in neutrinos (Lovegrove and Woosley, 2013; Nadezhin, 1980). The $\sim 15.2 M_{\odot}$ BH formed in the collapse of our $40 M_{\odot}$ progenitor thus receives a natal kick of $\sim 3.3 \text{ km s}^{-1}$, whereas the BH left by the $75 M_{\odot}$ progenitor will have a mass in the range between $\sim 54.7 M_{\odot}$ and $\sim 74 M_{\odot}$ and a neutrino-induced kick of less than $\sim 1 \text{ km s}^{-1}$. A graphical overview of these results is presented in the right panel of Figure 4.

It is important to note that in spite of high values of the instantaneous neutrino-emission asymmetry parameter $\alpha_{\nu}^{\text{tot}}$ of up to 10%, the time-averaged values $\bar{\alpha}_{\nu}^{\text{tot}}$ are one to two orders of magnitude lower and only in the range of 0.1%–0.2% (Figure 13). The enormous reduction is caused by

the rapid variations of the kick directions, which force the average effect to much smaller amplitudes. This can be concluded from the lower left panel of Figure 14 and the third panels from top in the right columns of Figures C10–C15. The short-timescale variability of the relative angle between hydrodynamic and neutrino kicks seen there is linked to rapid fluctuations of both the gas momentum vector and of the momentum vector of the anisotropically radiated neutrinos. These directional variations are connected to stochastic changes of massive, anisotropic accretion downflows to the PNS, whose neutrino emission fluctuates wildly.

Figure 14, which depicts a representative example of our BH forming models, and Figures C10–C15 reveal the crucial role of accretion emission for the neutrino emission asymmetry. The upper right panel of Figure 14 demonstrates that up to $\sim 30\%$ of the total neutrino luminosity originate from the accretion mantle exterior to a (angle-averaged) density of $10^{11} \text{ g cm}^{-3}$, and

the lower right panel conveys the information that the emission from the layer between this density and the angle-averaged gain radius as well as neutrino scattering and absorption between the gain radius and 400 km are mainly responsible for the high values of the instantaneous neutrino asymmetry parameter. Characteristic signatures of accretion-governed neutrino kicks are also visible in Figures C10–C15. On the one hand, the bottom right panels there exhibit nearly aligned directions of the force vectors $\hat{\mathbf{p}}_{\nu_i}$ for ν_e , $\bar{\nu}_e$, and ν_x during most of the simulated periods of evolution. On the other hand, they also show that the hydro-kick force vector, $\hat{\mathbf{p}}_{\text{gas}}$, and the total neutrino-kick force vector, $\hat{\mathbf{p}}_{\nu}^{\text{tot}}$, are mostly in opposite hemispheres (i.e., the relative angle between them is larger than 90° most of the time). Both of these findings are typical of the situation that is expected when massive accretion flows produce neutrinos of all species (see left panel of Figure 8).

Only during short phases around ~ 0.1 s after bounce in models s40 and u75_DD2 one can witness trends towards the LESA-typical anti-alignment between the ν_e acceleration direction on the one side and the $\bar{\nu}_e$ and ν_x acceleration directions on the other side (Figure 7). These indications of LESA effects, however, remain confined to short episodes during the early postbounce evolution of the two models, because the LESA dipole emission is quickly suppressed in BH forming models, where the LESA-driving convective shell in the PNS interior gets buried deep below a thick, convectively stable accretion mantle (Walk et al, 2020), which grows rapidly due to the extremely high mass-infall rates (see upper left panels of Figures C10–C15).

4 Discussion and conclusions

4.1 Summary

We have presented a detailed and comprehensive evaluation of hydrodynamic and neutrino-induced NS and BH kicks that we obtained in a set of long-time 3D stellar collapse simulations with the PROMETHEUS-VERTEX/NEMESIS code of the Garching group. The model set includes successful SN explosions of progenitor stars with ZAMS masses of 9.0, 9.6, 12.28, 15.0, 18.88, and 20.0 M_\odot as well as BH forming cases for progenitors with ZAMS masses of 40 M_\odot and 75 M_\odot .

The elaborate neutrino transport with the VERTEX module was applied until the PNS collapsed to a BH or well beyond the onset of the neutrino-driven SN explosion. Thus a post-bounce evolution of typically ~ 0.5 s was covered, in our exploding 12.28 M_\odot and 18.88 M_\odot models indeed much longer, namely more than 4 s and nearly 2 s after bounce, respectively. All hydrodynamic SN simulations (except the 12.28 M_\odot model) were continued until the explosion energies were nearly saturated, using our newly developed NEMESIS module, which provides an approximate but still sophisticated, computationally efficient treatment of the neutrino effects inside and in the surroundings of the PNS. The NEMESIS scheme allows one to obviate the use of time-consuming 3D neutrino transport while employing neutrino results from 1D neutrino-hydrodynamics simulations of PNS cooling with the PROMETHEUS-VERTEX code including PNS convection via a mixing-length description.

Our analysis of the kicks is based on the time integration of forces expressed by the time derivatives of the total linear momentum of the ejecta (i.e., gas in the surroundings of the PNS) and of the linear momentum carried away by escaping neutrinos in the free-streaming limit. In course of this time integration we take into account the changes of the gravitational mass of the PNS due to its neutrino losses (Equations 11 and 12 in Section 2.3.1). Thus our approach is consistent with previous analyses of neutrino and hydrodynamic kicks by the Garching group, for example in Stockinger et al (2020) and Bollig et al (2021), but it is slightly more accurate.

Our long-term 3D simulations yield hydrodynamic (total) NS kicks between ~ 10 km s^{-1} ($\gtrsim 60$ km s^{-1}) and ~ 1290 km s^{-1} ($\gtrsim 1300$ km s^{-1}), with the highest values still growing when our calculations were stopped after several seconds of postbounce evolution (Table 2 and Figure 3). The contributions of neutrino-induced kicks to the total values are between ~ 45 km s^{-1} and ~ 140 km s^{-1} during the periods computed with full neutrino transport and between ~ 150 km s^{-1} and ~ 260 km s^{-1} according to our best-guess estimates (Equation 25) based on an extrapolation of the conditions found at the end of our transport calculations (Table 3 and Figure 4).

We witness a complex interplay of hydrodynamic and neutrino-induced kicks, whose combined effect determines the total natal kick the NS receives at its birth. In line with previous findings (Stockinger et al, 2020; Bollig et al, 2021; Burrows et al, 2023b) we obtained neutrino-induced NS kicks dominating in the explosions of low-mass progenitors (our $9.0 M_{\odot}$ and $9.6 M_{\odot}$ cases) and hydrodynamic NS kicks clearly dominating in the successful explosion models of our progenitors with $15 M_{\odot}$ and more. The $12.28 M_{\odot}$ model is an intermediate case, where the hydro kick is still higher but the neutrino kick contributes significantly (Figure 4). Because of a large angle between the hydrodynamic kick and the neutrino kick (which corresponds to the most probable relative orientation of both kicks), the neutrino contribution does not have a great impact on the absolute value of the total NS velocity in this model, but it still has a considerable influence on its direction. Overall, however, hydrodynamic recoil should dominate the observed kicks of most NSs except those born in the core collapse of the lowest-mass SN progenitors. Therefore neutrino-induced kicks should not have a severe impact on the morphological properties of SN remnants with high-velocity NSs, which are predicted to possess stronger explosions and to eject the major fraction of the intermediate-mass and iron-group elements in the hemisphere pointing opposite to the NS’s kick vector (Wongwathanarat et al, 2013, 2017), in agreement with a larger number of closely investigated remnants of relatively recent and near galactic SNe (Holland-Ashford et al, 2017; Katsuda et al, 2018).

In a careful analysis of the individual matter forces (gravity, pressure, momentum flow; Scheck et al, 2006) in all of our models, we demonstrated that usually the gravitational effect as a long-range force between NS and ejecta is the dominant one for determining the magnitude and direction of the final hydrodynamic kick over long evolution times (Figure 6). Since also later fallback, which can have an impact on the final ejecta and their linear momentum at very late times, is governed by the influence of the NS’s gravity on the innermost, temporary ejecta, our results justify the use of the term “gravitational tug-boat effect” (Wongwathanarat et al, 2013) for the mechanism producing the hydrodynamic NS kicks.

In our BH forming models the NSs (or proto-BHs) receive neutrino-induced kicks of $10\text{--}30 \text{ km s}^{-1}$ until they become gravitationally unstable and collapse. Since shock expansion is weak or absent in our simulations, explosive, asymmetric mass ejection is not expected to happen, but the newly born BHs will swallow the progenitor’s helium core or possibly the whole mass of the pre-collapse star. Therefore, applying momentum conservation, the final BH kicks in such failed SNe will be reduced to at most a few km s^{-1} , exclusively caused by the anisotropic neutrino loss during the transient existence of the NSs (Table 3). These results receive support by a detailed investigation of the massive BH binary system VFTS 243, where a $\sim 10 M_{\odot}$ BH exists in a nearly circular orbit, suggesting that it was born from a stripped progenitor with mass-energy just being lost by neutrinos but no ejected matter (Vigna-Gómez et al, 2023). The estimated most likely value of about 4 km s^{-1} for the natal kick velocity of the BH and a best-fit value of $\lesssim 0.2\%$ for the neutrino emission asymmetry are perfectly well compatible with our results, in particular our s40 model, which is expected to form a $\sim 15.2 M_{\odot}$ BH with a natal kick of 3.3 km s^{-1} and a neutrino emission asymmetry of 0.13% .

In fallback SNe, where a powerful, asymmetric SN explosion is launched by the neutrino-driven mechanism before the NS collapses to a low-mass BH, the BH kicks can be much larger, as predicted by Janka (2013) and recently found in 3D simulations by Chan et al (2020) and Burrows et al (2023a,b). Here, the NS collapses due to the fallback accretion of initially ejected matter that does not become gravitationally unbound. The fallback mass is sufficiently large to push the NS beyond its upper mass limit, but it is also sufficiently small—and the SN shock is sufficiently strong—to allow the initial asymmetry of the blast wave to survive and to expel the far dominant fraction of the star. This combination of conditions requires quite some fine-tuning of the strength of the SN explosion, but the mentioned 3D simulations demonstrate that this possibility, which was pointed out to exist in principle by Janka (2013), could be realized in some stellar collapse events.

Our combined analysis of hydrodynamic and neutrino kicks reveals three characteristically different phases for the neutrino kicks in core-collapse simulations of massive progenitors.

After the LESA-minted early postbounce phase (Figure 7), the LESA effects are overruled by anisotropic neutrino emission (mainly of ν_e and $\bar{\nu}_e$) from accretion downflows onto the PNS (Figure 8, left panel). Later, well after SN shock revival, when the mass accretion by the PNS has effectively ended, the non-isotropy of the fluxes of neutrinos escaping to infinity is affected by absorption and scattering (mainly of $\bar{\nu}_e$ and ν_x) in nonradial downflows that penetrate to the close vicinity of the PNS but are not accreted (Figure 8, right panel). We argued that it is crucial to measure the neutrino flux asymmetry in the free-streaming regime because of the non-negligible interaction of neutrinos in the downflows. The corresponding momentum transfer to the stellar medium changes the linear momentum of both escaping neutrinos and ejected gas. Measuring neutrino emission asymmetries near the neutronospheres or PNS surface may thus lead to a double-counting of momentum contributions in the sum of neutrino and hydrodynamic kicks, if the hydrodynamic forces are evaluated at a different radius or from the total gas momentum. For the same reason the neutrino-induced kick velocities of BHs should be evaluated in the free streaming limit, in particular, if the evaluation is stopped at the time of BH formation but the gas momentum is subsequently reduced by fallback of asymmetrically distributed matter to the BH.

4.2 Discussion

Our results are in overall agreement with the findings reported by Burrows et al (2023b) on grounds of an impressively large set of recent long-term 3D simulations that also provide data of neutrino-induced NS and BH kicks, and all together their and our 3D models confirm a variety of insights already discussed in previous literature (e.g., Podsiadlowski et al, 2004; Janka, 2013, 2017; Tauris et al, 2017; Gessner and Janka, 2018; Müller et al, 2019; Stockinger et al, 2020; Chan et al, 2020). However, our current set of 3D simulations is too small to deduce statistical information and to draw firm conclusions on integral population properties, for example regarding any tendency of NS spin-kick alignment or a bimodal vs. single-peaked distribution of NS kicks. Our models compared to those of Burrows et al (2023b) exhibit roughly similar magnitudes of the hydrodynamic as well

as neutrino kicks and they reveal similar general trends. Nevertheless, our neutrino kicks of BHs tend to be considerably lower, which may be connected either to our earlier BH formation times or to the differences in our analysis of the anisotropic loss of neutrinos as discussed in Sections 2.3.1 and 3.2.2. Possibly for the same reason we also witness values of the instantaneous neutrino emission asymmetry parameter that are significantly lower (by a factor of roughly 2–3) than those plotted in Coleman and Burrows (2022), and we get an even greater reduction of this asymmetry measure when considering time-averaged values.

A specific and quantitative comparison of individual models is impeded by the fact that the only case our model set and the one of Burrows et al (2023b) have in common is the $9.0 M_\odot$ model, which develops an explosion energy of 0.052 B in our simulation, whereas Burrows et al (2023b) report a value of 0.107 B, more than twice higher. We generally find explosion energies that are significantly lower (see discussions in Stockinger et al, 2020; Bollig et al, 2021). Moreover, we obtain self-consistent explosions in all of our 3D models only under special circumstances (see summary in Section 2.2), e.g., for low-mass progenitors (Melson et al, 2015b, 2020; Stockinger et al, 2020), rapid rotation (Summa et al, 2018), with slight changes in the neutrino opacities (Melson et al, 2015a), and with 3D perturbations in the convective oxygen-burning layer of the progenitor prior to collapse (Bollig et al, 2021). Therefore we expect sizable quantitative differences and probably even qualitatively different outcomes if individual cases could be confronted with each other.

Contrary to what is stated in Coleman and Burrows (2022), we have witnessed clear evidence that LESA dipole emission (i.e., a strong dipole component in the electron-lepton number emission by ν_e and $\bar{\nu}_e$; Tamborra et al, 2014) determines the neutrino-induced kick of NSs born in the collapse of progenitors near the low-mass end of stars exploding as SNe. LESA-dominated neutrino kicks manifest themselves by an anti-alignment of the ν_e -induced kick on the one side and $\bar{\nu}_e$ - and ν_x -induced kicks on the other side; the net effect is a total neutrino kick aligned with the LESA dipole vector (Figure 7). This concerns our $9.0 M_\odot$

model and also the electron-capture-SN-like explosion of the $9.6 M_{\odot}$ model (see also [Stockinger et al, 2020](#)). In the latter case, where the explosion develops rapidly and a phase of massive downflow activity around the PNS after shock revival is absent, the ejecta asymmetry is even influenced by the anisotropic neutrino heating due to the LESA dipole (see [Tamborra et al, 2014](#)), making the blast wave stronger in the anti-LESA direction. Therefore neutrino kick and hydrodynamic kick of the NS are aligned in this model, both directed collinearly with the LESA dipole vector ([Stockinger et al, 2020](#)).

But we also find that LESA affects the neutrino kick during the first few hundred milliseconds after core bounce in most other models with more massive progenitors, although in these cases LESA is not crucial for the final values of the neutrino kicks. This also holds true for the BH forming cases, where the LESA effects are significantly weakened by the high mass-accretion rates, which lead to the rapid formation of a massive accretion mantle around the PNS, thus burying the LESA-driving convective shell inside the PNS deep below a thick, convectively stable outer layer ([Walk et al, 2020](#)). Our rapidly rotating $15 M_{\odot}$ explosion model is the only case where signatures of neutrino-emission asymmetries connected to LESA are absent, because rapid rotation suppresses PNS convection and thus the LESA dipole emission ([Walk et al, 2019](#)). Nevertheless, this model is expected to develop a high neutrino-induced NS kick because of a large hemispheric asymmetry of massive accretion downflows near the equatorial plane. Both neutrino and hydro kicks have big inclination angles to the rotation axis and a big relative angle, too.

4.3 Conclusions

The ubiquitous presence of neutrino-induced NS kicks between more than 50 km s^{-1} and up to possibly over 150 km s^{-1} defines a floor value for the natal kick velocity. This floor value is dominant for NSs born in explosions of stars near the low-mass end of SN progenitors, where the LESA dipole emission determines the kick, and it is exceeded by the hydrodynamic kicks in more massive progenitors. Interestingly, the spatial velocity of the Crab pulsar is inferred to be around 160 km s^{-1} (with fairly big uncertainties; [Hester, 2008](#); [Kaplan et al,](#)

[2008](#)). This kick magnitude is hard to explain by the hydrodynamic kick in the explosion of a low-mass progenitor, which is preferred as an explanation of SN 1054 because of its low explosion energy (for a detailed discussion, see [Stockinger et al, 2020](#); [Gessner and Janka, 2018](#)). However, a neutrino kick of the NS in such an explosion may provide a natural explanation.

The existence of a floor value for the NS kick, suggested by our results as well as those of [Burrows et al \(2023b\)](#), might demand a reconsideration of formation paths of low-mass X-ray binaries in globular clusters and NSs that stay bound in these environments (e.g., [Ivanova et al, 2008](#)). Low-velocity natal NS kicks might require an efficient (nearly perfect) compensation of hydrodynamic and neutrino-induced kicks in SN explosions where both kicks possess similar magnitudes but can stochastically attain opposite directions. The recent sets of 3D SN models suggest that progenitors in the mass range between $\sim 10 M_{\odot}$ and $\sim 13 M_{\odot}$ might qualify as candidates for such a scenario.

The work discussed in this paper has led to a better understanding of the interplay of hydrodynamic NS kicks due to the gravitational tugboat mechanism and neutrino-induced NS and BH kicks due to anisotropic neutrino losses. More work is necessary, in particular a much larger set of models is needed, in order to draw statistical conclusions (e.g., on a trend/lack of NS spin-kick alignment or anti-alignment) and to arrive at information on population-integrated properties (e.g., the measurable distribution of NS kicks). Also longer 3D simulations with our sophisticated VERTEX neutrino transport are needed (such as the ones we presented for models s12.28 and s18.88) in order to ameliorate our best-guess estimates of the finally achievable neutrino-induced kick velocities of NSs. Some may also consider the use of the RbR+ approximation in our VERTEX code for neutrino transport in multi-dimensional simulations as a deficiency, although we have shown that the RbR+ neutrino treatment in 3D SN simulations does not lead to any fundamental differences compared to multi-D transport, neither in the hydrodynamical evolution ([Glas et al, 2019b](#)) nor in the development of the LESA dipole asymmetry of the PNS's neutrino emission ([Glas et al, 2019a](#)). In our view a more problematic shortcoming in all of the present SN simulations

is the fact that the NS is pinned to the center of the polar coordinate grid and therefore effects connected to the kick-driven movement of the PNS are neglected (Janka et al, 2022). Finally, a direct, detailed, and quantitative comparison with other long-term 3D simulations employing sophisticated neutrino transport in the recent literature (e.g., Burrows et al, 2023b) may be of interest for the wider community.

Acknowledgments. We are grateful to Bernhard Müller and Naveen Yadav for their initial work of performing 3D progenitor simulations and Tobias Melson, Alexander Summa, and Robert Bollig for their 3D core-collapse simulations analysed in this work. The presented study was supported by the German Research Foundation (DFG) through the Collaborative Research Centre “Neutrinos and Dark Matter in Astro- and Particle Physics (NDM),” Grant No. SFB-1258-283604770, and under Germany’s Excellence Strategy through the Cluster of Excellence ORIGINS EXC-2094-390783311. The authors are grateful to the Gauss Centre for Supercomputing e.V. (GCS; www.gauss-centre.eu) and to the Leibniz Supercomputing Centre (LRZ; www.lrz.de) for computing time on the supercomputers SuperMUC and SuperMUC-NG at LRZ under LRZ project IDs pn69ho and pn25me as well as GAUSS Call 13 project ID pr48ra, GAUSS Call 15 project ID pr74de, and GAUSS Call 17 and Call 20 project ID pr53yi. Computer resources for this project were also provided by the Max Planck Computing and Data Facility (MPCDF) on the HPC systems Cobra, Draco, and Raven.

Declarations

Data availability. Data of the model analysis can be made available upon request.

Code availability. The codes used for the 3D simulations and post-processing analysis were developed at the Max Planck Institute for Astrophysics and are not public source.

Conflict of interest. The authors declare no competing interests.

Ethics approval. Not applicable.

Consent to participate. All authors contributed to the work and approved sending the paper for publication.

Authors’ contributions. HTJ initiated the project and did most of the writing. DK performed the analysis of the 3D simulations, did most of the figures, and provided inputs for the written text.

Consent of publication. All authors agree for the work to be published in Astrophysics and Space Science.

Funding note. Open Access funding enabled and organized by Projekt DEAL. Funding through academic grants is listed in the Acknowledgements section.

Appendix A Overview: detailed time evolution of exploding models

Figures A1–A6 in this appendix display detailed information about the postbounce evolution of relevant diagnostic quantities for all of our 3D stellar collapse simulations with successful explosions. The displayed time intervals are constrained to the periods that were simulated with full VERTEX neutrino transport (ending at times t_f') in order to relate hydrodynamic and neutrino kicks during the postbounce phase when both are computed, and to compare the characteristic properties specific to the different models against each other.

For the hydrodynamic and total kick velocities as well as their angles relative to the neutrino-induced kick velocity, results for $v_{\text{NS}}^{\text{hyd}} = |\mathbf{v}_{\text{NS}}^{\text{hyd}}|$ and $v_{\text{NS}}^{\text{tot}} = |\mathbf{v}_{\text{NS}}^{\text{tot}}|$ according to the acceleration integrals of Equations (13) and (15) are plotted with solid lines; the time evolution of these kick velocities is also displayed in Figure 3 and their values at $t_f \geq t_f'$ are given in Table 2 and Figure 4. We compare them with results for $v_{\text{NS}}^{\text{hyd,mc}} = |\mathbf{v}_{\text{NS}}^{\text{hyd,mc}}|$ and $v_{\text{NS}}^{\text{tot,mc}} = |\mathbf{v}_{\text{NS}}^{\text{tot,mc}}|$ computed from the total gas momentum and the total momentum of escaping neutrinos via the approximate expressions of Equations (16) and (17), respectively, which constitute lower bounds for the hydrodynamic and total kicks (dashed lines).

In general, there is excellent agreement obtained with the two complementary methods of evaluation, except for minor systematic differences that are natural when a lower bound is compared with the more accurate values ($v_{\text{NS}}^{\text{hyd,mc}} \leq v_{\text{NS}}^{\text{hyd}}$ and $v_{\text{NS}}^{\text{tot,mc}} \leq v_{\text{NS}}^{\text{tot}}$; see the discussion in Section 2.3.2). Clear discrepancies, mainly in the angles of $\mathbf{v}_{\text{NS}}^{\text{hyd}}$ and $\mathbf{v}_{\text{NS}}^{\text{hyd,mc}}$ relative to the neutrino-kick velocity $\mathbf{v}_{\text{NS}}^{\nu}$, can be witnessed only during transient phases with very low absolute values of the hydrodynamic kicks and rapid temporal variations of the corresponding kick directions. The corresponding numerical inaccuracies of the kick evaluation concern mainly models s9.0 and s20, but also lead to episodes when $v_{\text{NS}}^{\text{hyd,mc}} > v_{\text{NS}}^{\text{hyd}}$ and $v_{\text{NS}}^{\text{tot,mc}} > v_{\text{NS}}^{\text{tot}}$ holds on a low level in model m15.

It should be noted that in Figures A1–A6 the plotted results for all quantities, except the angles of $\mathbf{v}_{\text{NS}}^{\text{hyd}}$ and $\mathbf{v}_{\text{NS}}^{\text{hyd,mc}}$ relative to $\mathbf{v}_{\text{NS}}^{\nu}$ and the time-integrated neutrino energy losses, are smoothed by applying a running average over time intervals of 10 ms. The same holds true for all curves displayed in Figure 9. This implies that the first and last 5 ms of the simulated periods of evolution are not shown, which leads to small discrepancies between the plotted final values and the true final values listed in Table 3.

Appendix B Neutrino-species dependent NS kicks in model s12.28

Figures B7, B8, and B9 in this appendix present an in-depth analysis of the neutrino-induced NS kicks for all neutrino species individually and at different radial positions in model s12.28. The evaluation is performed at radii where the angle-averaged densities are $10^{11} \text{ g cm}^{-3}$ and $10^{12} \text{ g cm}^{-3}$, which are locations close to the PNS surface and around the neutrinospheres. In addition, it is also conducted at the angle-averaged gain radius and at a radius of 400 km. The first two positions at high densities permit to extract information about the neutrino emission originating from inside the PNS and of asymmetry effects associated with the LESA dipole, whereas the additional analysis at the gain radius permits

conclusions on contributions by the neutrino radiation produced in accretion flows onto the PNS. The analysis at 400 km yields the observationally relevant results in the free-streaming regime of neutrinos, which allow for an unambiguous interpretation of the neutrino kicks in their interplay with the hydrodynamic kicks. Moreover, in comparison with the results obtained at the gain layer, it yields insights into the consequences connected to absorption and scattering of neutrinos above the gain radius.

At each of these radii the neutrino fluxes for computing the neutrino forces according to Equation (5) are transformed from the comoving frame of the stellar fluid, where the transport is solved, into the laboratory frame of a distant observer, which is coincident with the rest frame of the PNS (because the PNS is fixed at the coordinate center of the polar Yin-Yang grid used for the computations). Note that our VERTEX transport solver employs the RbR+ approximation in multi-dimensional simulations, which only provides radial neutrino fluxes. The disregard of nonradial flux components implies approximate results for the neutrino force calculations with Equation (5). The loss of accuracy should, however, be a minor effect, because near the PNS surface and outside the PNS the radial flux components are the far dominant ones.

In all of the figures of this appendix (and in Figures 10–12 and 14) the curves for the neutrino-induced kick velocities, neutrino luminosities, and neutrino anisotropy parameters have been smoothed by applying running means over time intervals of 10 ms.

Appendix C Overview: detailed time evolution of BH forming models

Figures C10–C15 display, in analogy to Figures A1–A6 in Appendix A, the detailed post-bounce behavior of the diagnostic quantities that are most relevant for the dynamical evolution, neutrino emission, and proto-BH kicks in all of our 3D stellar collapse simulations that lead to BH formation. The plots cover the evolution until

s9.0 (LS220, SMR)

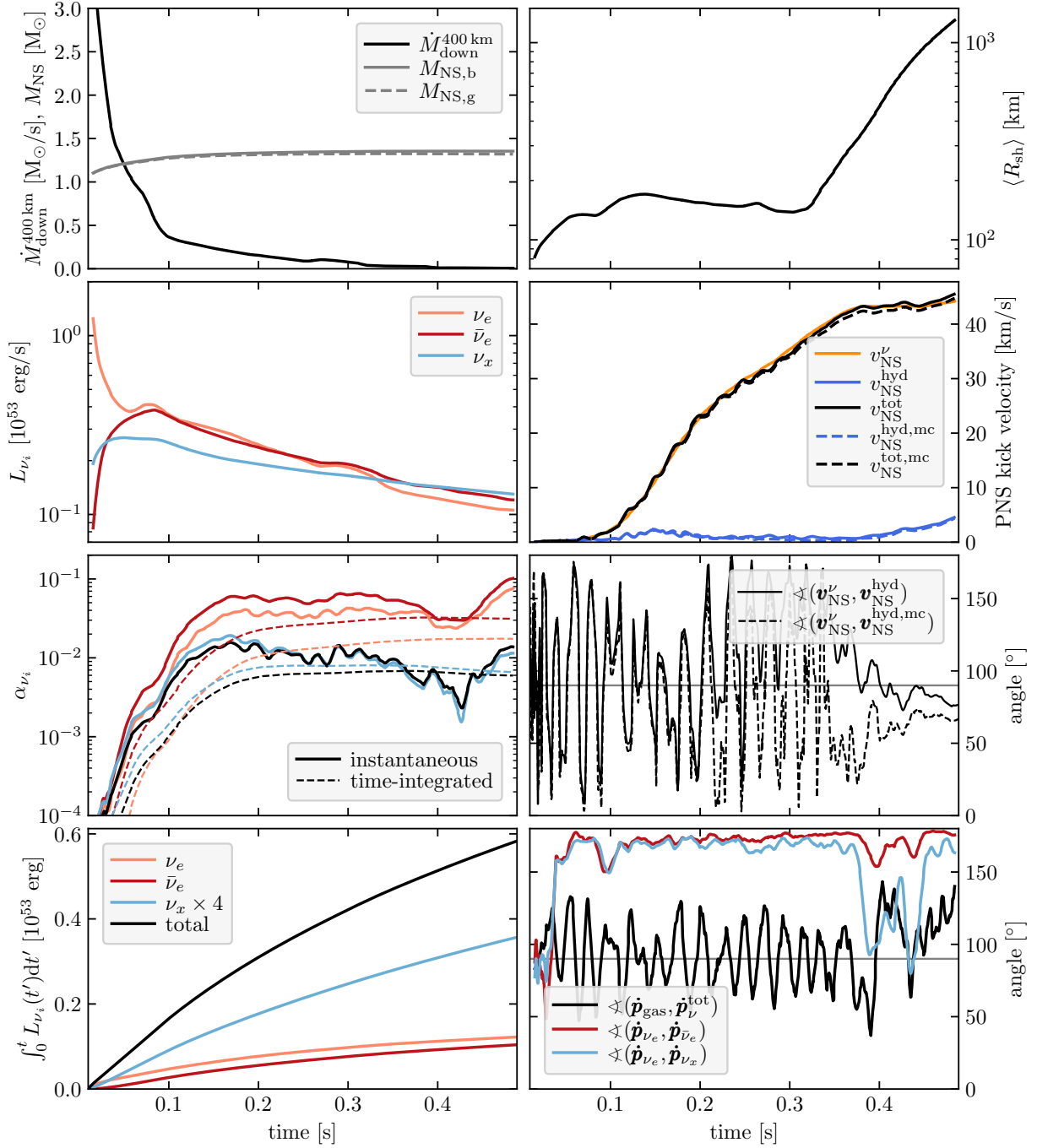


Fig. A1 Characteristic quantities as functions of postbounce time for the dynamical evolution, neutrino emission, hydrodynamic NS kick ($v_{\text{NS}}^{\text{hyd}}$; Equation 13), neutrino-induced NS kick (v_{NS}^{ν} ; Equation 14), and total NS kick ($v_{\text{NS}}^{\text{tot}}$; Equation 15) of model s9.0. Results for the kick velocities estimated on grounds of the total gas momentum ($v_{\text{NS}}^{\text{hyd,mc}}$ from Equation 16 and $v_{\text{NS}}^{\text{tot,mc}}$ from Equation 17) are also shown for comparison (dashed lines). *Top left*: Mass accretion rate in downflows at 400 km and baryonic and gravitational NS masses; *top right*: angle-averaged shock radius; *second row, left*: luminosities of ν_e , $\bar{\nu}_e$, and a single kind of ν_x , evaluated at 400 km, for a lab-frame observer at infinity; *second row, right*: hydrodynamic, neutrino-induced, and total NS kicks as labelled; *third row, left*: instantaneous neutrino-emission asymmetry parameters (solid) and their time-averaged values (dashed) for all neutrino species and the summed neutrino loss; *third row, right*: angles of $\mathbf{v}_{\text{NS}}^{\text{hyd}}$ and $\mathbf{v}_{\text{NS}}^{\nu}$ relative to $\mathbf{v}_{\text{NS}}^{\text{tot}}$; *bottom left*: time-integrated energy losses in ν_e , $\bar{\nu}_e$, all types of ν_x , and all summed up; *bottom right*: Relative angle between NS acceleration forces due to asymmetric gas ejection and due to total anisotropic neutrino emission, and angles between momentum force of ν_e and momentum forces of $\bar{\nu}_e$ and ν_x , respectively

z9.6 (LS220, 2°)

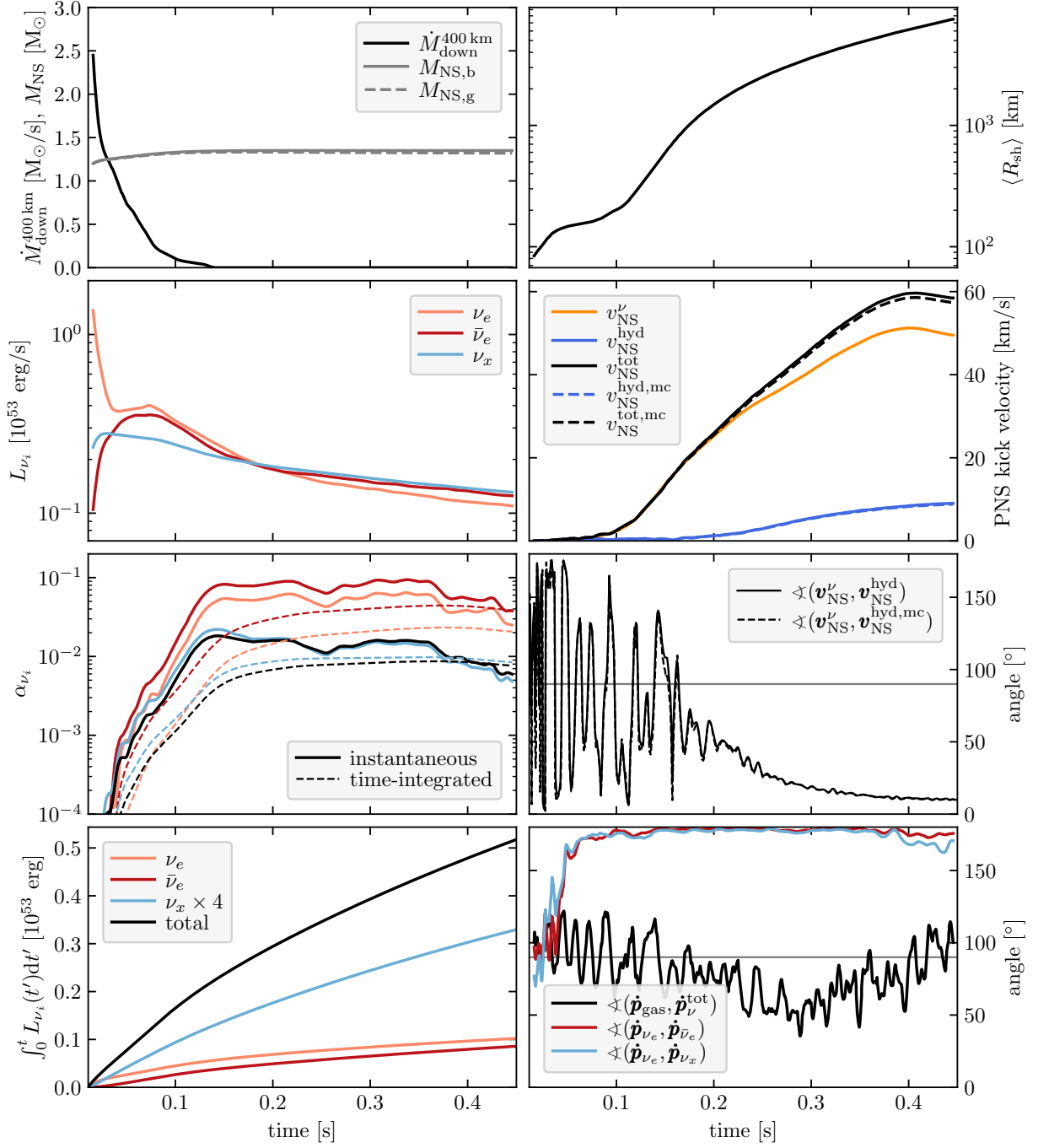


Fig. A2 Same as Figure A1, but for model z9.6

s12.28 (SFHo, 3.5°)

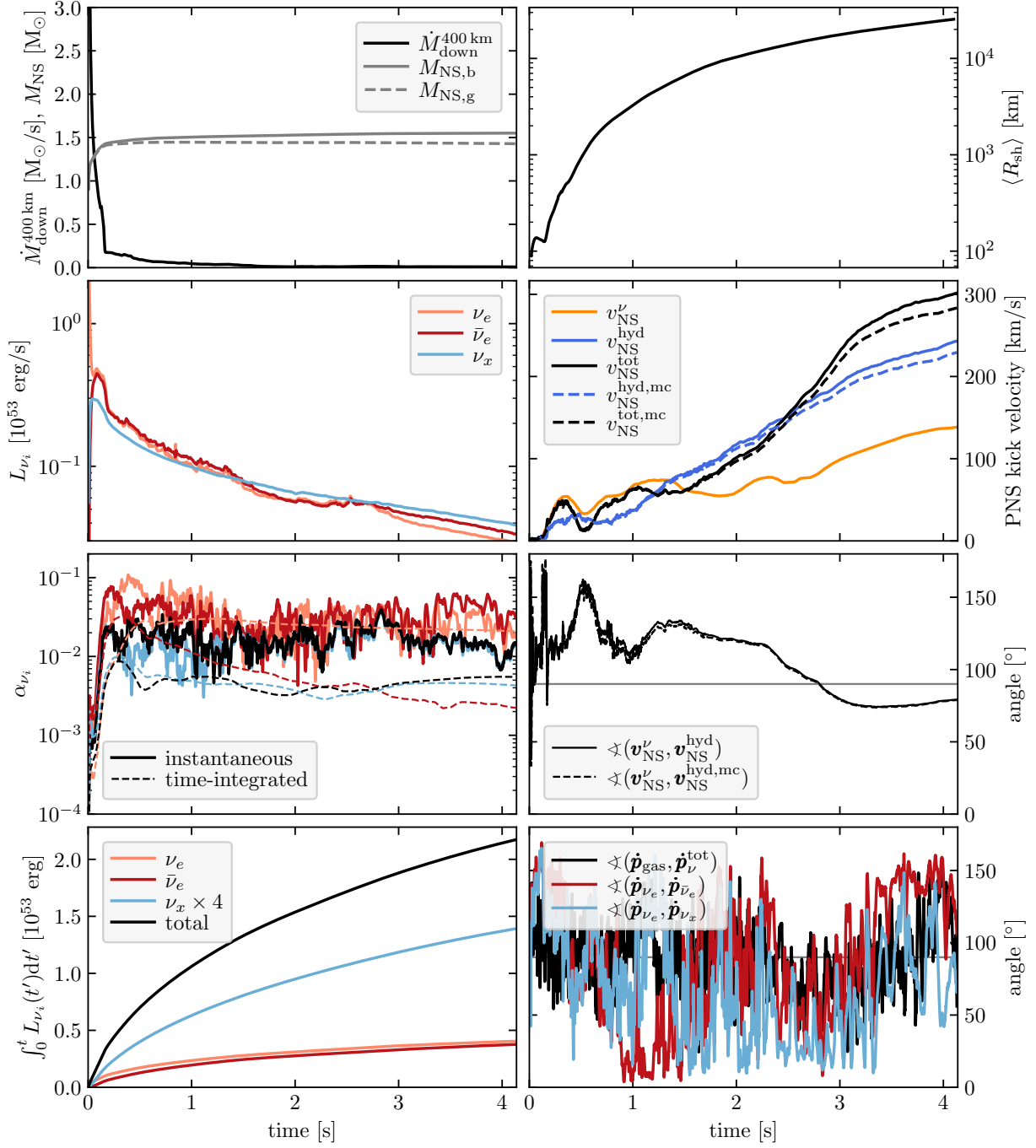


Fig. A3 Same as Figure A1, but for model s12.28

m15 (LS220, 2°)

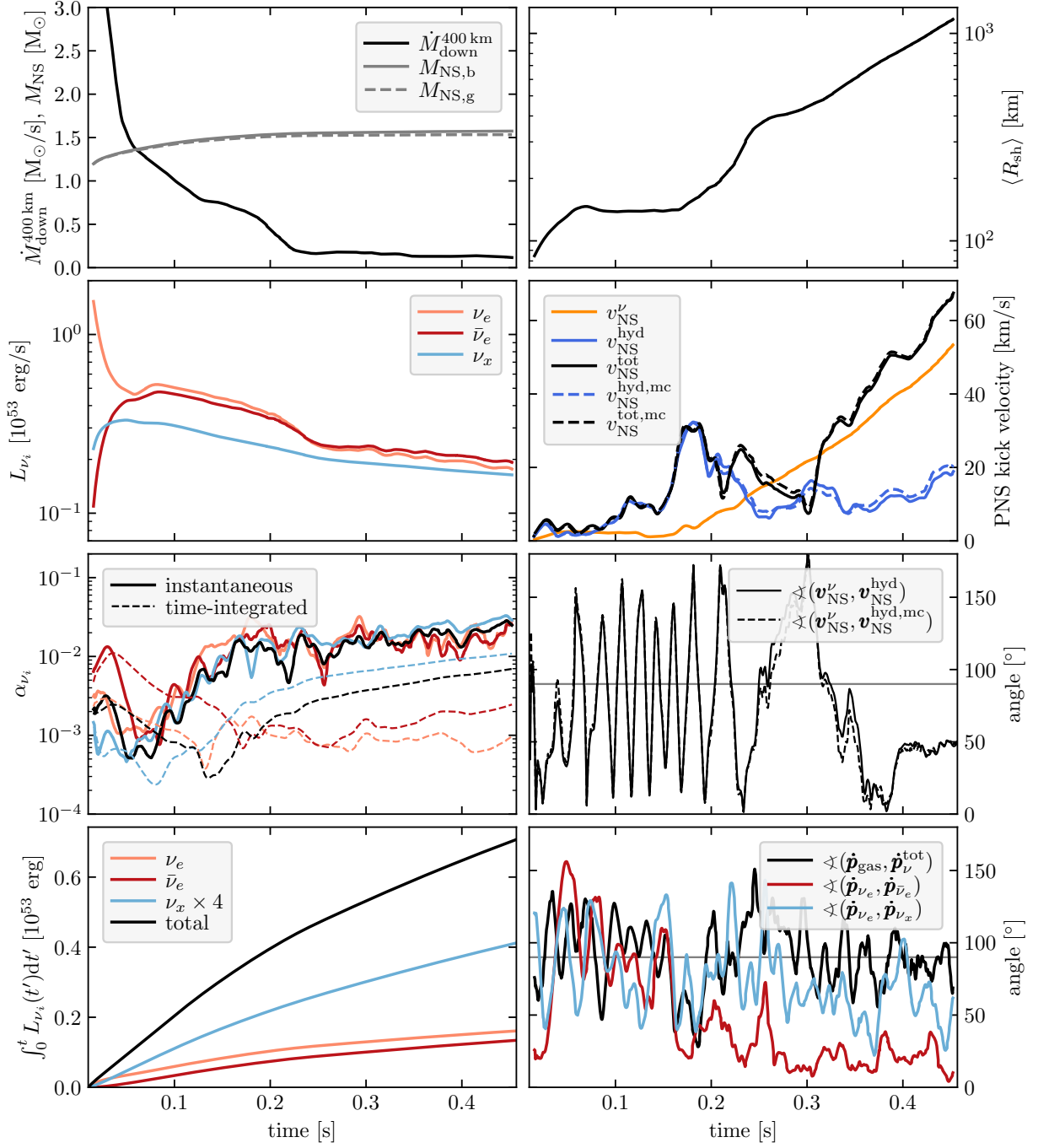


Fig. A4 Same as Figure A1, but for the rotating model m15

s18.88 (LS220, 2°)

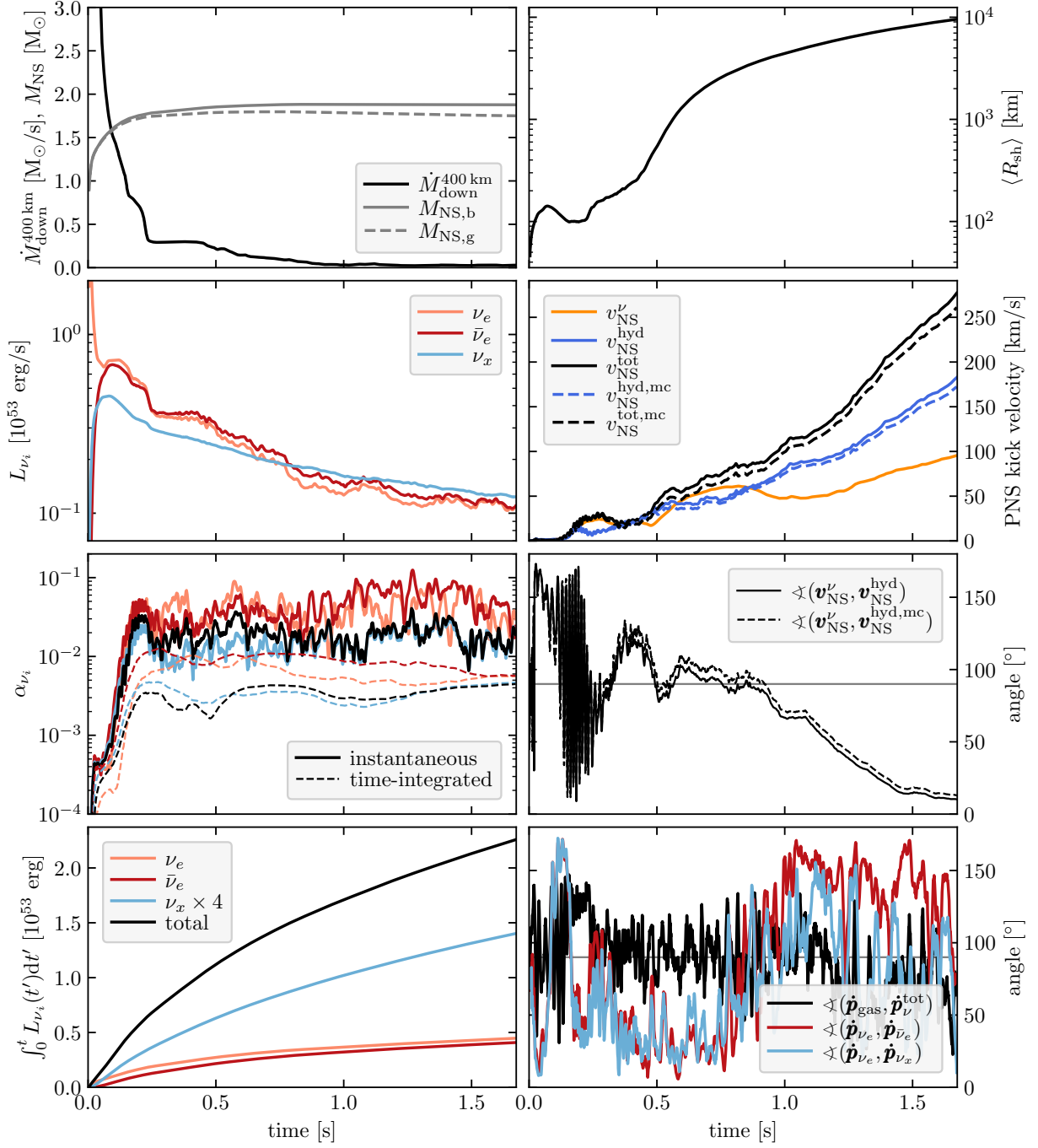


Fig. A5 Same as Figure A1, but for model s18.88

s20 (LS220, 2°)

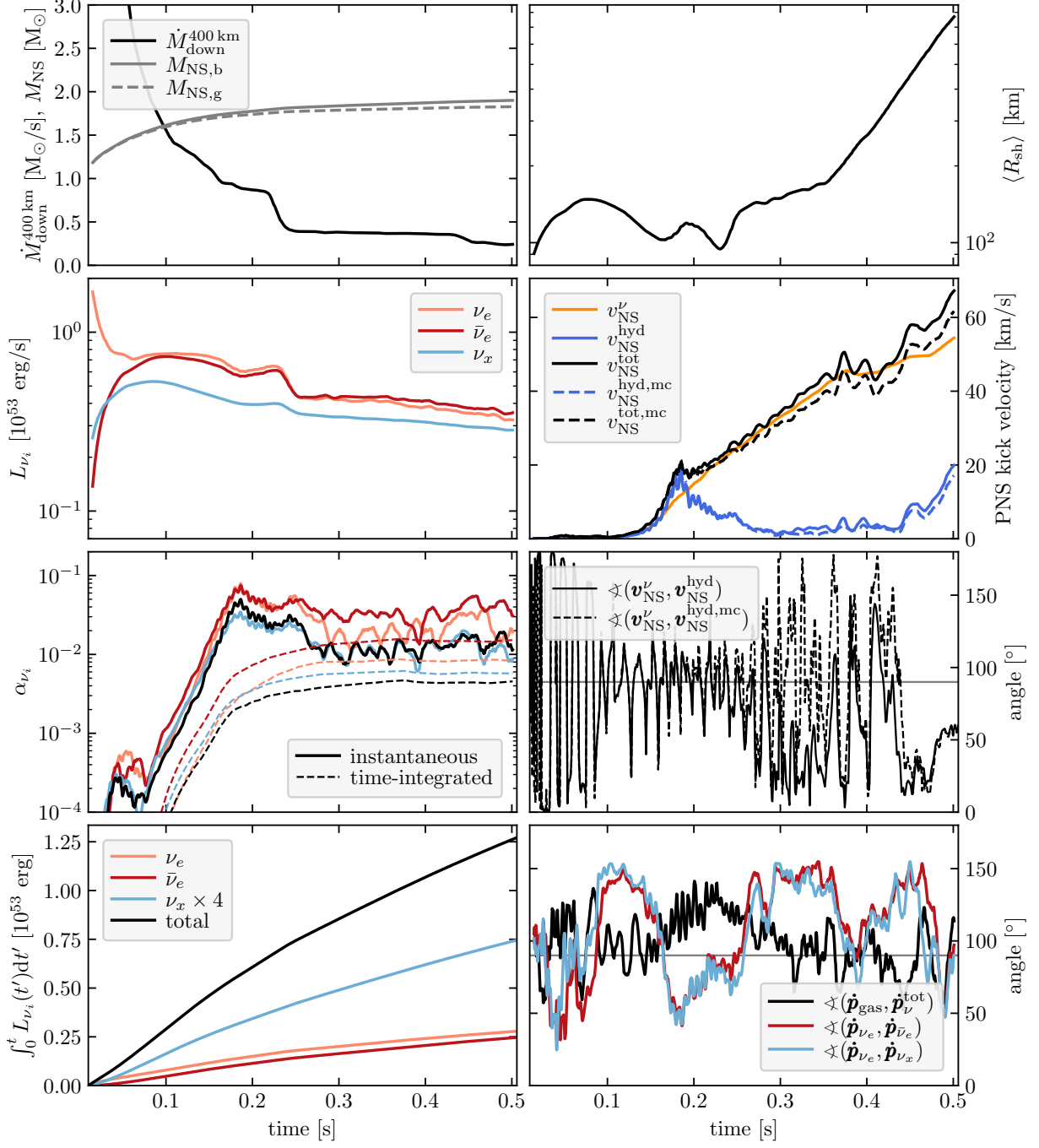


Fig. A6 Same as Figure A1, but for model s20

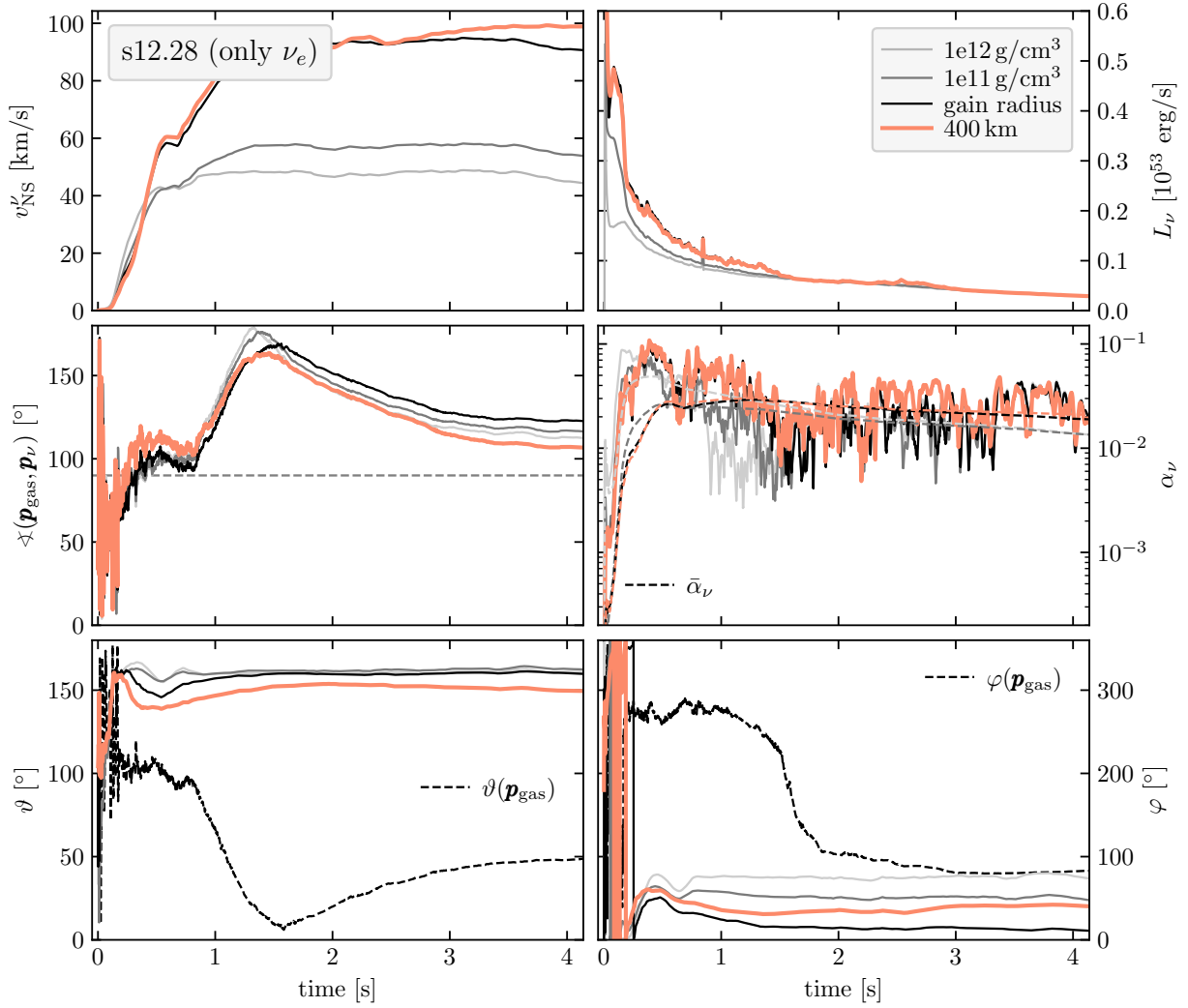


Fig. B7 Post-bounce evolution of the neutrino-induced NS kick caused by anisotropic emission of electron neutrinos ν_e in model s12.28. The displayed quantities are evaluated at radial locations for angle-averaged densities of $10^{12} \text{ g cm}^{-3}$ and $10^{11} \text{ g cm}^{-3}$, the angle-averaged gain radius, and at a radius of 400 km, where neutrinos have decoupled from the stellar plasma. *Top left*: NS kick velocity; *top right*: ν_e luminosity; *middle left*: relative angle between ν_e -kick of the NS and hydrodynamic NS kick; *middle right*: anisotropy parameter of the ν_e emission; *bottom left*: latitudinal angle of the ν_e momentum vector (solid lines) and the ejecta momentum vector (dashed line) in a global polar coordinate system of the simulation output; *bottom right*: azimuthal angle of the ν_e momentum vector (solid lines) and the ejecta momentum vector (dashed line) in a global polar coordinate system of the simulation output. Note that the vectors of the gas momentum and of the neutrino emission point in directions opposite to the corresponding NS kicks

times t'_i , when the PNSs become gravitationally unstable and our calculations with VERTEX neutrino transport were stopped.

It is important to keep in mind that the hydrodynamic kicks are only transient, because none of our BH forming models yields an explosion. Therefore the asymmetric gas around the PNSs constitutes only temporary ejecta, which ultimately fall back and are swallowed by the BHs.

Only the anisotropically radiated neutrinos are able to transfer a natal kick to the relic BHs. Our estimates of the neutrino-induced kicks for the final BHs are given in Table 3; the values listed there are calculated with the equation provided in the table notes, employing the PNS kick velocities obtained at the times when the PNSs collapse to BHs.

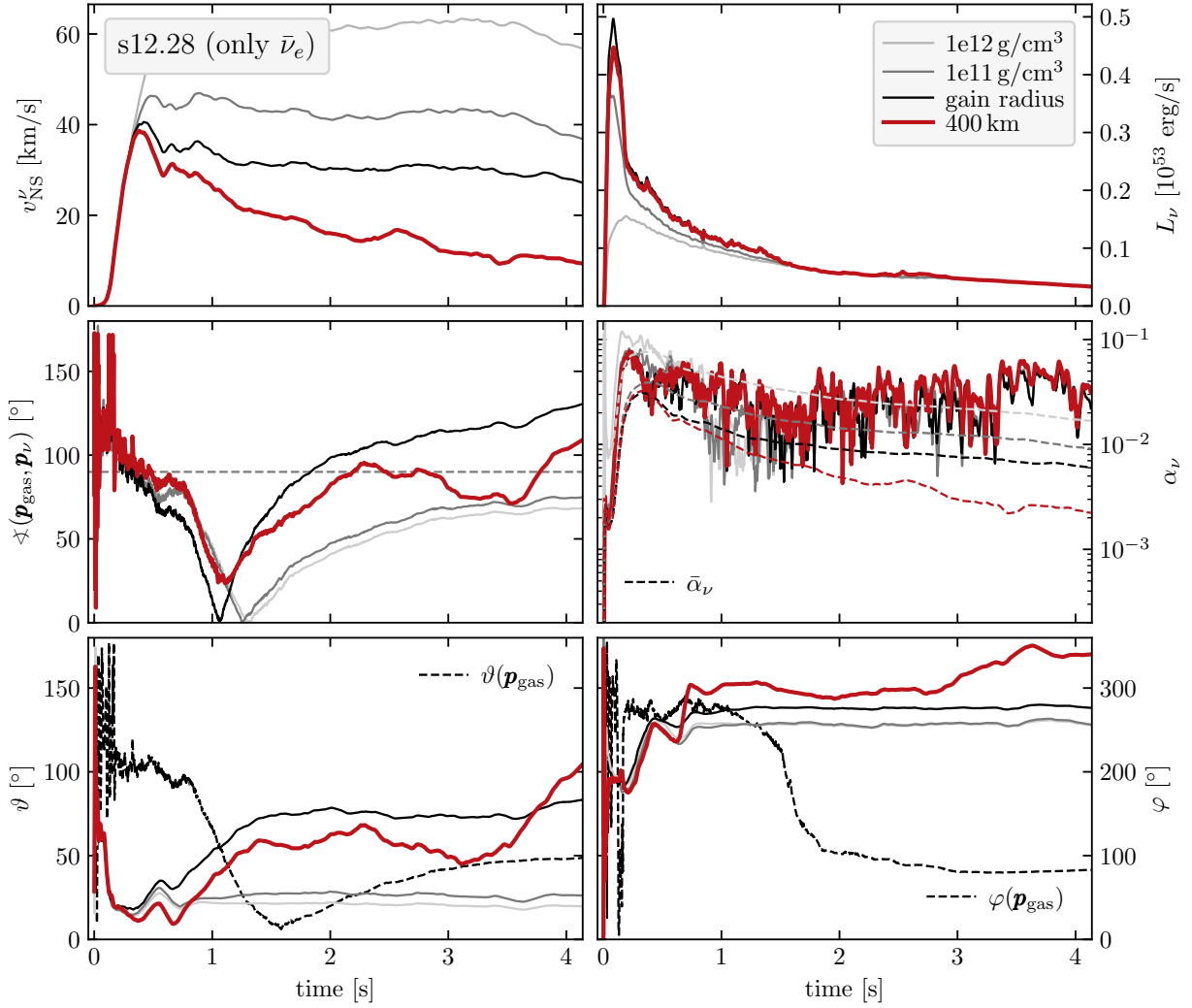


Fig. B8 Same as Figure B7, but for electron antineutrinos $\bar{\nu}_e$

We repeat that $\mathbf{v}_{\text{NS}}^{\text{hyd,mc}}$ and $\mathbf{v}_{\text{NS}}^{\text{tot,mc}}$ (computed via Equations 16 and 17) are approximate, lower bounds for $\mathbf{v}_{\text{NS}}^{\text{hyd}}$ and $\mathbf{v}_{\text{NS}}^{\text{tot}}$ (obtained from Equations 13 and 15), respectively. This fact can be disturbed by numerical inaccuracies of the kick evaluation in phases when the hydrodynamic accelerations and kick directions fluctuate wildly on short time scales because of rapid variations of non-spherical accretion flows. This mostly concerns model s40 and the late phase of model u75_DD2. In both cases the stalled shock retreats and describes violent SASI sloshing and spiral motions, which lead to large-amplitude non-radial variability in the postshock flows at very high frequencies. Discretized calculations of time

derivatives by finite differences are particularly prone to inaccuracies under such conditions.

Finally, we again remark that the displayed curves for all quantities, except the angles of $\mathbf{v}_{\text{NS}}^{\text{hyd}}$ and $\mathbf{v}_{\text{NS}}^{\text{hyd,mc}}$ relative to \mathbf{v}'_{NS} and the time-integrated neutrino energy losses, represent the computed results after smoothing by running means over time intervals of 10 ms. The same applies for all curves displayed in Figure 13. For this reason the first and last 5 ms of the simulated periods of evolution are not shown, which leads to small discrepancies between the plotted final values and the true final values listed in Table 3.

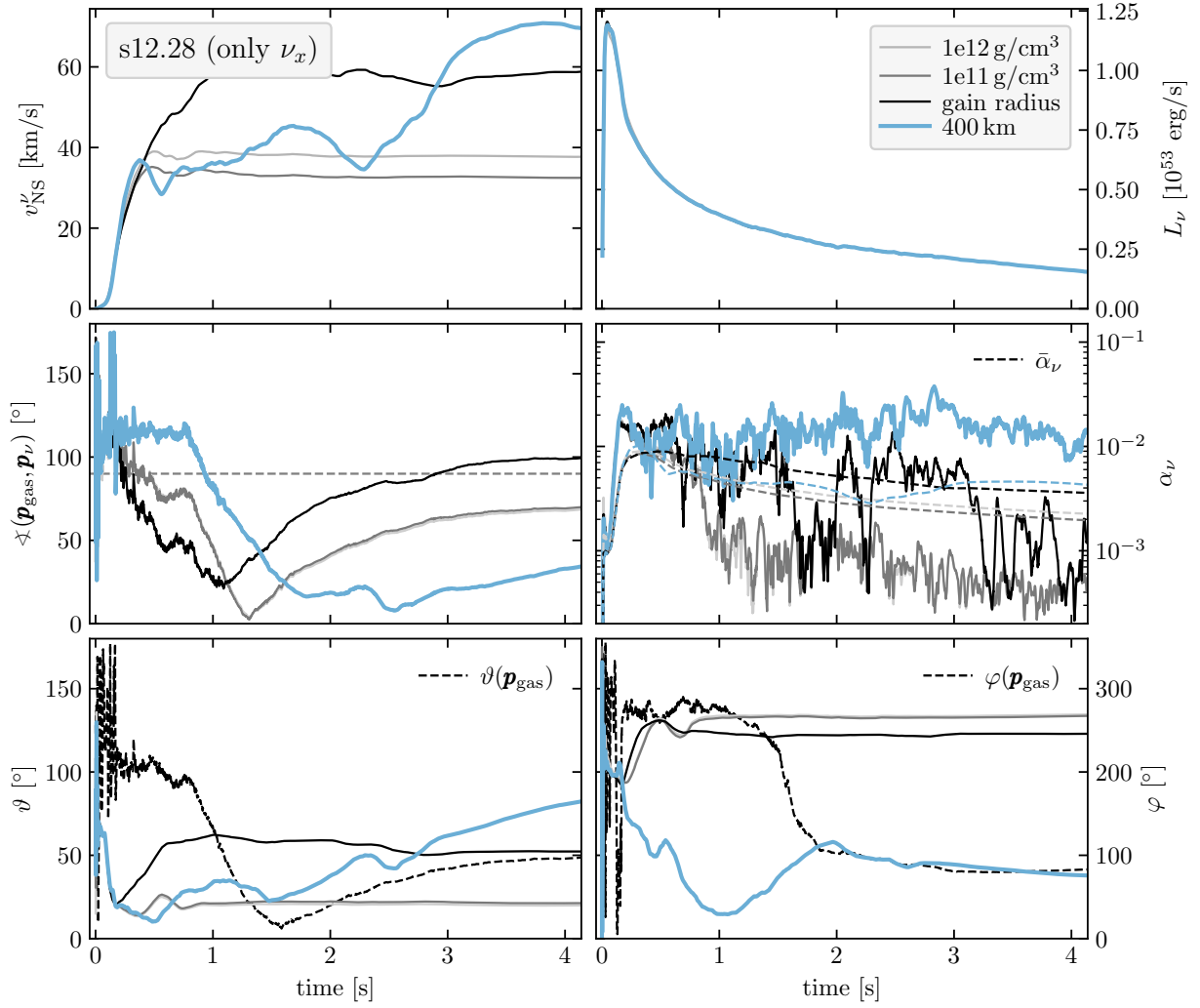


Fig. B9 Same as Figure B7, but for heavy-lepton neutrinos ν_x . The top panels show results summed up for all kinds of heavy-lepton neutrinos and antineutrinos

References

- Abbate F, Ridolfi A, Freire PCC, et al (2023) A MeerKAT view of the pulsars in the globular cluster NGC 6522. *Astron. Astrophys.* 680:A47. <https://doi.org/10.1051/0004-6361/202347725>, arXiv:2310.03800 [astro-ph.HE]
- Abbott BP, Abbott R, Abbott TD, et al (2017a) GW170817: Observation of Gravitational Waves from a Binary Neutron Star Inspiral. *Phys. Rev. Lett.* 119:161101. <https://doi.org/10.1103/PhysRevLett.119.161101>, arXiv:1710.05832 [gr-qc]
- Abbott BP, Abbott R, Abbott TD, et al (2017b) Gravitational Waves and Gamma-Rays from a Binary Neutron Star Merger: GW170817 and GRB 170817A. *Astrophys. J. Lett.* 848:L13. <https://doi.org/10.3847/2041-8213/aa920c>, arXiv:1710.05834 [astro-ph.HE]
- Andresen H, Glas R, Janka HT (2021) Gravitational-wave signals from 3D supernova simulations with different neutrino-transport methods. *Mon. Not. R. Astron. Soc.* 503:3552–3567. <https://doi.org/10.1093/mnras/stab675>, arXiv:2011.10499 [astro-ph.HE]
- Andrews JJ, Kalogera V (2022) Constraining

s40 (LS220, 5°)

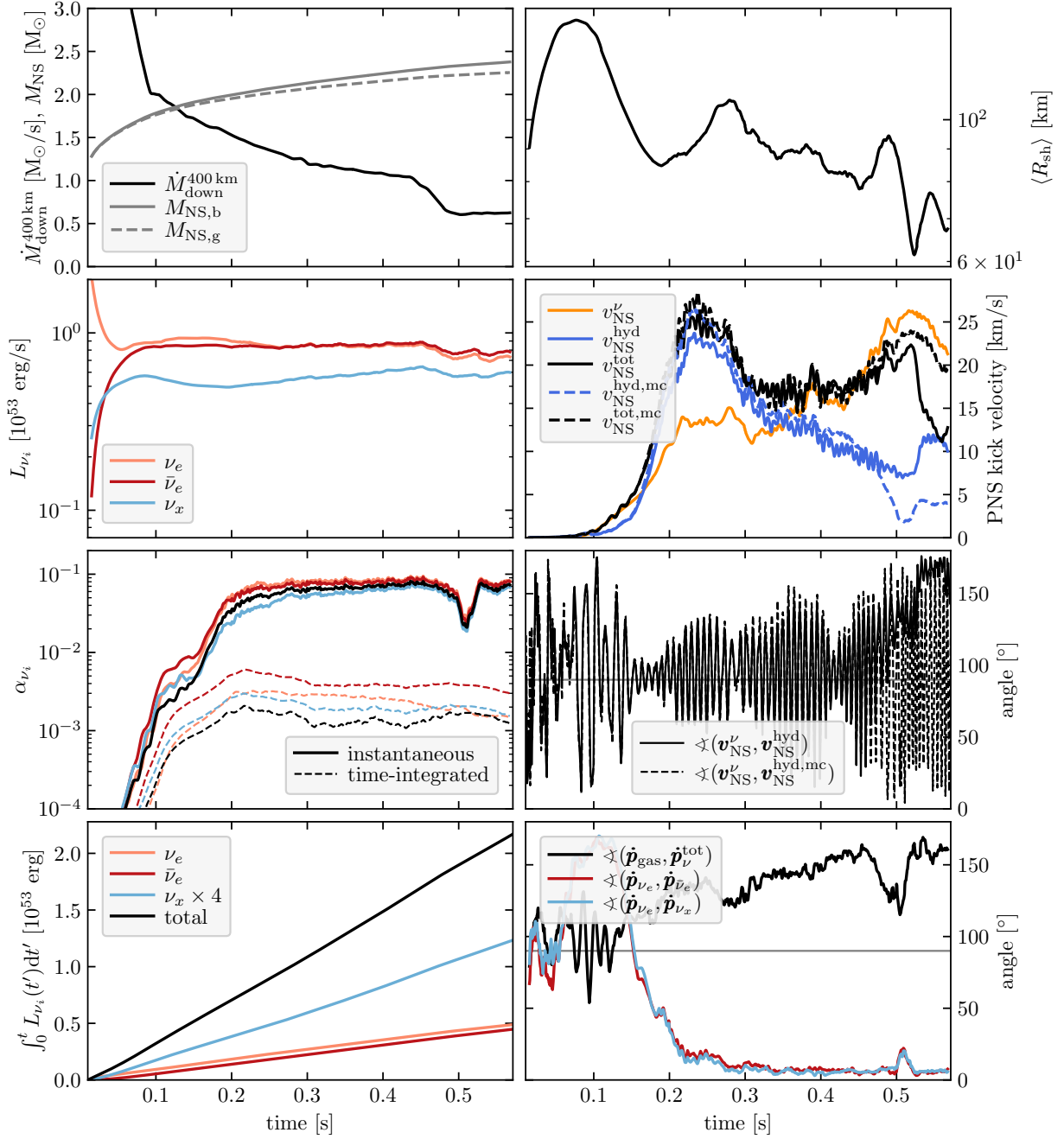


Fig. C10 Same as Figure A1, but for BH forming model s40

Black Hole Natal Kicks with Astrometric Microlensing. *Astrophys. J.* 930:159. <https://doi.org/10.3847/1538-4357/ac66d6>, [arXiv:2203.15156](https://arxiv.org/abs/2203.15156) [astro-ph.HE]

Arzoumanian Z, Chernoff DF, Cordes JM (2002) The Velocity Distribution of Isolated Radio Pulsars. *Astrophys. J.* 568:289–301. <https://doi.org/10.1086/338805>, [arXiv:astro-ph/0106159](https://arxiv.org/abs/astro-ph/0106159) [astro-ph]

u75 (DD2, 5°)

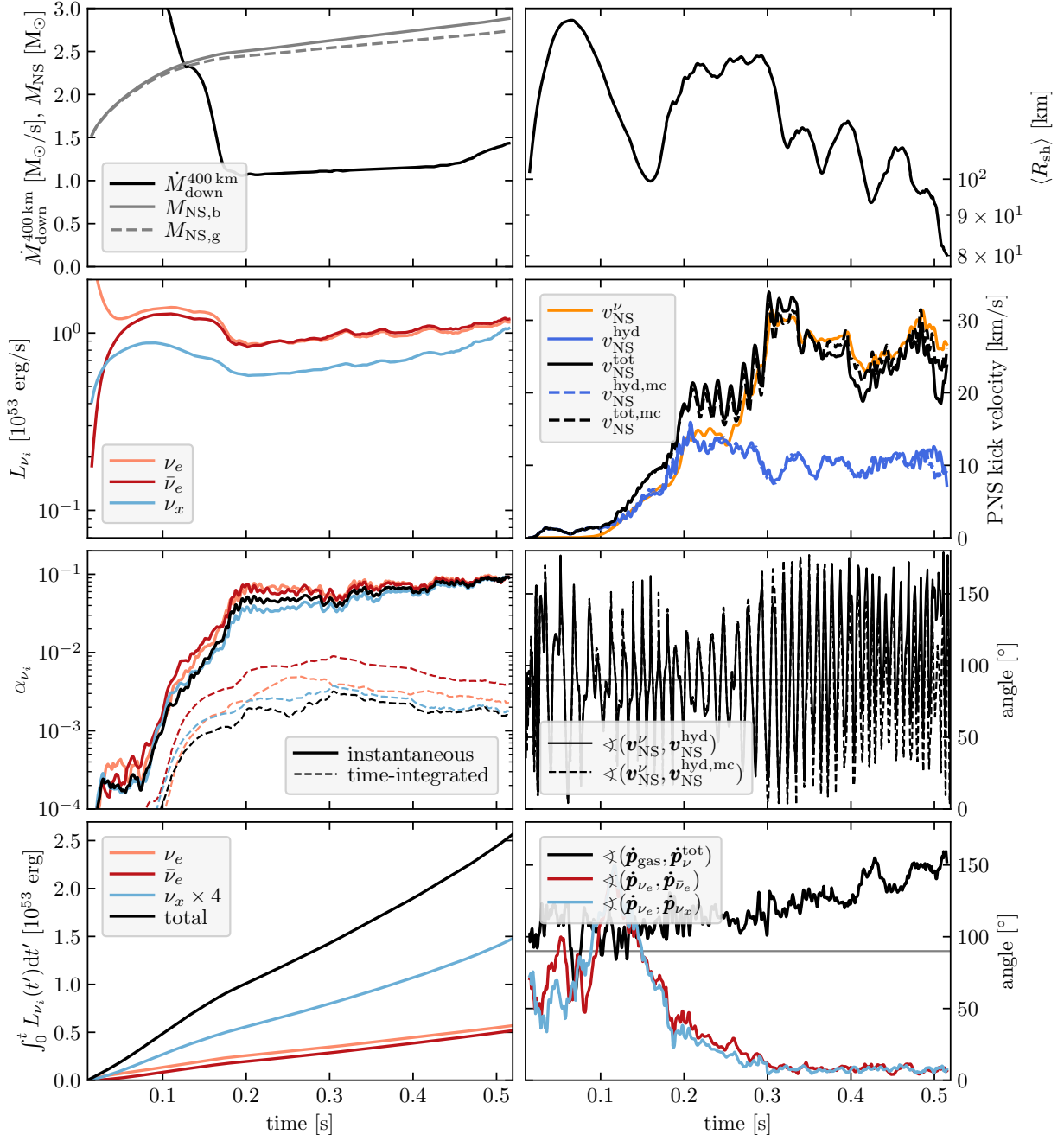


Fig. C11 Same as Figure A1, but for BH forming model u75_DD2

Atri P, Miller-Jones JCA, Bahramian A, et al (2019) Potential kick velocity distribution of black hole X-ray binaries and implications for natal kicks. Mon. Not. R. Astron. Soc. 489:3116–3134. <https://doi.org/10.1093/mnras/stz2335>

[arXiv:1908.07199](https://arxiv.org/abs/1908.07199) [astro-ph.HE]

Bahramian A, Degenaar N (2023) Low-Mass X-ray Binaries. In: Bambi C, Santangelo A (eds)

u75 (LS220, 5°)

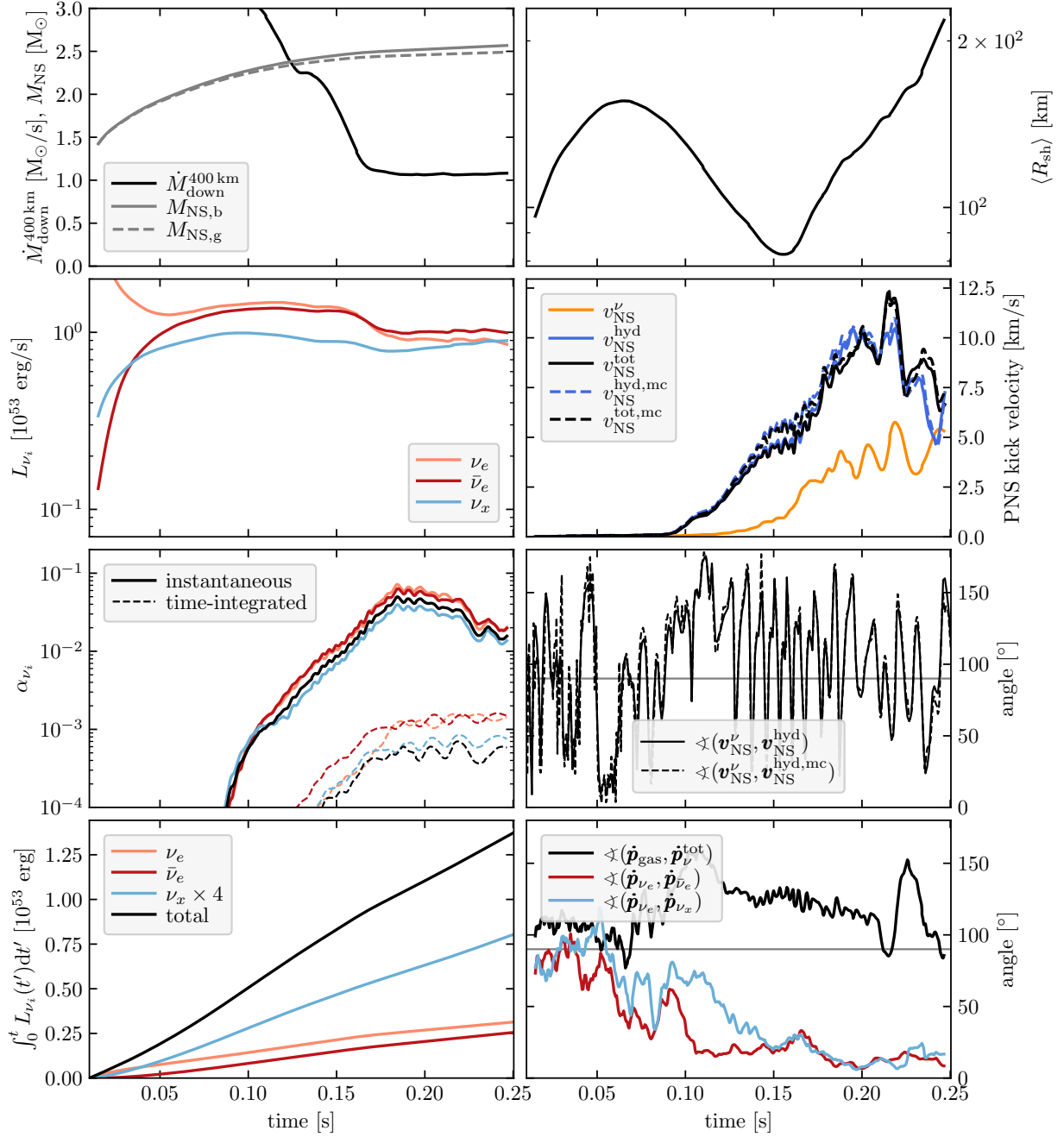


Fig. C12 Same as Figure A1, but for BH forming model u75-LS220_1

Handbook of X-ray and Gamma-ray Astrophysics. Springer, Singapore, p 120, <https://doi.org/10.1007/978-981-16-4544-0-94-1>

Blaauw A (1961) On the origin of the O- and B-type stars with high velocities (the “run-away” stars), and some related problems. Bulletin of the Astronomical Institutes of the Netherlands 15:265

u75 (LS220, 5°, v2)

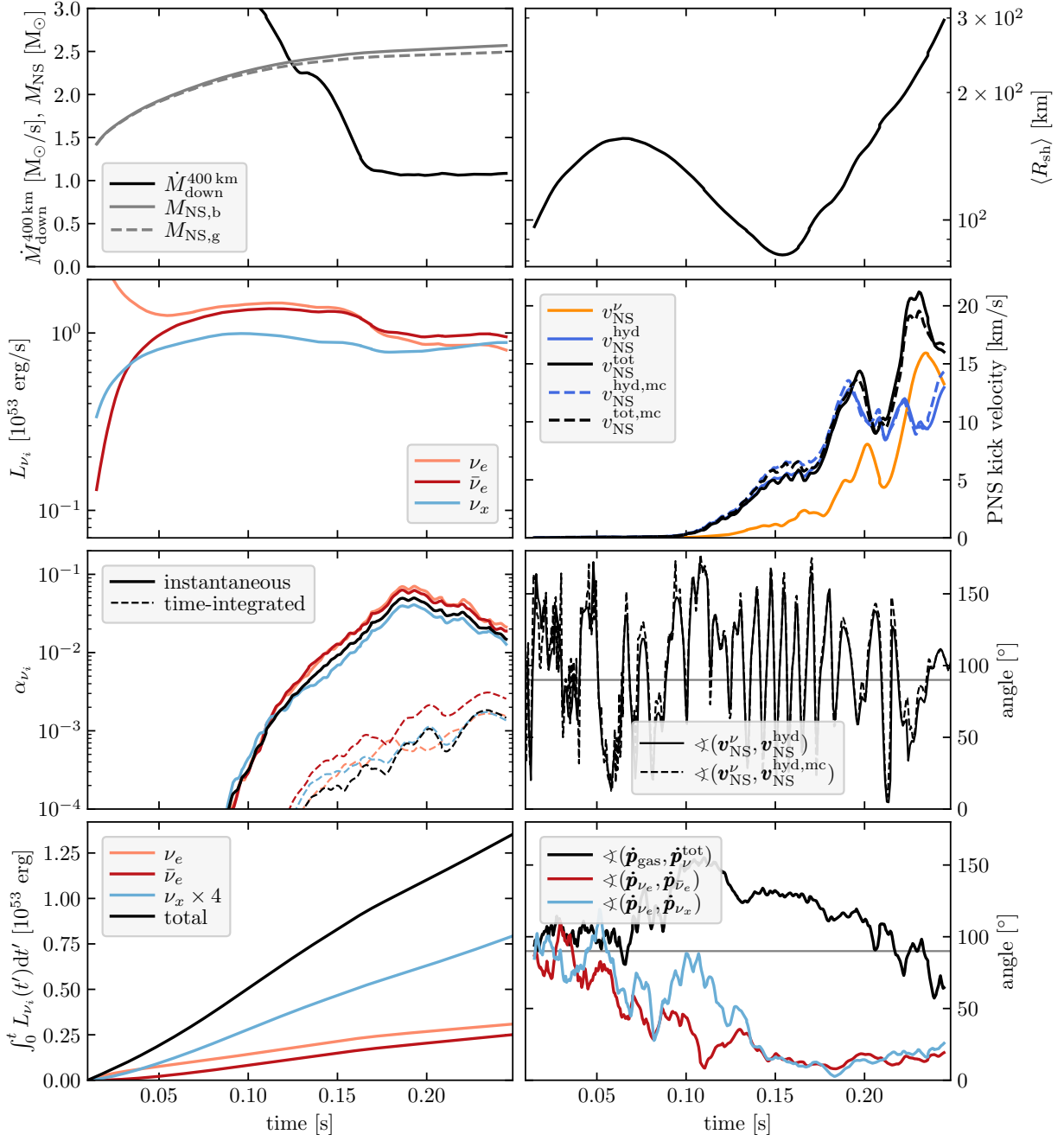


Fig. C13 Same as Figure A1, but for BH forming model u75.LS220-2

Blondin JM, Mezzacappa A (2007) Pulsar spins from an instability in the accretion shock of supernovae. *Nature* 445:58–60. <https://doi.org/10.1038/nature05428>, [arXiv:astro-ph/0611680](https://arxiv.org/abs/astro-ph/0611680) [astro-ph]

Blondin JM, Mezzacappa A, DeMarino C (2003) Stability of Standing Accretion Shocks, with an Eye toward Core-Collapse Supernovae. *Astrophys. J.* 584:971–980. <https://doi.org/10.1086/345812>, [arXiv:astro-ph/0210634](https://arxiv.org/abs/astro-ph/0210634) [astro-ph]

u75 (LS220, SMR)

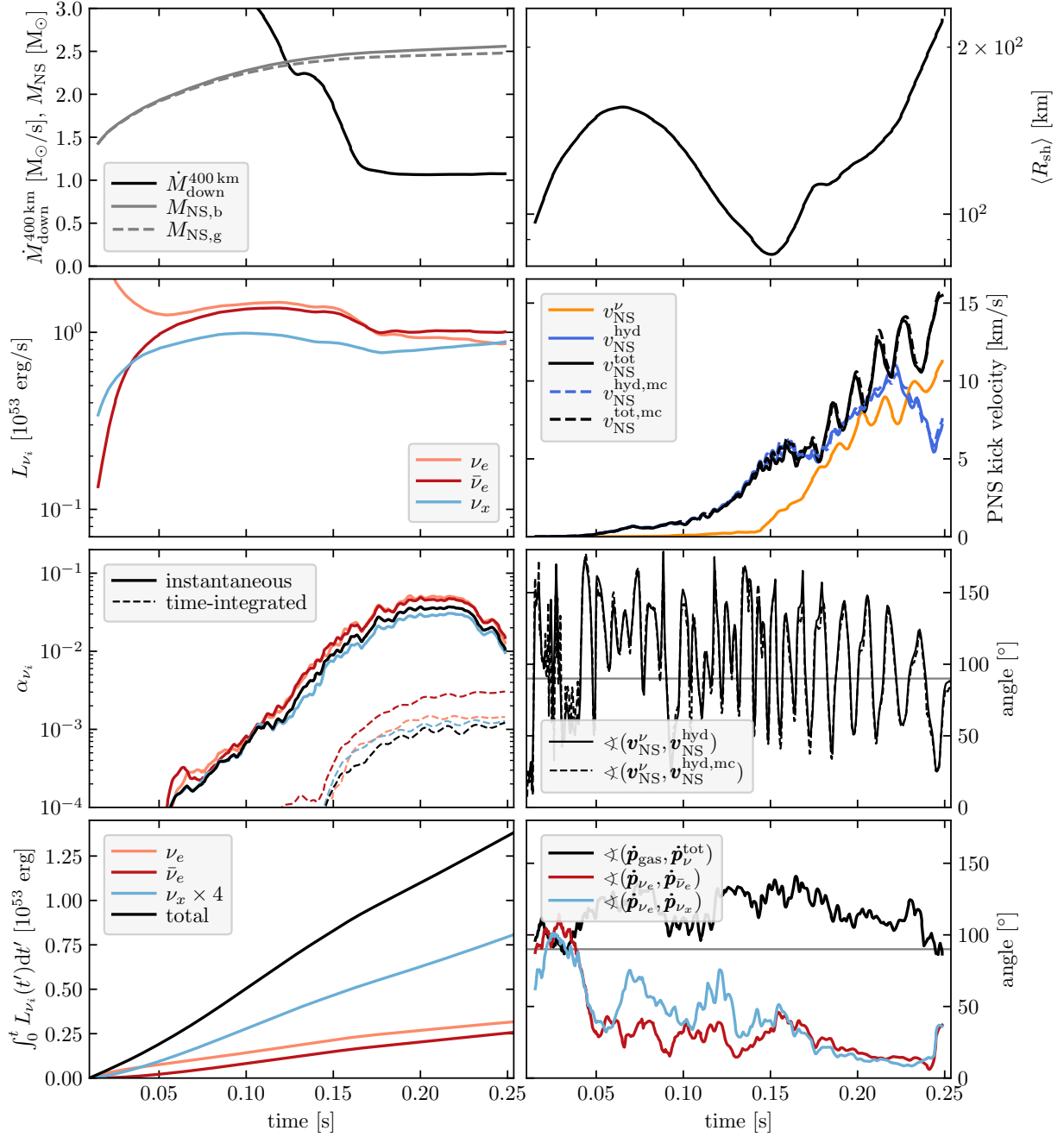


Fig. C14 Same as Figure A1, but for BH forming model u75-SMR-LS220-hr

Bollig R, Yadav N, Kresse D, et al (2021) Self-consistent 3D Supernova Models From -7 Minutes to +7 s: A 1-bethe Explosion of a 19 M_{\odot} Progenitor. *Astrophys. J.* 915:28. <https://doi.org/10.3847/1538-4357/>

abf82e, arXiv:2010.10506 [astro-ph.HE]

Buras R, Rampp M, Janka HT, et al (2006) Two-dimensional hydrodynamic core-collapse supernova simulations with spectral neutrino

u75 (SFHo, 5°)

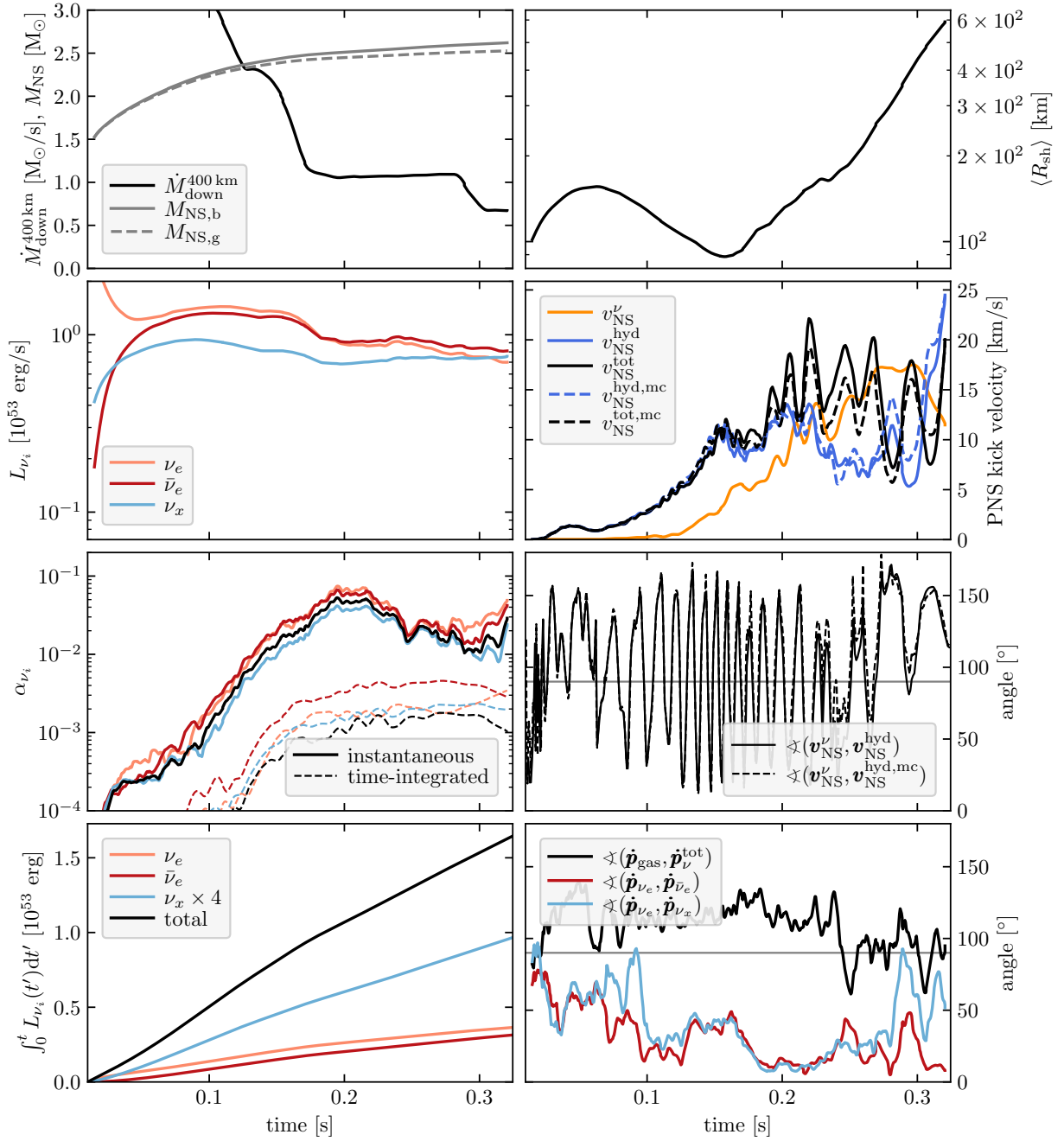


Fig. C15 Same as Figure A1, but for BH forming model u75_SFHo

transport. I. Numerical method and results for a 15 M_{\odot} star. *Astron. Astrophys.* 447:1049–1092. <https://doi.org/10.1051/0004-6361:20053783>, [arXiv:astro-ph/0507135](https://arxiv.org/abs/astro-ph/0507135) [astro-ph]

Burrows A, Hayes J (1996) Pulsar Recoil and Gravitational Radiation Due to Asymmetrical Stellar Collapse and Explosion. *Phys. Rev. Lett.* 76:352–355. <https://doi.org/10.1103/PhysRevLett.76.352>,

- arXiv:astro-ph/9511106 [astro-ph]
- Burrows A, Vartanyan D (2021) Core-collapse supernova explosion theory. *Nature* 589:29–39. <https://doi.org/10.1038/s41586-020-03059-w>, arXiv:2009.14157 [astro-ph.SR]
- Burrows A, Vartanyan D, Wang T (2023a) Black Hole Formation Accompanied by the Supernova Explosion of a 40 M_{\odot} Progenitor Star. *Astrophys. J.* 957:68. <https://doi.org/10.3847/1538-4357/acfc1c>, arXiv:2308.05798 [astro-ph.SR]
- Burrows A, Wang T, Vartanyan D, et al (2023b) A Comprehensive Theory for Neutron Star and Black Hole Kicks and Induced Spins. arXiv e-prints <https://doi.org/10.48550/arXiv.2311.12109>, arXiv:2311.12109 [astro-ph.HE]
- Chan C, Müller B, Heger A, et al (2018) Black Hole Formation and fallback during the Supernova Explosion of a 40 M_{\odot} Star. *Astrophys. J. Lett.* 852:L19. <https://doi.org/10.3847/2041-8213/aaa28c>, arXiv:1710.00838 [astro-ph.SR]
- Chan C, Müller B, Heger A (2020) The impact of fallback on the compact remnants and chemical yields of core-collapse supernovae. *Mon. Not. R. Astron. Soc.* 495:3751–3762. <https://doi.org/10.1093/mnras/staa1431>, arXiv:2003.04320 [astro-ph.SR]
- Chatterjee S, Vlemmings WHT, Briskeen WF, et al (2005) Getting Its Kicks: A VLBA Parallax for the Hyperfast Pulsar B1508+55. *Astrophys. J. Lett.* 630:L61–L64. <https://doi.org/10.1086/491701>, arXiv:astro-ph/0509031 [astro-ph]
- Coleman MSB, Burrows A (2022) Kicks and induced spins of neutron stars at birth. *Mon. Not. R. Astron. Soc.* 517:3938–3961. <https://doi.org/10.1093/mnras/stac2573>, arXiv:2209.02711 [astro-ph.HE]
- Dashwood Brown C, Gandhi P, Zhao Y (2024) On the natal kick of the black hole X-ray binary H 1705-250. *Mon. Not. R. Astron. Soc.* 527:L82–L87. <https://doi.org/10.1093/mnrasl/slad151>, arXiv:2310.11492 [astro-ph.HE]
- Fernández R (2010) The Spiral Modes of the Standing Accretion Shock Instability. *Astrophys. J.* 725:1563–1580. <https://doi.org/10.1088/0004-637X/725/2/1563>, arXiv:1003.1730 [astro-ph.SR]
- Fiorillo DFG, Heinlein M, Janka HT, et al (2023) Supernova simulations confront SN 1987A neutrinos. *Phys. Rev. D* 108:083040. <https://doi.org/10.1103/PhysRevD.108.083040>, arXiv:2308.01403 [astro-ph.HE]
- Foglizzo T, Galletti P, Scheck L, et al (2007) Instability of a Stalled Accretion Shock: Evidence for the Advective-Acoustic Cycle. *Astrophys. J.* 654:1006–1021. <https://doi.org/10.1086/509612>, arXiv:astro-ph/0606640 [astro-ph]
- Fryer CL, Kusenko A (2006) Effects of Neutrino-driven Kicks on the Supernova Explosion Mechanism. *Astrophys. J. Suppl. Ser.* 163:335–343. <https://doi.org/10.1086/500933>, arXiv:astro-ph/0512033 [astro-ph]
- Fryer CL, Belczynski K, Wiktorowicz G, et al (2012) Compact Remnant Mass Function: Dependence on the Explosion Mechanism and Metallicity. *Astrophys. J.* 749:91. <https://doi.org/10.1088/0004-637X/749/1/91>, arXiv:1110.1726 [astro-ph.SR]
- Fryxell B, Müller E, Arnett D (1989) Computation of multi-dimensional flows with non-uniform composition. In: Hillebrandt W, Müller E (eds) *Proceedings of the 5th Workshop on Nuclear Astrophysics*. Max Planck Institute for Astrophysics, Garching, Germany, p 100
- Gaspari N, Levan AJ, Chrimes AA, et al (2024) The Galactic neutron star population - II. Systemic velocities and merger locations of binary neutron stars. *Mon. Not. R. Astron. Soc.* 527:1101–1113. <https://doi.org/10.1093/mnras/stad3259>, arXiv:2310.14773 [astro-ph.HE]
- Gessner A, Janka HT (2018) Hydrodynamical Neutron-star Kicks in Electron-capture Supernovae and Implications for the CRAB Supernova. *Astrophys. J.* 865:61. <https://doi.org/10.3847/1538-4357/aadbae>,

- [arXiv:1802.05274](https://arxiv.org/abs/1802.05274) [astro-ph.HE]
- Glas R, Janka HT, Melson T, et al (2019a) Effects of LESA in Three-dimensional Supernova Simulations with Multidimensional and Ray-by-ray-plus Neutrino Transport. *Astrophys. J.* 881:36. <https://doi.org/10.3847/1538-4357/ab275c>, [arXiv:1809.10150](https://arxiv.org/abs/1809.10150) [astro-ph.HE]
- Glas R, Just O, Janka HT, et al (2019b) Three-dimensional Core-collapse Supernova Simulations with Multidimensional Neutrino Transport Compared to the Ray-by-ray-plus Approximation. *Astrophys. J.* 873:45. <https://doi.org/10.3847/1538-4357/ab0423>, [arXiv:1809.10146](https://arxiv.org/abs/1809.10146) [astro-ph.HE]
- Grefenstette BW, Harrison FA, Boggs SE, et al (2014) Asymmetries in core-collapse supernovae from maps of radioactive ^{44}Ti in Cassiopeia A. *Nature* 506:339–342. <https://doi.org/10.1038/nature12997>, [arXiv:1403.4978](https://arxiv.org/abs/1403.4978) [astro-ph.HE]
- Grefenstette BW, Fryer CL, Harrison FA, et al (2017) The Distribution of Radioactive ^{44}Ti in Cassiopeia A. *Astrophys. J.* 834:19. <https://doi.org/10.3847/1538-4357/834/1/19>, [arXiv:1612.02774](https://arxiv.org/abs/1612.02774) [astro-ph.HE]
- Heger A (2012) Private communication
- Heger A, Woosley SE, Spruit HC (2005) Pre-supernova Evolution of Differentially Rotating Massive Stars Including Magnetic Fields. *Astrophys. J.* 626:350–363. <https://doi.org/10.1086/429868>, [astro-ph/0409422](https://arxiv.org/abs/astro-ph/0409422)
- Hempel M, Schaffner-Bielich J (2010) A statistical model for a complete supernova equation of state. *Nuclear Physics A* 837:210–254. <https://doi.org/10.1016/j.nuclphysa.2010.02.010>, [arXiv:0911.4073](https://arxiv.org/abs/0911.4073) [nucl-th]
- Hester JJ (2008) The Crab Nebula : an astrophysical chimera. *Ann Rev Astron Astrophys* 46:127–155. <https://doi.org/10.1146/annurev.astro.45.051806.110608>
- Heywood I (2023) A new pulsar candidate in 47 Tucanae discovered with MeerKAT imaging. *Mon. Not. R. Astron. Soc.* 525:L76–L81. <https://doi.org/10.1093/mnrasl/slado94>, [arXiv:2307.02077](https://arxiv.org/abs/2307.02077) [astro-ph.HE]
- Hobbs G, Lorimer DR, Lyne AG, et al (2005) A statistical study of 233 pulsar proper motions. *Mon. Not. R. Astron. Soc.* 360:974–992. <https://doi.org/10.1111/j.1365-2966.2005.09087.x>, [arXiv:astro-ph/0504584](https://arxiv.org/abs/astro-ph/0504584) [astro-ph]
- Holland-Ashford T, Lopez LA, Auchettl K, et al (2017) Comparing Neutron Star Kicks to Supernova Remnant Asymmetries. *Astrophys. J.* 844:84. <https://doi.org/10.3847/1538-4357/aa7a5c>, [arXiv:1705.08454](https://arxiv.org/abs/1705.08454) [astro-ph.HE]
- Holland-Ashford T, Slane P, Long X (2023) Updated Proper Motion of the Neutron Star in the Supernova Remnant Cassiopeia A. *arXiv e-prints* <https://doi.org/10.48550/arXiv.2310.19879>, [arXiv:2310.19879](https://arxiv.org/abs/2310.19879) [astro-ph.HE]
- Ivanova N, Heinke CO, Rasio FA, et al (2008) Formation and evolution of compact binaries in globular clusters - II. Binaries with neutron stars. *Mon. Not. R. Astron. Soc.* 386:553–576. <https://doi.org/10.1111/j.1365-2966.2008.13064.x>, [arXiv:0706.4096](https://arxiv.org/abs/0706.4096) [astro-ph]
- Iwakami W, Ohnishi N, Kotake K, et al (2009) Spiral mode of standing accretion shock instability in core-collapse supernovae. *Astrophys. Space Sci.* 322:43–47. <https://doi.org/10.1007/s10509-008-9957-6>
- Janka HT (2004) Neutron Star Formation and Birth Properties. In: Camilo F, Gaensler BM (eds) *Young Neutron Stars and Their Environments*, vol 218. *Astronomical Society of the Pacific*, San Francisco, CA, p 3, <https://doi.org/10.48550/arXiv.astro-ph/0402200>, [astro-ph/0402200](https://arxiv.org/abs/astro-ph/0402200)
- Janka HT (2013) Natal kicks of stellar mass black holes by asymmetric mass ejection in fallback supernovae. *Mon. Not. R. Astron. Soc.* 434:1355–1361. <https://doi.org/10.1093/mnras/stt1106>, [arXiv:1306.0007](https://arxiv.org/abs/1306.0007) [astro-ph.SR]
- Janka HT (2017) Neutron Star Kicks by the Gravitational Tug-boat Mechanism in Asymmetric Supernova Explosions: Progenitor and Explosion Dependence. *Astrophys. J.* 837:84. <https://doi.org/10.3847/1538-4357/1705.08454>

- aa618e, [arXiv:1611.07562](https://arxiv.org/abs/1611.07562) [astro-ph.HE]
- Janka HT, Müller E (1994) Neutron star recoils from anisotropic supernovae. *Astron. Astrophys.* 290:496–502
- Janka HT, Wongwathanarat A, Kramer M (2022) Supernova fallback as origin of neutron star spins and spin-kick alignment. *Astrophys. J.* 926:9. <https://doi.org/10.3847/1538-4357/ac403c>, [arXiv:2104.07493](https://arxiv.org/abs/2104.07493) [astro-ph.HE]
- Kaplan DL, Chatterjee S, Gaensler BM, et al (2008) A precise proper motion for the Crab pulsar, and the difficulty of testing spin-kick alignment for young neutron stars. *Astrophys. J.* 677:1201–1215. <https://doi.org/10.1086/529026>, [arXiv:0801.1142](https://arxiv.org/abs/0801.1142) [astro-ph]
- Kasen D, Woosley SE (2009) Type II supernovae: model light curves and standard candle relationships. *Astrophys. J.* 703:2205–2216. <https://doi.org/10.1088/0004-637X/703/2/2205>, [arXiv:0910.1590](https://arxiv.org/abs/0910.1590) [astro-ph.CO]
- Katsuda S, Morii M, Janka HT, et al (2018) Intermediate-mass elements in young supernova remnants reveal neutron star kicks by asymmetric explosions. *Astrophys. J.* 856:18. <https://doi.org/10.3847/1538-4357/aab092>, [arXiv:1710.10372](https://arxiv.org/abs/1710.10372) [astro-ph.HE]
- Kazeroni R, Guilet J, Foglizzo T (2016) New insights on the spin-up of a neutron star during core collapse. *Mon. Not. R. Astron. Soc.* 456:126–135. <https://doi.org/10.1093/mnras/stv2666>, [arXiv:1509.02828](https://arxiv.org/abs/1509.02828) [astro-ph.HE]
- Kazeroni R, Guilet J, Foglizzo T (2017) Are pulsars spun up or down by SASI spiral modes? *Mon. Not. R. Astron. Soc.* 471:914–925. <https://doi.org/10.1093/mnras/stx1566>, [arXiv:1701.07029](https://arxiv.org/abs/1701.07029) [astro-ph.HE]
- Keil W (1997) Konvektive instabilitäten in entstehenden neutronensternen. PhD thesis, Technische Universität München
- Kifonidis K, Plewa T, Janka HT, et al (2003) Non-spherical core collapse supernovae. I. Neutrino-driven convection, Rayleigh-Taylor instabilities, and the formation and propagation of metal clumps. *Astron. Astrophys.* 408:621–649. <https://doi.org/10.1051/0004-6361:20030863>, [arXiv:astro-ph/0302239](https://arxiv.org/abs/astro-ph/0302239) [astro-ph]
- Kim V, Izmailova I, Aimuratov Y (2023) Catalog of the Galactic Population of X-Ray Pulsars in High-mass X-Ray Binary Systems. *Astrophys. J. Suppl. Ser.* 268:21. <https://doi.org/10.3847/1538-4365/ace68f>, [arXiv:2308.09295](https://arxiv.org/abs/2308.09295) [astro-ph.HE]
- Kimball C, Imperato S, Kalogera V, et al (2023) A black hole kicked at birth: MAXI J1305-704. *Astrophys. J. Lett.* 952:L34. <https://doi.org/10.3847/2041-8213/ace526>, [arXiv:2211.02158](https://arxiv.org/abs/2211.02158) [astro-ph.HE]
- Kresse D (2023) Towards energy saturation in three-dimensional simulations of core-collapse supernova explosions. PhD thesis, Technical University of Munich
- Kresse D, Ertl T, Janka HT (2021) Stellar collapse diversity and the diffuse supernova neutrino background. *Astrophys. J.* 909:169. <https://doi.org/10.3847/1538-4357/abd54e>, [arXiv:2010.04728](https://arxiv.org/abs/2010.04728) [astro-ph.HE]
- Kuroda T, Kotake K, Takiwaki T, et al (2018) A full general relativistic neutrino radiation-hydrodynamics simulation of a collapsing very massive star and the formation of a black hole. *Mon. Not. R. Astron. Soc.* 477:L80–L84. <https://doi.org/10.1093/mnras/sly059>, [arXiv:1801.01293](https://arxiv.org/abs/1801.01293) [astro-ph.HE]
- Lai D, Chernoff DF, Cordes JM (2001) Pulsar jets: implications for neutron star kicks and initial spins. *Astrophys. J.* 549:1111–1118. <https://doi.org/10.1086/319455>, [arXiv:astro-ph/0007272](https://arxiv.org/abs/astro-ph/0007272) [astro-ph]
- Lattimer JM, Swesty DF (1991) A generalized equation of state for hot, dense matter. *Nuclear Physics A* 535:331–376. [https://doi.org/10.1016/0375-9474\(91\)90452-C](https://doi.org/10.1016/0375-9474(91)90452-C)
- Lovegrove E, Woosley SE (2013) Very low energy supernovae from neutrino mass loss. *Astrophys. J.* 769:109. <https://doi.org/10.1088/>

- 0004-637X/769/2/109, arXiv:1303.5055 [astro-ph.HE]
- Mandel I (2016) Estimates of black hole natal kick velocities from observations of low-mass X-ray binaries. *Mon. Not. R. Astron. Soc.* 456:578–581. <https://doi.org/10.1093/mnras/stv2733>, arXiv:1510.03871 [astro-ph.HE]
- Mandel I, Müller B (2020) Simple recipes for compact remnant masses and natal kicks. *Mon. Not. R. Astron. Soc.* 499:3214–3221. <https://doi.org/10.1093/mnras/staa3043>, arXiv:2006.08360 [astro-ph.HE]
- Mandel I, Müller B, Riley J, et al (2021) Binary population synthesis with probabilistic remnant mass and kick prescriptions. *Mon. Not. R. Astron. Soc.* 500:1380–1384. <https://doi.org/10.1093/mnras/staa3390>, arXiv:2007.03890 [astro-ph.HE]
- Marek A, Dimmelmeier H, Janka HT, et al (2006) Exploring the relativistic regime with Newtonian hydrodynamics: an improved effective gravitational potential for supernova simulations. *Astron. Astrophys.* 445:273–289. <https://doi.org/10.1051/0004-6361:20052840>, arXiv:astro-ph/0502161 [astro-ph]
- Martinez L, Bersten MC, Anderson JP, et al (2022) Type II supernovae from the Carnegie Supernova Project-I. II. Physical parameter distributions from hydrodynamical modelling. *Astron. Astrophys.* 660:A41. <https://doi.org/10.1051/0004-6361/202142076>, arXiv:2111.06529 [astro-ph.SR]
- Mayer M, Becker W, Patnaude D, et al (2020) The Proper Motion of the Central Compact Object RX J0822-4300 in the Supernova Remnant Puppis A, Revisited. *Astrophys. J.* 899:138. <https://doi.org/10.3847/1538-4357/aba121>, arXiv:2005.09457 [astro-ph.HE]
- Melson T, Janka HT, Bollig R, et al (2015a) Neutrino-driven Explosion of a 20 Solar-mass Star in Three Dimensions Enabled by Strange-quark Contributions to Neutrino-Nucleon Scattering. *Astrophys. J. Lett.* 808:L42. <https://doi.org/10.1088/2041-8205/808/2/L42>, arXiv:1504.07631 [astro-ph.SR]
- Melson T, Janka HT, Marek A (2015b) Neutrino-driven Supernova of a Low-mass Iron-core Progenitor Boosted by Three-dimensional Turbulent Convection. *Astrophys. J. Lett.* 801:L24. <https://doi.org/10.1088/2041-8205/801/2/L24>, arXiv:1501.01961 [astro-ph.SR]
- Melson T, Kresse D, Janka HT (2020) Resolution Study for Three-dimensional Supernova Simulations with the Prometheus-Vertex Code. *Astrophys. J.* 891:27. <https://doi.org/10.3847/1538-4357/ab72a7>, arXiv:1904.01699 [astro-ph.HE]
- Mezzacappa A, Marronetti P, Landfield RE, et al (2023) Core collapse supernova gravitational wave emission for progenitors of 9.6, 15, and 25 M_{\odot} . *Phys. Rev. D* 107:043008. <https://doi.org/10.1103/PhysRevD.107.043008>, arXiv:2208.10643 [astro-ph.SR]
- Müller B (2023) Fallback onto kicked neutron stars and its effect on spin-kick alignment. *Mon. Not. R. Astron. Soc.* 526:2880–2888. <https://doi.org/10.1093/mnras/stad2881>, arXiv:2308.08312 [astro-ph.HE]
- Müller B, Melson T, Heger A, et al (2017) Supernova simulations from a 3D progenitor model - Impact of perturbations and evolution of explosion properties. *Mon. Not. R. Astron. Soc.* 472:491–513. <https://doi.org/10.1093/mnras/stx1962>, arXiv:1705.00620 [astro-ph.SR]
- Müller B, Gay DW, Heger A, et al (2018) Multi-dimensional simulations of ultrastripped supernovae to shock breakout. *Mon. Not. R. Astron. Soc.* 479:3675–3689. <https://doi.org/10.1093/mnras/sty1683>, arXiv:1803.03388 [astro-ph.SR]
- Müller B, Tauris TM, Heger A, et al (2019) Three-dimensional simulations of neutrino-driven core-collapse supernovae from low-mass single and binary star progenitors. *Mon. Not. R. Astron. Soc.* 484:3307–3324. <https://doi.org/10.1093/mnras/stz216>, arXiv:1811.05483 [astro-ph.SR]
- Nadezhin DK (1980) Some Secondary Indications of Gravitational Collapse. *Astrophys. Space Sci.* 69:115–125. <https://doi.org/10.1007/>

BF00638971

- Nagakura H, Sumiyoshi K, Yamada S (2019) Possible Early Linear Acceleration of Proto-neutron Stars via Asymmetric Neutrino Emission in Core-collapse Supernovae. *Astrophys. J. Lett.* 880:L28. <https://doi.org/10.3847/2041-8213/ab30ca>, [arXiv:1907.04863](https://arxiv.org/abs/1907.04863) [astro-ph.HE]
- Nakamura K, Takiwaki T, Kuroda T, et al (2015) Systematic features of axisymmetric neutrino-driven core-collapse supernova models in multiple progenitors. *Publ. Astron. Soc. Jpn* 67:107. <https://doi.org/10.1093/pasj/psv073>, [arXiv:1406.2415](https://arxiv.org/abs/1406.2415) [astro-ph.HE]
- Nordhaus J, Brandt TD, Burrows A, et al (2010) Theoretical support for the hydrodynamic mechanism of pulsar kicks. *Phys. Rev. D* 82:103016. <https://doi.org/10.1103/PhysRevD.82.103016>, [arXiv:1010.0674](https://arxiv.org/abs/1010.0674) [astro-ph.HE]
- Nordhaus J, Brandt TD, Burrows A, et al (2012) The hydrodynamic origin of neutron star kicks. *Mon. Not. R. Astron. Soc.* 423:1805–1812. <https://doi.org/10.1111/j.1365-2966.2012.21002.x>, [arXiv:1112.3342](https://arxiv.org/abs/1112.3342) [astro-ph.SR]
- O'Connor E, Ott CD (2011a) Black Hole Formation in Failing Core-Collapse Supernovae. *Astrophys. J.* 730:70. <https://doi.org/10.1088/0004-637X/730/2/70>, [arXiv:1010.5550](https://arxiv.org/abs/1010.5550) [astro-ph.HE]
- O'Connor E, Ott CD (2011b) Black Hole Formation in Failing Core-Collapse Supernovae. *Astrophys. J.* 730:70. <https://doi.org/10.1088/0004-637X/730/2/70>, [arXiv:1010.5550](https://arxiv.org/abs/1010.5550) [astro-ph.HE]
- O'Connor EP, Couch SM (2018) Exploring Fundamentally Three-dimensional Phenomena in High-fidelity Simulations of Core-collapse Supernovae. *Astrophys. J.* 865:81. <https://doi.org/10.3847/1538-4357/aadcf7>, [arXiv:1807.07579](https://arxiv.org/abs/1807.07579) [astro-ph.HE]
- O'Doherty TN, Bahramian A, Miller-Jones JCA, et al (2023) An observationally derived kick distribution for neutron stars in binary systems. *Mon. Not. R. Astron. Soc.* 521(2):2504–2524. <https://doi.org/10.1093/mnras/stad680>, [arXiv:2303.01059](https://arxiv.org/abs/2303.01059) [astro-ph.HE]
- Oh M, Fishbach M, Kimball C, et al (2023) The Role of Natal Kicks in Forming Asymmetric Compact Binary Mergers. *Astrophys. J.* 953:152. <https://doi.org/10.3847/1538-4357/ace349>, [arXiv:2303.06081](https://arxiv.org/abs/2303.06081) [astro-ph.HE]
- Ohnishi N, Kotake K, Yamada S (2006) Numerical Analysis of Standing Accretion Shock Instability with Neutrino Heating in Supernova Cores. *Astrophys. J.* 641:1018–1028. <https://doi.org/10.1086/500554>, [arXiv:astro-ph/0509765](https://arxiv.org/abs/astro-ph/0509765) [astro-ph]
- Orlando S, Wongwathanarat A, Janka HT, et al (2021) The fully developed remnant of a neutrino-driven supernova. Evolution of ejecta structure and asymmetries in SNR Cassiopeia A. *Astron. Astrophys.* 645:A66. <https://doi.org/10.1051/0004-6361/202039335>, [arXiv:2009.01789](https://arxiv.org/abs/2009.01789) [astro-ph.HE]
- Ott CD, Roberts LF, da Silva Schneider A, et al (2018) The Progenitor Dependence of Core-collapse Supernovae from Three-dimensional Simulations with Progenitor Models of 12–40 M_{\odot} . *Astrophys. J. Lett.* 855:L3. <https://doi.org/10.3847/2041-8213/aaa967>, [arXiv:1712.01304](https://arxiv.org/abs/1712.01304) [astro-ph.HE]
- Pan KC, Liebendörfer M, Couch SM, et al (2021) Stellar Mass Black Hole Formation and Multimessenger Signals from Three-dimensional Rotating Core-collapse Supernova Simulations. *Astrophys. J.* 914:140. <https://doi.org/10.3847/1538-4357/abfb05>, [arXiv:2010.02453](https://arxiv.org/abs/2010.02453) [astro-ph.HE]
- Pejcha O, Prieto JL (2015) On the Intrinsic Diversity of Type II-Plateau Supernovae. *Astrophys. J.* 806:225. <https://doi.org/10.1088/0004-637X/806/2/225>, [arXiv:1501.06573](https://arxiv.org/abs/1501.06573) [astro-ph.SR]
- Podsiadlowski P, Langer N, Poelarends AJT, et al (2004) The Effects of Binary Evolution on the Dynamics of Core Collapse and

- Neutron Star Kicks. *Astrophys. J.* 612:1044–1051. <https://doi.org/10.1086/421713>, [arXiv:astro-ph/0309588](https://arxiv.org/abs/astro-ph/0309588) [astro-ph]
- Powell J, Müller B (2019) Gravitational wave emission from 3D explosion models of core-collapse supernovae with low and normal explosion energies. *Mon. Not. R. Astron. Soc.* 487:1178–1190. <https://doi.org/10.1093/mnras/stz1304>, [arXiv:1812.05738](https://arxiv.org/abs/1812.05738) [astro-ph.HE]
- Powell J, Müller B (2020) Three-dimensional core-collapse supernova simulations of massive and rotating progenitors. *Mon. Not. R. Astron. Soc.* 494:4665–4675. <https://doi.org/10.1093/mnras/staa1048>, [arXiv:2002.10115](https://arxiv.org/abs/2002.10115) [astro-ph.HE]
- Powell J, Müller B, Heger A (2021) The final core collapse of pulsational pair instability supernovae. *Mon. Not. R. Astron. Soc.* 503:2108–2122. <https://doi.org/10.1093/mnras/stab614>, [arXiv:2101.06889](https://arxiv.org/abs/2101.06889) [astro-ph.HE]
- Powell J, Müller B, Aguilera-Dena DR, et al (2023) Three dimensional magnetorotational core-collapse supernova explosions of a 39 solar mass progenitor star. *Mon. Not. R. Astron. Soc.* 522:6070–6086. <https://doi.org/10.1093/mnras/stad1292>, [arXiv:2212.00200](https://arxiv.org/abs/2212.00200) [astro-ph.HE]
- Radice D, Morozova V, Burrows A, et al (2019) Characterizing the Gravitational Wave Signal from Core-collapse Supernovae. *Astrophys. J. Lett.* 876:L9. <https://doi.org/10.3847/2041-8213/ab191a>, [arXiv:1812.07703](https://arxiv.org/abs/1812.07703) [astro-ph.HE]
- Rahman N, Janka HT, Stockinger G, et al (2022) Pulsational pair-instability supernovae: gravitational collapse, black hole formation, and beyond. *Mon. Not. R. Astron. Soc.* 512:4503–4540. <https://doi.org/10.1093/mnras/stac758>, [arXiv:2112.09707](https://arxiv.org/abs/2112.09707) [astro-ph.HE]
- Rampp M, Janka HT (2002) Radiation hydrodynamics with neutrinos. Variable Eddington factor method for core-collapse supernova simulations. *Astron. Astrophys.* 396:361–392. <https://doi.org/10.1051/0004-6361:20021398>, [arXiv:astro-ph/0203101](https://arxiv.org/abs/astro-ph/0203101) [astro-ph]
- Rantsiou E, Burrows A, Nordhaus J, et al (2011) Induced Rotation in Three-dimensional Simulations of Core-collapse Supernovae: Implications for Pulsar Spins. *Astrophys. J.* 732:57. <https://doi.org/10.1088/0004-637X/732/1/57>, [arXiv:1010.5238](https://arxiv.org/abs/1010.5238) [astro-ph.HE]
- Repetto S, Nelemans G (2015) Constraining the formation of black holes in short-period black hole low-mass X-ray binaries. *Mon. Not. R. Astron. Soc.* 453:3341–3355. <https://doi.org/10.1093/mnras/stv1753>, [arXiv:1507.08105](https://arxiv.org/abs/1507.08105) [astro-ph.HE]
- Repetto S, Davies MB, Sigurdsson S (2012) Investigating stellar-mass black hole kicks. *Mon. Not. R. Astron. Soc.* 425:2799–2809. <https://doi.org/10.1111/j.1365-2966.2012.21549.x>, [arXiv:1203.3077](https://arxiv.org/abs/1203.3077) [astro-ph.GA]
- Repetto S, Igoshev AP, Nelemans G (2017) The Galactic distribution of X-ray binaries and its implications for compact object formation and natal kicks. *Mon. Not. R. Astron. Soc.* 467:298–310. <https://doi.org/10.1093/mnras/stx027>, [arXiv:1701.01347](https://arxiv.org/abs/1701.01347) [astro-ph.HE]
- Scheck L, Plewa T, Janka HT, et al (2004) Pulsar Recoil by Large-Scale Anisotropies in Supernova Explosions. *Phys. Rev. Lett.* 92:011103. <https://doi.org/10.1103/PhysRevLett.92.011103>, [arXiv:astro-ph/0307352](https://arxiv.org/abs/astro-ph/0307352) [astro-ph]
- Scheck L, Kifonidis K, Janka HT, et al (2006) Multidimensional supernova simulations with approximative neutrino transport. I. Neutron star kicks and the anisotropy of neutrino-driven explosions in two spatial dimensions. *Astron. Astrophys.* 457:963–986. <https://doi.org/10.1051/0004-6361:20064855>, [arXiv:astro-ph/0601302](https://arxiv.org/abs/astro-ph/0601302) [astro-ph]
- Scheck L, Janka HT, Foglizzo T, et al (2008) Multidimensional supernova simulations with approximative neutrino transport. II. Convection and the advective-acoustic cycle in the supernova core. *Astron. Astrophys.* 477:931–952. <https://doi.org/10.1051/0004-6361:20077701>, [arXiv:0704.3001](https://arxiv.org/abs/0704.3001) [astro-ph]

- Steiner AW, Hempel M, Fischer T (2013) Core-collapse Supernova Equations of State Based on Neutron Star Observations. *Astrophys. J.* 774:17. <https://doi.org/10.1088/0004-637X/774/1/17>, arXiv:1207.2184 [astro-ph.SR]
- Stevance HF, Ghodla S, Richards S, et al (2023) VFTS 243 as predicted by the BPASS fiducial models. *Mon. Not. R. Astron. Soc.* 520:4740–4746. <https://doi.org/10.1093/mnras/stad362>, arXiv:2208.02258 [astro-ph.SR]
- Stockinger G, Janka HT, Kresse D, et al (2020) Three-dimensional models of core-collapse supernovae from low-mass progenitors with implications for Crab. *Mon. Not. R. Astron. Soc.* 496:2039–2084. <https://doi.org/10.1093/mnras/staa1691>, arXiv:2005.02420 [astro-ph.HE]
- Sukhbold T, Woosley SE (2014) The Compactness of Presupernova Stellar Cores. *Astrophys. J.* 783:10. <https://doi.org/10.1088/0004-637X/783/1/10>, arXiv:1311.6546 [astro-ph.SR]
- Sukhbold T, Ertl T, Woosley SE, et al (2016) Core-collapse Supernovae from 9 to 120 Solar Masses Based on Neutrino-powered Explosions. *Astrophys. J.* 821:38. <https://doi.org/10.3847/0004-637X/821/1/38>, arXiv:1510.04643 [astro-ph.HE]
- Sukhbold T, Woosley SE, Heger A (2018) A High-resolution Study of Presupernova Core Structure. *Astrophys. J.* 860:93. <https://doi.org/10.3847/1538-4357/aac2da>, arXiv:1710.03243 [astro-ph.HE]
- Summa A, Janka HT, Melson T, et al (2018) Rotation-supported Neutrino-driven Supernova Explosions in Three Dimensions and the Critical Luminosity Condition. *Astrophys. J.* 852:28. <https://doi.org/10.3847/1538-4357/aa9ce8>, arXiv:1708.04154 [astro-ph.HE]
- Tamborra I, Hanke F, Janka HT, et al (2014) Self-sustained Asymmetry of Lepton-number Emission: A New Phenomenon during the Supernova Shock-accretion Phase in Three Dimensions. *Astrophys. J.* 792:96. <https://doi.org/10.1088/0004-637X/792/2/96>, arXiv:1402.5418 [astro-ph.SR]
- Tauris TM, Kramer M, Freire PCC, et al (2017) Formation of Double Neutron Star Systems. *Astrophys. J.* 846:170. <https://doi.org/10.3847/1538-4357/aa7e89>, arXiv:1706.09438 [astro-ph.HE]
- Vartanyan D, Burrows A (2023) Neutrino signatures of 100 2D Axisymmetric Core-Collapse Supernova Simulations. *Mon. Not. R. Astron. Soc.* 526:5900–5910. <https://doi.org/10.1093/mnras/stad2887>, arXiv:2307.08735 [astro-ph.HE]
- Vartanyan D, Burrows A, Radice D (2019) Temporal and angular variations of 3D core-collapse supernova emissions and their physical correlations. *Mon. Not. R. Astron. Soc.* 489:2227–2246. <https://doi.org/10.1093/mnras/stz2307>, arXiv:1906.08787 [astro-ph.HE]
- Vartanyan D, Burrows A, Wang T, et al (2023) Gravitational-wave signature of core-collapse supernovae. *Phys. Rev. D* 107:103015. <https://doi.org/10.1103/PhysRevD.107.103015>, arXiv:2302.07092 [astro-ph.HE]
- Vigna-Gómez A, Willcox R, Tamborra I, et al (2023) Observational evidence for neutrino natal kicks from black-hole binary VFTS 243. arXiv e-prints <https://doi.org/10.48550/arXiv.2310.01509>, arXiv:2310.01509 [astro-ph.HE]
- Walk L, Tamborra I, Janka HT, et al (2019) Effects of the standing accretion-shock instability and the lepton-emission self-sustained asymmetry in the neutrino emission of rotating supernovae. *Phys. Rev. D* 100:063018. <https://doi.org/10.1103/PhysRevD.100.063018>, arXiv:1901.06235 [astro-ph.HE]
- Walk L, Tamborra I, Janka HT, et al (2020) Neutrino emission characteristics of black hole formation in three-dimensional simulations of stellar collapse. *Phys. Rev. D* 101:123013. <https://doi.org/10.1103/PhysRevD.101.123013>, arXiv:1910.12971 [astro-ph.HE]
- Wongwathanarat A, Janka HT, Müller E (2010) Hydrodynamical Neutron Star Kicks in Three Dimensions. *Astrophys. J. Lett.* 725:L106–L110. <https://doi.org/10.1088/2041-8205/725/1/L106>, arXiv:1010.0167 [astro-ph.HE]

- Wongwathanarat A, Janka HT, Müller E (2013) Three-dimensional neutrino-driven supernovae: Neutron star kicks, spins, and asymmetric ejection of nucleosynthesis products. *Astron. Astrophys.* 552:A126. <https://doi.org/10.1051/0004-6361/201220636>, [arXiv:1210.8148](https://arxiv.org/abs/1210.8148) [astro-ph.HE]
- Wongwathanarat A, Janka HT, Müller E, et al (2017) Production and Distribution of ^{44}Ti and ^{56}Ni in a Three-dimensional Supernova Model Resembling Cassiopeia A. *Astrophys. J.* 842:13. <https://doi.org/10.3847/1538-4357/aa72de>, [arXiv:1610.05643](https://arxiv.org/abs/1610.05643) [astro-ph.HE]
- Woosley SE, Heger A (2007) Nucleosynthesis and remnants in massive stars of solar metallicity. *Phys. Rep.* 442:269–283. <https://doi.org/10.1016/j.physrep.2007.02.009>, [arXiv:astro-ph/0702176](https://arxiv.org/abs/astro-ph/0702176) [astro-ph]
- Woosley SE, Heger A (2015) The Remarkable Deaths of 9-11 Solar Mass Stars. *Astrophys. J.* 810:34. <https://doi.org/10.1088/0004-637X/810/1/34>, [arXiv:1505.06712](https://arxiv.org/abs/1505.06712) [astro-ph.SR]
- Woosley SE, Heger A, Weaver TA (2002) The evolution and explosion of massive stars. *Reviews of Modern Physics* 74:1015–1071. <https://doi.org/10.1103/RevModPhys.74.1015>
- Wu Y, Pan Z, Qian L, et al (2023) Three Pulsars Discovered in Globular Cluster M15 (NGC 7078) with FAST. *arXiv e-prints* <https://doi.org/10.48550/arXiv.2312.06067>, [arXiv:2312.06067](https://arxiv.org/abs/2312.06067) [astro-ph.HE]
- Yadav N, Müller B, Janka HT, et al (2020) Large-scale Mixing in a Violent Oxygen-Neon Shell Merger Prior to a Core-collapse Supernova. *Astrophys. J.* 890:94. <https://doi.org/10.3847/1538-4357/ab66bb>, [arXiv:1905.04378](https://arxiv.org/abs/1905.04378) [astro-ph.HE]